ABSTRACT

Title of Document: TEMPLATE SYNTHESIZED NANOTUBES, NANOWIRES AND HETEROGENEOUS COAXIAL NANOWIRES FOR ELECTROCHEMICAL ENERGY STORAGE

Ran Liu, Doctor of Philosophy, 2009

Directed By: Professor, Sang Bok Lee
Department of Chemistry and Biochemistry

Template synthesized nanomaterials have been successfully applied in electrochemical energy storage systems such as supercapacitors and lithium ion batteries. The first part of present study will list examples of applying various nanomaterials such as nanowires, nanotubes and heterostructured nanowires in different electrochemical energy storage systems for enhancing their charge/discharge rates, energy densities and power densities, etc. The following of the thesis will describe the template synthesis of nanomaterials in details. The experimental part of this thesis will concentrate on the fabrication of alumina template and the detailed experimental setups for aluminum anodization and template synthesis of nanomaterials. The rest of the thesis analyzes four cases of using template synthesized nanomaterials in electrochemical energy storage, which include my major work during my PhD studies. The first one is utilizing poly(3,4-ethylenedioxythiophene) (PEDOT) nanotubes as electrode materials for high-powered supercapacitor. The thin-walled nanotubes allow fast charge/discharge of the

PEDOT to achieve high power. The second one is related to synthesis and characterization of RuO_2/PEDOT composite nanotubes for supercapacitors. Loading appropriate amount of RuO_2 can effectively enhance the specific capacitance of PEDOT nanotube. The third case illustrates the synthesis of MnO_2/PEDOT coaxial nanowires by one step coelectrodeposition for electrochemical energy storage. The combined properties of MnO_2 and PEDOT enable the coaxial nanowires to have very high specific capacitances at high current densities. Their formation mechanism will be explored and their nanostructures are tuned for optimized electrochemical properties. The final case reports the MnO_2-Nanoparticles enriched PEDOT nanowires for enhanced electrochemical energy storage capacity. Large amount of the MnO_2 nanoparticles can be loaded into PEDOT nanowires after they are soaked in $KMnO_4$ solution. Thus loaded MnO_2 nanoparticles effective enhance the energy densities of PEDOT nanowires without causing too much volume expansion to them.

TEMPLATE SYNTHESIZED NANOTUBES, NANOWIRES AND HETEROGENEOUS COAXIAL NANOWIRES FOR ELECTROCHEMICAL ENERGY STORAGE

By

Ran Liu

Dissertation submitted to the Faculty of the Graduate School of the
University of Maryland, College Park, in partial fulfillment
of the requirements for the degree of
Doctor of Philosophy
2009

Advisory Committee:
Professor Sang Bok Lee, Chair
Professor Alice Mignerey
Professor Janice Reutt-Robey
Professor Yu Huang Wang
Professor Kyu Yong Choi

Dedication

This work is dedicated in great love to my parents, my wife and my mentors.

Acknowledgements

I owe my gratitude to all the people who have made this thesis possible.

First and foremost, I am deeply indebted to my advisor, Sang Bok Lee, who has been my mentor throughout my graduate studies. He guided me into this interesting field, encouraged me to start my research and provided strong support at each stage of the thesis. His invaluable advice has shaped my work and thoughts and will continue to influence my future research. I am grateful for his continuous guidance and his confidence in me even in the most difficult moments.

In addition, thanks are due to Professor Alice Mignerey, Professor Janice Reutt-Robey, Professor Yu Huang Wang and Professor Kyu Yong Choi for kindly accepting to serve on my committee and for their suggestions and support along the way.

I owe my deepest thanks to my wife, Ran Bi, for her unwavering support and love along the journey of life. Her companionship made this difficult process an enjoyable and inspiring one. My gratitude also goes to my parents for their forever love, understanding and untold sacrifice.

Table of Contents

List of Tables

List of Figures

List of Illustrations

Chapter 1: Applications of Nanomaterials in Electrochemical Energy Storage

1.1 Introduction

Climate change and the decreasing availability of fossil fuels require society to move towards sustainable and renewable resources. As a result, we are observing an increase in renewable energy production from sun and wind, as well as the development of electric vehicles or hybrid electric vehicles with low CO_2 emissions. Because the sun does not shine during the night, wind does not blow on demand and we all expect to drive our car with at least a few hours of autonomy, energy storage systems are starting to play a larger part in our lives. At the forefront of these are electrical energy storage systems, such as batteries[1-6] and electrochemical capacitors (ECs).[1-8] However, we need to improve their performance substantially to meet the higher requirement (high power density and high energy density) of future systems such as a plug-in hybrid electric vehicles (PHEV's)[1], revolutionary advances such as innovative materials with architecture tailored structures are needed for constructing these electrochemical energy storage systems.

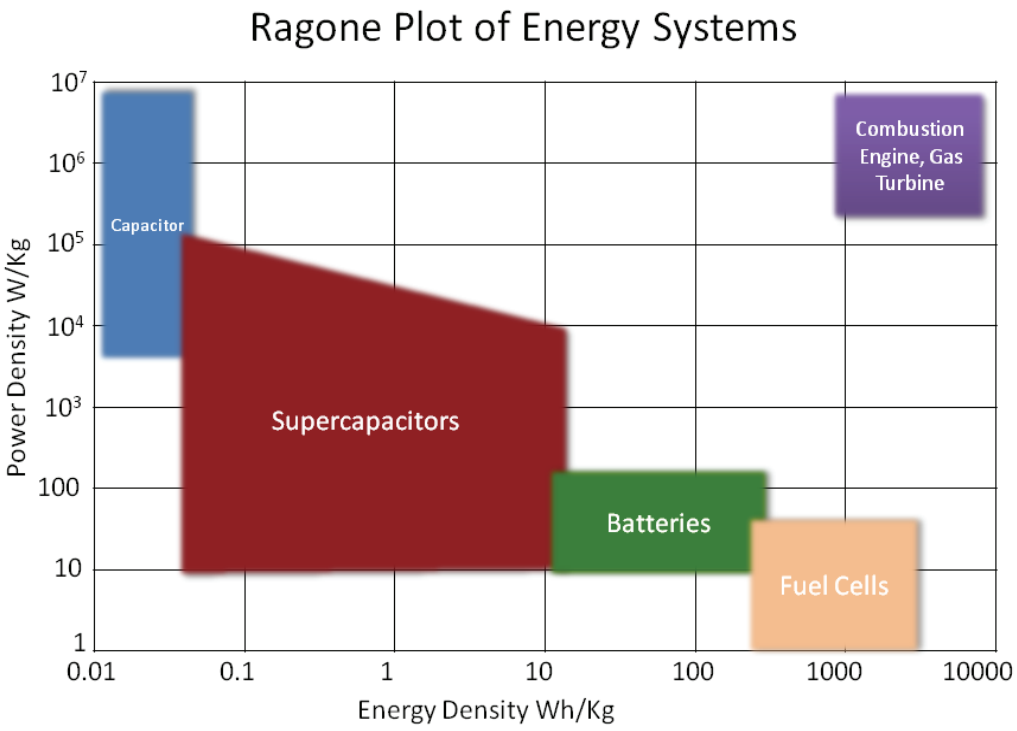

Figure 1.1 Ragone plot of the electrochemical energy storage system

Figure 1.1 shows the plot of power against energy density, also called a Ragone plot, [2] for the most important energy storage systems. Apparently, we would like an electrochemical energy storage that can have both high power and high energy densities, which is located the right-above corner on Figure 1.1 to meet the future requirement. However, a lot of efforts are needed for the scientists to more toward this goal.

Nanostructured materials have attracted great interest in recent years because of the unusual mechanical, electrical and optical properties endowed by confining the dimensions of such materials and because of the combination of bulk and surface properties to the overall behavior[3-11]. One need only consider the staggering developments in microelectronics to appreciate the potential of materials with reduced dimensions. Nanostructured materials are becoming increasingly important

for electrochemical energy storage.[3-6] Here we address this topic in this chapter. It is important to appreciate the advantages and disadvantages of nanomaterials for energy conversion and storage, as well as how to control their synthesis and properties. This is a sizeable challenge facing those involved in materials research into energy conversion and storage. It is beyond the scope of this chapter to give an exhaustive summary of the energy storage and conversion devices that may now or in the future benefit from the use of nanomaterials; rather, the contents of this chapter will be limited to the fields of supercapacitors and lithium ion batteries.

1.2 Electrochemical Capacitors or Supercapacitors

Although great efforts have gone into developing high-performance Li-ion and other advanced secondary batteries that use nanomaterials or organic redox couples[3-5], Electrochemical Capacitors (ECs) have attracted less attention until very recently. Because Li-ion batteries suffer from a somewhat slow power delivery or uptake, faster and higher-power energy storage systems are needed in a number of applications, and this role has been given to the ECs[6]. Also known as supercapacitors or ultracapacitors, ECs are power devices that can be fully charged or discharged in seconds; as a consequence, their energy density (about 5 Wh kg^{-1}) is lower than in batteries, but a much higher power delivery or uptake (10 kW kg^{-1}) can be achieved for shorter times (a few seconds)[7]. They have had an important role in complementing or replacing batteries in the energy storage field, such as for uninterruptible power supplies (back-up supplies used to protect against power disruption) and load-leveling. A more recent example is the use of electrochemical double layer capacitors (EDLCs) in emergency doors (16 per plane) on an Airbus A380, thus proving that in

terms of performance, safety and reliability ECs are definitely ready for large-scale implementation. A recent report by the US Department of Energy assigns equal importance to supercapacitors and batteries for future energy storage systems and articles on supercapacitors appearing in business and popular magazines show increasing interest by the general public.

Several types of ECs can be distinguished, depending on the charge storage mechanism as well as the active materials used. EDLCs, the most common devices at present, use carbon-based active materials with high surface area.[8-13] A second group of ECs, known as pseudo-capacitors or redox supercapacitors, uses fast and reversible surface or near-surface reactions for charge storage. Transition metal oxides[14-16] as well as electrically conducting polymers[17-20] are examples of pseudo-capacitive active materials. Hybrid capacitors, combining a capacitive or pseudo-capacitive electrode with a battery electrode, are the latest kind of EC, which benefit from both the capacitor and the battery properties.

Electrochemical capacitors currently fill the gap between batteries and conventional solid state and electrolytic capacitors, as we can see from the Ragone plot in Fig 1.1. They store hundreds or thousands of times more charge (tens to hundreds of farads per gram) than the latter, because of a much larger surface area (1,000–2,000 $m^2 g^{-1}$) available for charge storage in EDLC. However, they have a lower energy density than batteries, and this limits the optimal discharge time to less than a minute, whereas many applications clearly need more.[21] Since the early days of EC development in the late 1950s, there has not been a good strategy for increasing the

energy density; only incremental performance improvements were achieved from the 1960s to 1990s. The impressive increase in performance that has been demonstrated in the past couple of years is due to the discovery of new electrode materials and improved understanding of ion behavior in small pores, as well as the design of new hybrid systems combining faradic and capacitive electrodes. Here we give an overview of past and recent findings as well as an analysis of what the future holds for ECs.

1.2.1 Electrochemical Double-Layer Capacitors

The first patent describing the concept of an electrochemical capacitor was filed in 1957 by Becker[21], who used carbon with a high specific surface area (SSA) coated on a metallic current collector in a sulfuric acid solution. In 1971, NEC (Japan) developed aqueous-electrolyte capacitors under the energy company SOHIO's license for power-saving units in electronics, and this application can be considered as the starting point for electrochemical capacitor use in commercial devices[21]. New applications in mobile electronics, transportation (cars, trucks, trams, trains and buses), renewable energy production and aerospace systems bolstered further research.

EDLCs are electrochemical capacitors that store the charge electrostatically using reversible adsorption of ions of the electrolyte onto active materials that are electrochemically stable and have high accessible SSA. Charge separation occurs on polarization at the electrode–electrolyte interface (Figure 1.2), producing what Helmholtz described in 1853 as the double layer capacitance *C*:

$$C = \frac{\varepsilon_r \varepsilon_0 A}{d} \tag{1.1}$$

where ε_r is the electrolyte dielectric constant, ε_0 is the dielectric constant of the vacuum, d is the effective thickness of the double layer (charge separation distance) and A is the electrode surface area.[22]

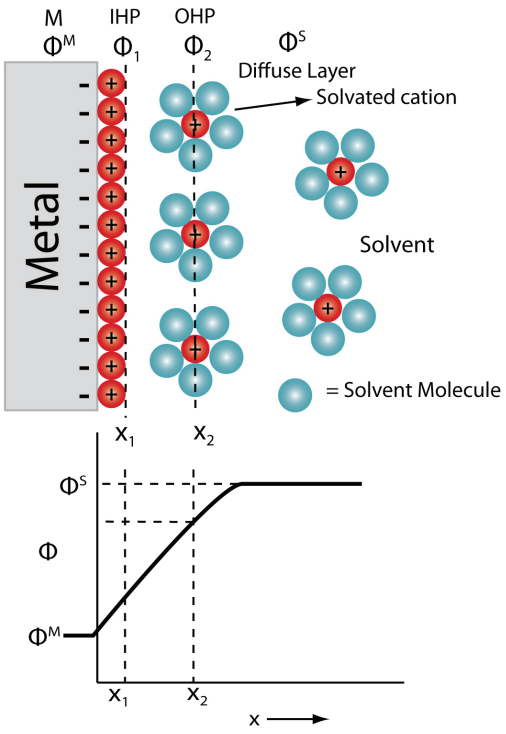

Figure 1.2 Charge separation occurs on polarization at the electrode–electrolyte interface for the double layer charge, which induces the double layer supercapacitance

This capacitance model was later refined by Gouy and Chapman, and Stern and Geary, who suggested the presence of a diffuse layer in the electrolyte due to the accumulation of ions close to the electrode surface. The double layer capacitance is

between 5 and 20 μF cm^{-2} depending on the electrolyte used.[8] Specific capacitance achieved with aqueous alkaline or acid solutions is generally higher than in organic electrolytes, but organic electrolytes are more widely used as they can sustain a higher operation voltage (up to 2.7 V in symmetric systems). Because the energy stored is proportional to voltage squared according to

$$E = \frac{1}{2} C V^2 \tag{1.2}$$

a three-fold increase in voltage, V, results in about an order of magnitude increase in energy, E, stored at the same capacitance.

As a result of the electrostatic charge storage, there is no faradic (redox) reaction at EDLC electrodes. A supercapacitor electrode must be considered as a blocking electrode from an electrochemical point of view. This major difference from batteries means that there is no limitation by the electrochemical kinetics through a polarization resistance. In addition, this surface storage mechanism allows very fast energy uptake and delivery, and better power performance. The absence of faradic reactions also eliminates the swelling in the active material that batteries show during charge/discharge cycles. EDLCs can sustain millions of cycles whereas batteries survive a few thousand at best. Finally, the solvent of the electrolyte is not involved in the charge storage mechanism, unlike in Li-ion batteries where it contributes to the solid–electrolyte interphase when graphite anodes or high-potential cathodes are used. This does not limit the choice of solvents, and electrolytes with high power performances at low temperatures (down to -40 °C) can be designed for EDLCs.

However, as a consequence of the electrostatic surface charging mechanism, these devices suffer from a limited energy density. This explains why today's EDLC research is largely focused on increasing their energy performance and widening the temperature limits into the range where batteries cannot operate[21].

1.2.2 Redox-based Electrochemical Capacitors

Some ECs use fast, reversible redox reactions at the surface of active materials, thus defining what is called the pseudo-capacitive behavior. As shown in the Figure 1.3, the electrons are transferred from the electrode materials to the current collector or vice visa, depending on the charge/discharge process, which induced the redox reaction of the electrode materials. At the same time, the charged ions such protons, metal ions, or hydroxide, other cations are diffused in and out during in the redox reaction at the surface of electrode material. Metal oxides such as RuO_2[23,24], Fe_3O_4[25,26] or MnO_2[27-29], as well as electronically conducting polymers[17,18,20,30], have been extensively studied in the past decades. The specific pseudo-capacitance exceeds that of carbon materials using double layer charge storage, justifying interest in these systems. But because redox reactions are used, pseudo-capacitors, like batteries, often suffer from a lack of stability during cycling.

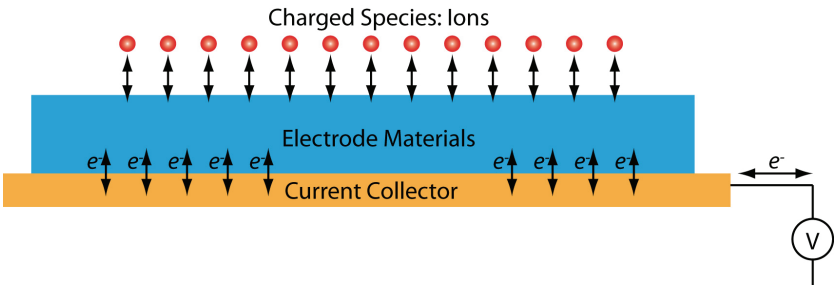

Figure 1.3 Mechanism of pseudo-capacitive charge storage

Ruthenium oxide, RuO_2, is widely studied because it is conductive and has three distinct oxidation states accessible within 1.2 V. The pseudo-capacitive behavior of RuO_2 in acidic solutions has been the focus of research in the past 30 years. It can be described as a fast, reversible electron transfer together with an electro-adsorption of protons on the surface of RuO_2 particles, where Ru oxidation states can change from (II) up to (IV):

$$RuO_2+xH^++xe^-\leftrightarrow RuO_{2-x}(OH)_x$$

where $0 \leq x \leq 2$. The continuous change of x during proton insertion or de-insertion occurs over a window of about 1.2 V and leads to a capacitive behavior with ion adsorption following a Frumkin-type isotherm. Specific capacitance of more than 600 F g^{-1} has been reported, but Ru-based aqueous electrochemical capacitors are expensive, and the 1-V voltage window limits their applications to small electronic devices. Organic electrolytes with proton surrogates (for example Li^+) must be used to go past 1 V. Less expensive oxides of iron, vanadium, nickel and cobalt have been tested in aqueous electrolytes, but none has been investigated as much as manganese oxide. The charge storage mechanism is based on surface adsorption of electrolyte cations C^+ (K^+, Na^+...) as well as proton incorporation according to the reaction:

$$MnO_2 + xC^+ + yH^+ + (x+y)e^- \leftrightarrow MnOOC_xH_y$$

MnO_2 micro-powders or micrometer-thick films show a specific capacitance of about 150 F g^{-1} in neutral aqueous electrolytes within a voltage window of <1 V.

Accordingly, there is limited interest in MnO_2 electrodes for symmetric devices, because there are no oxidation states available at less than 0 V. Other transition metal oxides with various oxidation degrees, such as molybdenum oxides, should also be explored as active materials for pseudo-capacitors.

Many kinds of conducting polymers (polyaniline[31,32], polypyrrole[30,33], polythiophene and their derivatives[34,35]) have been tested in EC applications as pseudo-capacitive materials and have shown high gravimetric and volumetric pseudo-capacitance in various non-aqueous electrolytes at operating voltages of about 3 V. When used as bulk materials, conducting polymers suffer from a limited stability during cycling that reduces the initial performance. Research efforts with conducting polymers for supercapacitor applications are nowadays directed towards hybrid systems.

1.2.3 Nanostructuring redox-active materials to increase capacitance and power

Given that nanomaterials have helped to improve Li-ion batteries, it is not surprising that nanostructuring has also affected ECs. Because pseudo-capacitors store charge in the first few nanometers from the surface, decreasing the particle size increases active material usage and the charge/discharge rate, which leads to the increase of energy density (specific capacitance) as well as the power densities. Thanks to a thin electrically conducting surface layer of oxide and oxynitride, the charging mechanism of nanocrystalline vanadium nitride (VN) includes a combination of an electric double layer and a faradic reaction (II/IV) at the surface of the nanoparticles[36], leading to specific capacitance up to 1,200 F g^{-1} at a scan rate of 2 mV s^{-1}. A similar approach can be applied to other nano-sized transition metal

nitrides or oxides. In another example, the cycling stability and the specific capacitance of RuO_2 nanoparticles were increased by depositing a thin conducting polymer coating that enhanced proton exchange at the surface[37]. The design of specific surface functionalization to improve interfacial exchange could be suggested as a generic approach to other pseudo-redox materials.

MnO_2 and RuO_2 films have been synthesized at the nanometer scale. Thin MnO_2 deposits of tens to hundreds of nanometers have been produced on various substrates such as metal collectors, carbon nanotubes or activated carbons. Specific capacitances as high as 1,300 F g^{-1} have been reported, as reaction kinetics were no longer limited by the electrical conductivity of MnO_2.[38] In the same way, Sugimoto's group have prepared hydrated RuO_2 nano-sheets with capacitance exceeding 1,300 F g^{-1}. The RuO_2 specific capacitance also increased sharply when the film thickness was decreased[39]. The deposition of RuO_2 thin film onto carbon supports both increased the capacitance and decreased the RuO_2 consumption[40]. Thin film synthesis or high SSA capacitive material decoration with nano-sized pseudo-capacitive active material, like the examples presented in, offers an opportunity to increase energy density and compete with carbon-based EDLCs. Particular attention must be paid to further processing of nano-sized powders into active films because they tend to re-agglomerate into large-size grains. An alternative way to produce porous films from powders is by growing nanotubes, as has been shown for V_2O_5, or nanorods[41]. These allow easy access to the active material, but can only be produced in thin films so far, and the manufacturing cost will probably limit the use of these sophisticated nanostructures to small electronic devices.

Nanostructured materials have also been applied to enhance the power density (enhance the charge/discharge rate) of the electroactive materials for supercapacitor. For example, using arrays of one-dimensional hollow nanotubular structures has recently emerged as a solution achieving high power because of their intrinsic structural characteristics[42,43]. The thin nature of the nanotube wall enables the rapid redox processes of electroactive materials such as conductive polymers and metal oxides by providing large surface area to the counter-ions. Furthermore, long nanotubes can provide high surface area and enough mass loading for electrode materials to store sufficient energy. Nanotubes of RuO_2 and poly (3,4-ethylenedioxythiophene) (PEDOT) have been reported for high power supercapacitors by Hu's group[42] and our group[43] respectively. Details for the PEDOT nanotube based supercapacitor are described later in Chapter 4.

1.3 Lithium-ion Batteries

Rechargeable lithium batteries have revolutionized portable electronic devices. They have become the dominant power source for cell phones, digital cameras, laptops etc., because of their superior energy density (capability to store 2– 3 times the energy per unit weight and volume compared with conventional rechargeable batteries). The worldwide market for rechargeable lithium batteries is now valued at 10 billion dollars per annum and growing. They are the technology of choice for future hybrid electric vehicles, which are central to the reduction of CO_2 emissions arising from transportation.

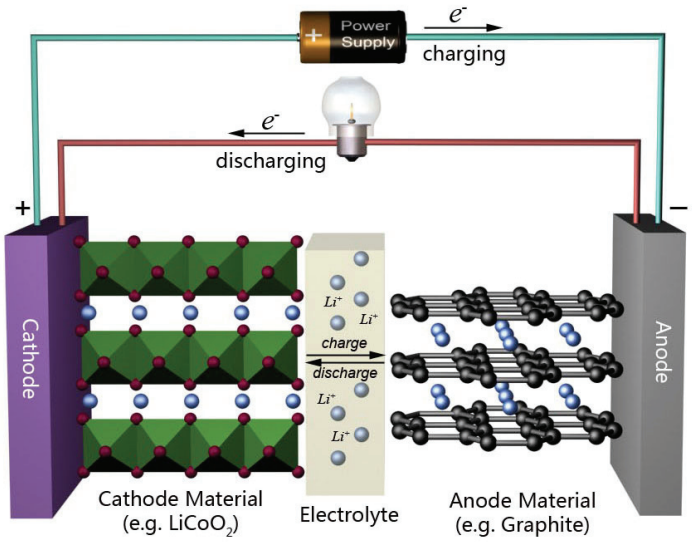

Figure 1.4 Charge storage mechanism of lithium-ion batteries

The rechargeable lithium battery does not contain lithium metal. It is a lithium-ion device, comprising a graphite negative electrode (anode), a non-aqueous liquid electrolyte, and a positive electrode (cathode) formed from layered $LiCoO_2$ (Figure 1.4). On charging, lithium ions are deintercalated from the layered $LiCoO_2$ intercalation host, pass across the electrolyte, and are intercalated between the graphite layers in the anode. Discharge reverses this process. The electrons, of course, pass around the external circuit. The rechargeable lithium battery is a supreme representation of solid-state chemistry in action. A more detailed account of lithium-ion batteries than is appropriate here may be obtained from the literature. The first-generation lithium-ion battery has electrodes that are composed of powders containing millimeter-sized particles, and the electrolyte is trapped within the millimeter-sized pores of a polypropylene separator. Although the battery has a high energy density, it is a low-power device (slow charge/discharge). No matter how creative we are in designing new lithium intercalation hosts with higher rates, limits

exist because of the intrinsic diffusivity of the lithium ion in the solid state (ca. 10^{-8} cm^2 s^{-1}), which inevitably limits the rate of intercalation/deintercalation, and hence charge/ discharge. However, an increase in the charge/discharge rate of lithium-ion batteries of more than one order of magnitude is required to meet the future demands of hybrid electric vehicles and clean energy storage. Nanomaterials, so often hyped or misrepresented by claims of delivering new properties, have the genuine potential to make a significant impact on the performance of lithium-ion batteries, as their reduced dimensions enable far higher intercalation/deintercalation rates and hence high power[44-47]. This is just one property that may be enhanced by the use of nanomaterials. However, nanomaterials are certainly not a panacea. The advantages and disadvantages of lithium-ion battery materials are summarized in Section 1.3.1 and 1.3.2 and thereafter advances (Section 1.3.3) in the use of nanomaterials, emphasizing in particular nanostructured materials, as negative electrodes, electrolytes, and positive electrodes for rechargeable lithium batteries are described.

1.3.1 Benefits of Nanometer Size Effects

Nanomaterials can play a large role in improving the performance of lithium-ion batteries, because in nanoscaled systems the distances over which Li^+ must diffuse are dramatically decreased; the nanomaterials can quickly absorb and store vast numbers of lithium ions without causing any deterioration in the electrode; and nanomaterials have large surface areas, short diffusion lengths, and fast diffusion rates along their many grain boundaries. Much enhanced capacities, high rate performance, capacity retention abilities, and many novel Li storage systems have been found to benefit from nanometer size effects.

(1) Enhanced Lithium Storage Kinetics

The achievement of high power density is hindered by kinetic problems in the electrode materials, i.e., the slow Li^+ and e^- diffusion. For solid-state diffusion of Li in electrode materials, the mean diffusion (or storage) time, t_{eq}, is determined by the diffusion coefficient, D, and the diffusion length, L, according to the following formula: $t_{eq} = L^2/D$ Two approaches are, at present, gaining momentum in resolving the kinetic problems of electrode materials. One approach is increasing D by doping the electrode materials with foreign atoms. Although mixed conduction is thus improved, only limited rate-performance enhancement can be achieved, and sometimes the introduction of heteroatoms can result in unstable crystal structure.

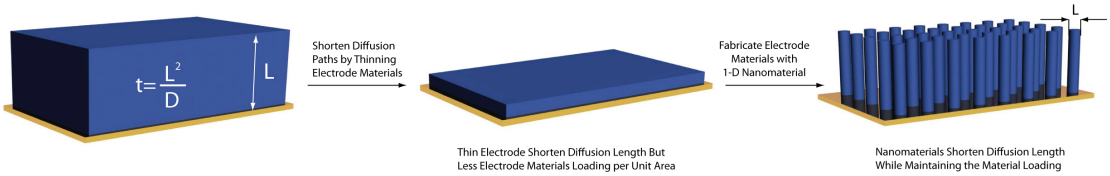

Figure 1.5 Using array of one dimensional nanomaterials to shorten the diffusion length for lithium intercalation in lithium-ion battery

An alternative approach is decreasing L, which has been realized by nanostructuring of electrode materials[48]. For example, a reduction of L from 10 μm (the typical size of commercial electrode materials) to 100 nm reduces, for a material with $D=10^{-10}$ cm^2 s^{-1} (the typical value of electrode materials), the t_{eq} from 5000 to 0.5 s. The effects are so remarkable that the most extensive research work over the years has followed this direction. However, an electrode material with such small thickness is not usable in reality. The development of one dimensional nanomaterials such as nanowires can solve this problem not only because radically small dimensions of

nanowires the can effectively shorten the diffusion lengths of the ions which can improve the charge/discharge rate capabilities but also because their axially big dimensions can provide high surface area and enough mass loading for electrode materials to store sufficient energy[49-51]. Other types of nanomaterials (e.g. nanoparticles, nanotubes, coaxial nanowires and core/shell nanoparticles)[44,46] for the application of lithium-ion batteries can be found in the Figure 1.6.

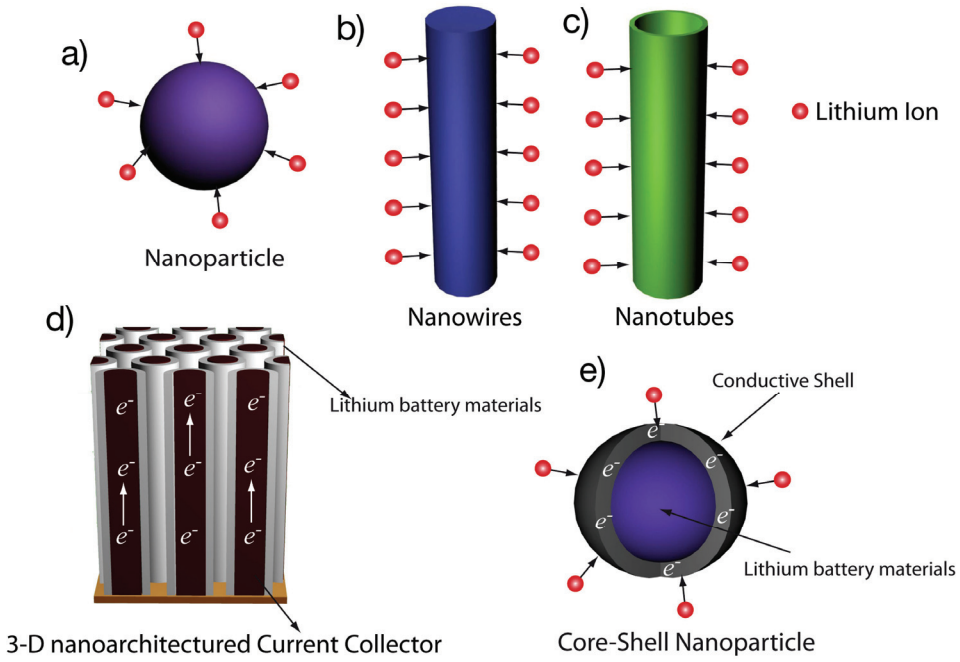

Figure 1.6 Summary of nanostructured cathode and anode materials used for different types of lithium-ion batteries.

(2) Enhanced Structural Stability

Small particles would more easily accommodate the structural changes occurring during the cycling process where Li is inserted and extracted. For example, layered $LiMnO_2$ suffers from structural instability during cycling and as a result, exhibits significant capacity fade. In nanomaterials the charge accommodation occurs largely

at or very near the surface and the smaller the particles are, the larger the portion of these constituent atoms at the surface[52]. This fact reduces the need for diffusion of Li^+ in the solid phase, greatly increasing the charge and discharge rate of the cathode as well as reducing the volumetric changes and lattice stresses caused by repeated Li insertion and expulsion (Figure 1.7).

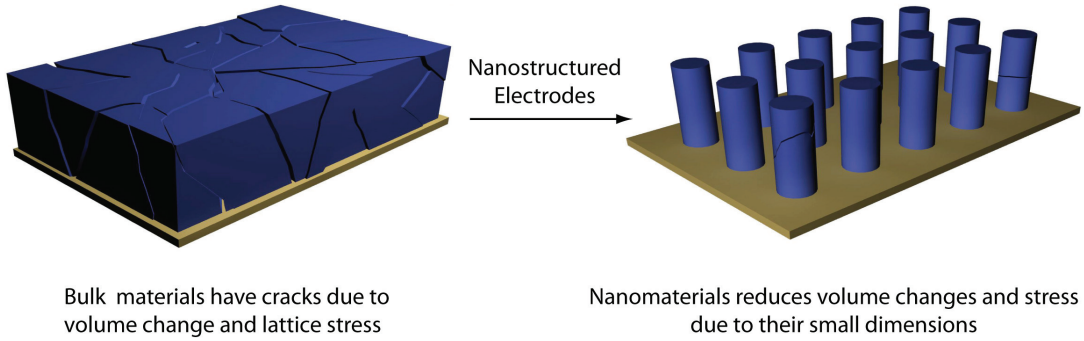

Figure 1.7 Nanomaterials reduces materials stress during charge/discharge

(3) New Lithium-Storage Mechanisms

Another benefit of nanostructured electrode materials is that they can lead to new Li-storage mechanisms, affording high capacities, rechargeability, and general applicability to a range of battery systems. One such new mechanism is referred to as a 'conversion' mechanism, first found in transition metal oxides[53], followed by fluorides, sulfides, and nitrides[49,54,55]. The mechanisms are mainly related to reversible in situ formation and decomposition of Li_yX (where X=O, S, F, or N) upon Li uptake and release, which can be described by the following equation:

$$MX + yLi^+ + ye^- \leftrightarrow Li_yX + M$$

where M=Fe, Co, Ni, Cr, Mn, Cu, and so on. Usually, reversible capacities in these systems, which have been demonstrated as innovative high energy anode materials for lithium-ion batteries, are in the range of 400–1100mAh g^{-1}. It is reported that

electrodes made of CoO nanoparticles can deliver a specific capacity of 700mAh g^{-1} with 100% capacity retention for up to 100 charge/discharge cycles and high recharging current rates[53].

1.3.2 Disadvantages of Nanomaterials in the applications of Lithium-ion batteries

(1) Low Thermodynamic Stability

One should note that as nanometer-sized particles have very high specific surface area and high surface energy, and tend to form agglomerates, they are therefore difficult to disperse and mix them with carbon black and binder to produce electrodes. Thus, the contact resistance of an electrode using nanometer-sized particles is much higher than that of commercial one, which explains the failing of performance (e.g., capacity fading) frequently happens in some cases. Another drawback of nanometer-sized electrode materials is the pronounced electrochemical agglomeration during electrochemical cycling. For example, nano-SnSb undergoes successive agglomeration during Li insertion and extraction, which consequently leads to quick capacity fading[56].

(2) High Surface Reactions

The high surface area of nanoparticles also raises the risk of secondary reactions involving electrolyte decomposition between electrode and electrolyte, which causes a high level of irreversibility (low columbic efficiency) and poor cycle life. For nanostructured electrode materials, the stabilized electrochemical windows become narrow compared with bulk materials. In nanometer-sized anodes, thick solid electrolyte interphase (SEI) films commonly form, which consume lots of the Li ions

supplied by cathodes. Furthermore, it has been found in many nanometer-sized transition metal oxides, the thick SEI films formed during Li uptake may disappear completely catalyzed by transition metal upon Li extraction, which may lead to capacity fade and safety problem. Residual species such as organic surfactants may also exist on the surface of nanomaterials. The high level impurities means pronounced secondary reactions that may also lead to serious safety problem. So far, most of the nano-systems studied exhibit a low columbic efficiency ca. 60–80% during the first cycle, the remaining 20– 40% capacity loss is mainly due to the thick SEI film formation and other Li-consuming surface secondary reactions. It should be noted that nanomaterials usually exhibit a poor packing density of electrodes, which limits the volumetric energy density because there is a larger proportion of 'inert' components such as binder or carbon black.

1.3.3 Examples of using nanomaterials in the applications of lithium-ion batteries

(1) Negative Electrodes

Nanoparticles

Graphite powder, composed of micrometer-sized particles, has been the stalwart of negative electrodes for rechargeable lithium batteries for many years. Replacement by nanoparticulate graphite would increase the rate of lithium insertion/removal and thus the rate (power) of the battery. However the formation of a passivating (SEI:solid electrolyte interface) layer on the graphite surface. In addition, lithium deposition on the graphite surface cause formidable problems[57,58].

Owing to their ability to store large amounts of lithium, lithium metal alloys, Li_xM_y, are of great interest as high capacity anode materials in lithium-ion cells[59-63]. Such alloys have specific capacities which exceed that of the conventional graphite anode; for example, $Li_{4.4}Sn$ (993 mAh g^{-1} and 1000 mA hr versus 372 mAh g^{-1} and 855 mAh cm^{-3} for graphite), and $Li_{4.4}Si$ (4200 $mAhg^{-1}$ and 1750 $mAhcm^{-3}$). Unfortunately, the consequence of accommodating such a large amount of lithium is large volume expansion–contraction that accompanies their electrochemical alloy formation. These changes lead rapidly to deterioration of the electrode (cracks, and eventually, pulverization), thus limiting its lifetime to only a few charge–discharge cycles. Significant research effort has been devoted to overcome this problem. One of the earliest approaches involved replacing bulk material with nanostructured alloys.

Nanotubes/wires

Given the significance of C_{60} and carbon nanotubes, it is apposite to start with a comment on their potential use as negative electrodes in lithium batteries. Several investigations have been carried out on these materials as electrodes. Although lithium intercalation is possible, and carbon nanotubes exhibit twice the lithium storage compared with graphite, similar problems of surface-layer formation and safety are present. Nanotubes/nanowires composed of TiO_2-(B), the fifth polymorph of titanium dioxide, retain the advantages of $Li_4Ti_5O_{12}$: low cost, low toxicity, high safety, and an electrode potential that eliminates lithium plating[64-66]. Furthermore, the amount of lithium that may be stored increases from 150 $mAhg^{-1}$ to 300 $mAhg^{-1}$, and this increased storage can be delivered at similar high rates to $Li_4Ti_5O_{12}$.

Cui and his coworker reported high-performance lithium battery anodes using silicon nanowires[51]. In their report, they show that silicon nanowire battery electrodes circumvent these issues as they can accommodate large strain without pulverization, provide good electronic contact and conduction, and display short lithium insertion distances. The theoretical charge capacity for silicon anodes was achieved and maintained a discharge capacity close to 75% of this maximum, with little fading during cycling.

A recent significant progress made in this field was reported by Belcher and coworkers[67]. Viruses were introduced as the template to synthesize and assemble Co_3O_4 and hybrid Au-Co_3O_4 nanowires under ambient and aqueous conditions. The virus-prepared crystalline Co_3O_4 nanowires exhibited higher reversible capacity than powders without viruses. The superior electrochemical properties of the viral templated wires were ascribed to their large surface areas, structural integrity, and dense packing, as well as favorable crystallinity.

(2) Positive Electrodes

Nanoparticles

Most of the lithium intercalation compounds suitable for use as positive electrodes in rechargeable lithium batteries have been prepared in the form of nanoparticles by methods such as grinding, synthesis from solution, or by sol–gel approaches. The rate of lithium intercalation/deintercalation is increased for compounds such as $LiCoO_2$, $LiMn_2O_4$, Li-$(Ni_{1/2}Mn_{1/2})O_2$, $Li(Mn_{1/3}Co_{1/3}Ni_{1/3})O_2$, and $Li[Ni_{1/2}Mn_{3/2}]O_4$, because of

the shorter diffusion lengths and higher electrolyte/ electrode contact area compared with micrometer particles[68-70].

Nanoparticulate $LiFePO_4$ deserves special attention[58,71-73]. It is an attractive cathode because of its low cost, high thermal and chemical stability, and lower voltage (3.4 V versus Li^+/Li) compared to other positive electrodes, making it less reactive towards electrolytes, resulting in higher electrochemical stability. The intercalation mechanism involves a two-phase reaction between $FePO_4$ and $LiFePO_4$. On extraction of lithium from a particle of $LiFePO_4$, a shell of $FePO_4$ forms just below the surface of the particle, and as lithium continues to be extracted the phase boundary between this shell and the $LiFePO_4$ core moves through the particle.

Nanotubes/wires

As described for anodes, it is possible to fabricate nanostructured positive electrodes of various dimensions, most notably nanowires or nanotubes. For example, nanotubes of V_2O_5 and nanowires of other lithium intercalation hosts, including $LiCoO_2$ and $Li(Ni_{1/2}Mn_{1/2})O_2$, have been prepared[74,75], and shown to act as intercalation hosts for lithium. In many cases, the performance, especially in terms of rate capability, is enhanced compared with bulk materials.

Martin and his coworkers later reported on the synthesis of V_2O_5 and $LiFeO_4$ nanofibers using polycarbonate (PC) membranes template and the study of their rate performance for Li intercalation[76,77]. Cao and collaborators prepared and investigated different template-prepared V_2O_5 nanostructures including nanorods and nanotubes arrays as well as Ni-$V_2O_5 \cdot nH_2O$ core–shell nanocable arrays[45].

1.4 Heterostructured Nanomaterials for the applications of electrochemical energy storage

In the previous sections, we have demonstrated the advantages of nanomaterials in the applications of electrochemical energy storage such as lithium ion batteries and supercapacitors. However, nanomaterials with single material may not be able to fulfill the requirements of future electrochemical energy storage due to its limitations[78], such as low energy densities, slow kinetics (low power densities), poor conductivities and weak mechanical stabilities. Electron transport properties (or electron conductivity) and mechanical strength can be serious limiting factors in the development of electrode materials that will give high power density or will maintain the material's intrinsic energy density at high power demand[51,71,79,80]. For example, various compositions of manganese and cobalt oxides are popular cathode materials for supercapacitors and Li^+ ion batteries and generally have high energy density, but their serious drawbacks are poor electrical conductivity and weak mechanical strength, especially when they are nanostructured. Without high electron conductivity, the nanostructured material itself cannot provide high power density. Many reports on nanostructured materials (both the cathodes and anodes, including a recent report on Si nanowires as anode material) have shown limited performance in charge-discharge rate (power density) and number of cycles because of the intrinsically poor and/or degrading conductivity and mechanical stability during the charge-discharge cycles affecting cyclability[51]. Thus, in order to meet the challenges for nano-based energy storage, heterogeneous nanostructured materials, which have multi-nanocomponents, each tailored to address different demands (e.g. high energy density, high conductivity and excellent mechanical stability), are necessitated. The

resulting materials will exhibit synergic properties of each component, which can realize the full potentials of the materials with excellent performance (e.g. high energy density and high power density). However, the success of applying heterogeneous nanostructured materials in the energy storage will hinge on a few factors (1) how to choose a proper combination of different materials (2) how to design and optimize the heterogeneous nanostructure, for example, coaxial nanowires[81] (Figure 1.8a), segmented nanowires, core-shell nanoparticles[76,82,83] (Figure 1.8b), (3) how to synthesize or assemble the nanocomponents into the desired and proposed nanostructures.

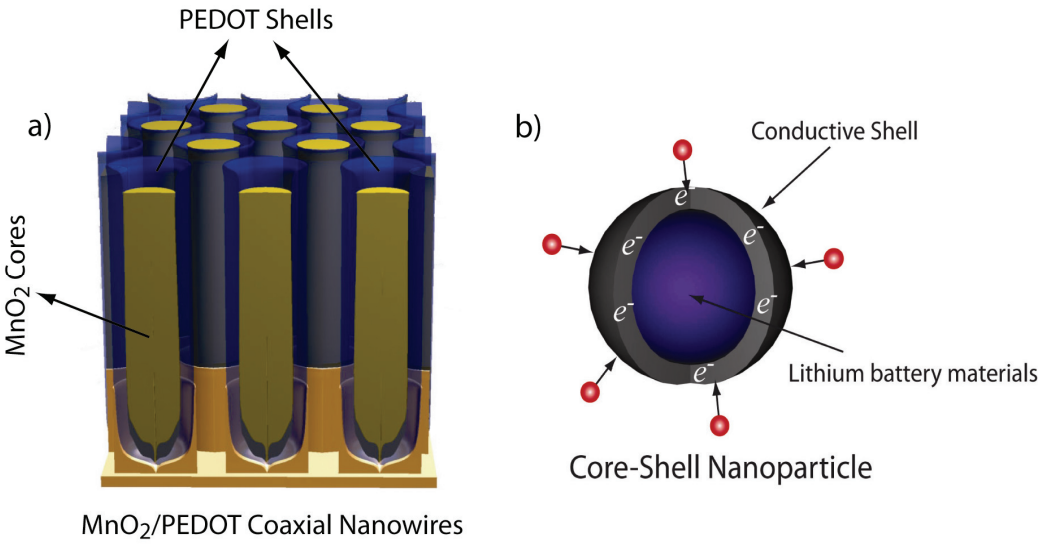

Figure 1.8 Heterostructured nanomaterials for the application of electrochemical energy storage

The second factor is especially important because the material properties can be dramatically enhanced if the appropriate nanostructure is chosen. The next question rises on how to accommodate different materials into a heterogeneous nanostructure and how to optimize the structure and composition of each nanocomponent to fully

bring its potentials into play. Core-shell nanoparticles composed with $LiFePO_4$/Carbon have been reported for enhanced conductivities as well as fast charge/discharge rate[76,83]. Coaxial nanowires or nanotubes have also attracted an increasing amount of attention due to their advantages of added synergetic properties of functionalities as well as the benefits from the one dimensional nanostructures mentioned earlier. For example, SnO_2-In_2O_3 heterostructured nanowires[84] and coaxial MnO_2/Carbon nanotube array electrodes have been reported for high performance lithium ion batteries[81].

In Chapter 5-8, we will investigate a few examples of using heterostructured nanomaterials (e.g. composite RuO_2/PEDOT nanowires, coaxial MnO_2/PEDOT nanowires, hybrid MnO_2 nanoparticles with PEDOT nanowires) for the applications of electrochemical energy storage.

1.5 Template Synthesized Nanomaterials for the Application of Electrochemical Energy Storage

In the previous sections, we have briefly reviewed the advantages of using various nanomaterials in the applications of electrochemical energy storage. And apparently it is very important to develop a mature and systematic synthetic method to fabricate such nanomaterials. Indeed, there are numerous approaches to fabricate nanomaterials, such as sol-gel[85,86], chemical vapor deposition[87,88], hydrothermal and[89,90] template synthesis[91-95]. Among these methods, the template synthesis technique is versatile to construct advanced nanomaterials with controlled structures and desired functions, especially the 1-D nanomaterials such as nanowires, nanotube and coaxial nanowires, etc. Template directed materials generally possess structural

and morphological abundance due to the diversity of employed template precursors[91-95]. Nano/microscaled electrode materials with different morphologies such as one-dimensional (1D) wire/tube structures, 2D films, and 3D interconnected porous architectures can be obtained through the template synthesis method. The template-synthesized materials normally exhibit small crystalline size, high surface area, large surface-to volume ratio, and favorable structural stability. These characteristics are beneficial to the electrochemical properties because they would lead to fast ion/electron transfer, sufficient contact between active materials and electrolyte, and enhanced flexibility. Improved electrode performances such as higher overall capacity, better high-rate capability, and longer cycling life can be expected accordingly. Therefore, introducing template technique in preparing and assembling electrode materials may offer new opportunities to further increase the performance of the existing electrochemical energy storage system[96].

Pioneering work carried out by Martin and co-workers has shown that template synthesis is a useful method to generate nanomaterials for diverse potential applications[76,77,97-108]. For example, they reported the template preparation of carbon nanotubule membranes for electrochemical energy storage. They prepared free-standing nanoporous carbon membranes and carbon nanotubules by chemical vapor deposition method combined with AAO template[97]. According to their cyclic voltammograms (CV) results, the template-synthesized tubule membranes delivered a high Li^+ intercalation capacity of 490 mA h g^{-1}, whereas the capacity of the tube-in-tube carbon membrane was at least two times higher. Later they reported the synthesis of V_2O_5 and $LiFeO_4$ nanofibers[76,102] using polycarbonate (PC) membranes

template and the study of their rate performance for Li intercalation. An early short review on the membrane template-prepared materials for Li-ion batteries was presented by the same group in 2002[104]. Ever since martin's innovative work, much more progress has been made in both the template synthesis and the applications of templated materials for lithium storage. For instance, Cao and collaborators prepared and investigated different template-prepared V_2O_5 nanostructures including nanorods and nanotubes arrays as well as Ni-$V_2O_5 \cdot nH_2O$ core–shell nanocable arrays[41,45].

Recently, AAO template synthesis has also been applied to fabricate heterostructured nanomaterials for the electrochemical energy storage. As an example, it has been successfully applied to fabricate MnO_2/PEDOT coaxial nanowires for the applications of supercapacitors[109], which will be described in details in Chapter 6. In addition, template synthesis has been applied to synthesize 3-D nanoarchitectured electrode, which can be coated with electroactive materials for the lithium-ion batteries to achieve fast charge/discharge rate. Here are two cases:

Simon and his collaborators reported a Fe_3O_4-based Cu nanoarchitectured electrode for Li-ion batteries[110]. The electrode was prepared by using a two-step design: the electrochemically assisted template growth of Cu nanorods followed by electrodeposition of Fe_3O_4. The obtained nanostructured electrodes were demonstrated to show a factor of 6 improvement in power density over planar electrodes. High capacity as well as excellent rate capability and cycling performance were also observed, making these conversion electrodes attractive to traditional intercalation electrodes for Li-ion batteries. In addition, large hysteresis between charge and discharge profiles was presented in the conversion reactions, which was

suggested to derive from the high activation barrier triggering the oxidation and reduction reactions. This charge/discharge potential difference, however, would result in poor energy efficiency and thus remains to be overcome as one of the major hurdles in the applicability of Fe_3O_4 nanoarchitectures.

Similar work has been reported by Hassoun et al[111], a nanoarchitectured Cu current collector prepared by template synthesis was used as the current collector, of which the surface was completely coated with Ni_3Sn_4 particles tests in lithium cells show that the nanostructured Ni_3Sn_4 electrodes cycle with a capacity of the order of 500 mAh g^{-1} with no decay over 200 cycles. In addition, these electrodes may operate at rates as high as 10 C while still delivering 20% of their theoretical capacity.

The advantages of the template synthesis lie in: (1) a variety of materials ranging from inorganic/organic compounds to polymers and even biological materials can be employed as templates without limitation to membranes. (2) various electrode materials with diverse compositions, structures, and morphologies can be obtained through the template synthesis route. In the next chapter, we will focus on the template synthesis, which is such a versatile and powerful tool to synthesize nanomaterials.

Chapter 2: Template Synthesis of Nanomaterials

2.1 Introduction

The most common method for the fabrication of structures in the sub-micrometer size regime is the "top-down" technology ('from large to small'), where using lithographic technique nanoscaled elements are cut from large entities. However, as one approaches sizes below 100 nm the resolution and replication speed limit the efficiency, consequently in this size regime the "bottom-up" technology ('from small to large') becomes important. One of the most popular "bottom-up" methods to fabricate nanomaterials is named as "template synthesis", which will be discussed in details in the following sections.

2.1.1 Template Synthesis of Nanomaterials

One of the easiest ways to control the shape and size of a material is to synthesize it inside a mold or template. This process is ubiquitous in the manufacturing world. Car tires, concrete walls, and gelatin desserts are all examples of products produced by casting the precursor material into a mold or form. This remains true down to nanoscopic dimensions. Here the template simply serves as a scaffold against which other kinds of materials with similar morphologies are synthesized. In other words, the in situ generated material is shaped into a nanostructure with its morphology complementary to that of the template. The overall process of template synthesis generally involves the following procedures: (1) precursors combine with templates by impregnation or incorporation; (2) solid species form through reaction, nucleation and growth; and (3) selectively remove the template in order to harvest resultant nanostructures.

Based on different types of templates, the template synthesis can be mainly categorized into two classes: hard template synthesis and soft template (or pseudo-template) synthesis. Other than these two major categories, there are some other important types of "template synthesis" methods to fabricate nanomaterials, such as template based on features on solid substrate, template based on existing nanostructures, or the combinations of different types of templates.

2.1.2 Hard Template

Hard template possess well-confined void, which is in the form of channels, pores, or connected hollow spaces. Various types of hard template are illustrated in Figure 2.1. The connectivity of the pores or channels strongly influences the structure of the resulting solid product. In the case of nonconnected porous templates such as AAO (anodic aluminum oxide) membranes[92] and mesoporous silica[112-114] (e.g. MCM-41 and SBA-15), solid product forms inside the isolated pores, replicating the shape of the void space in templates. As a result, aligned structures such as 1D nanotubes and nanowires are usually obtained after removing the template scaffold. However, the nanowires or nanotubes arrays fabricated from mesoporous silica are inter-connected by small pillars formed in the micro- or mesopores in the silica pore walls. Some authors also called this method "nanocasting"[115-117] in order to differentiate it from the template synthesis based on AAO membranes. The templates that consist of a continuous pore system such as photonic crystals (e.g. nature opal or self-assembled colloidal crystals)[118-120] generally lead to an inverse replica of the mold structure after template isolation, thus resulting in frameworks with interconnected 3D pores. The most widely used hard templates are AAO membranes because of their facile

preparation and controllable pore size (Figure 2.2 right). Template synthesis method based on AAO membrane has particularly fascinated scientists due to its simplicity and diverse applicabilities.

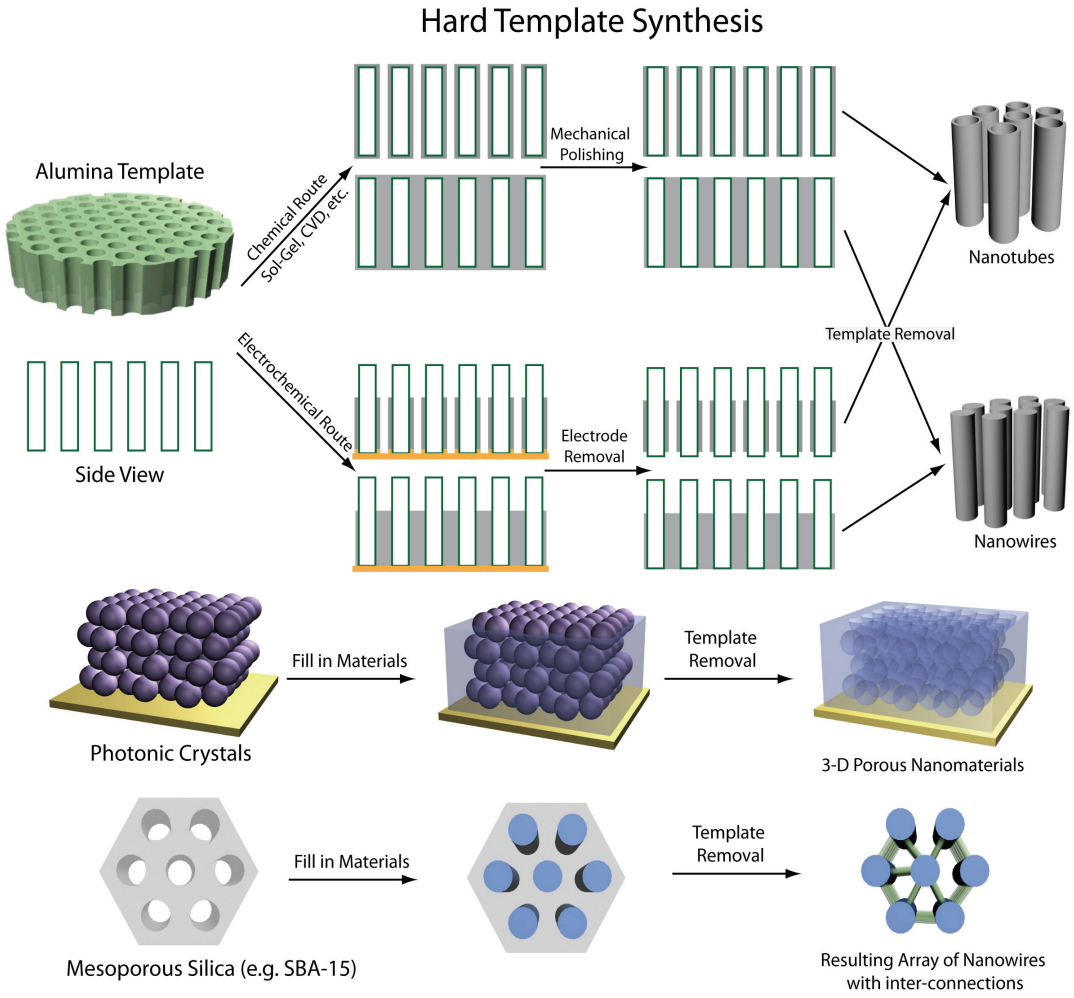

Figure 2.1 Hard template synthesis of nanomaterials

The Martin group pioneered and extensively studied this method since it was first reported by Possin et al[92,121-125]. Different methods such as electrochemical deposition[126,127], sol-gel[124], and chemical vapor depositions[98] can be combined with the template synthesis technique to fabricate different types of materials (e.g. metals[128], carbons[97], semiconductors[126], metal oxides[129], conductive polymers[125], etc.)

with different morphologies (e.g. nanotubes, nanowires, nanorings[130,131], nanodots[132] and heterogeneous nanostructures[81,109,129], etc.) Furthermore, dimensions of the deposited nanostructures can be easily controlled by regulating the template pores and deposition conditions. When the term of "template synthesis" is mentioned in the research papers, it is mostly often referred to hard template synthesis using AAO membrane, which will also be the main synthetic method discussed in this thesis. Other hard template synthesis methods such as templating against features on solid substrate (a good example is the electrodeposition of metal nanowires on step-edge of graphite sheet by Penner's group[133-135] in Figure 2.3) or templating against existing nanostructures[136,137] are also popular ones to generate nanomaterials and will not be discussed in this thesis in details.

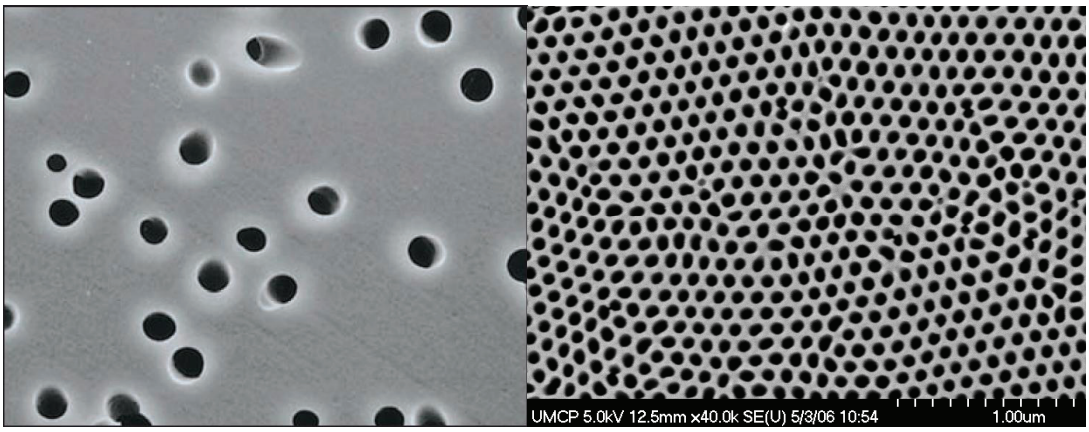

Figure 2.2 (left) SEM image of polycarbonate membrane and (right) SEM image of alumina template
(left image from http://www.advantecmfs.com/filtration/membranes/mb_pc.shtml)

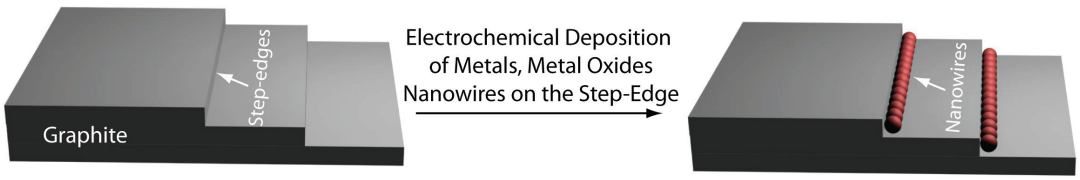

Figure 2.3 Step-edge deposition of nanowires on graphite

2.1.3 Soft Template

Soft template (or pseudo-template) usually consists of organic surfactants[138-140], polymers[141,142], and even biological viruses[67], which are relatively flexible in shape. Soft templates are facile for controlled fabrication of nanomaterials because of either the unique anisotropic structures or the functionality of their subunit groups.

In 1992, researchers at the Mobil Corporation reported the first synthesis of mesoporous silica and aluminosilicates[93]. Their synthetic approach was based on the self-assembly of a cationic surfactant into micelles that acted as a template for the "nanocasting" of the porous oxide network. Since then, interest in materials possessing ordered porous networks with uniform pore diameters in the nanometer range has intensified significantly. This new class of materials is expected to afford superior mass transport properties and enhanced surface areas in comparison with conventional porous materials, making them attractive for application in catalysis, selective separation, and electrochemical devices such as batteries and fuel cells.

Nano scientist extended this concept to fabricate dispersible nanomaterials. Here, the soft template, similar to hard template, functions as structure-directing agents that assist in the assembly of reacting species. The most common soft template is made of surfactants, which are amphiphilic species that are composed of hydrophilic heads and lipophilic tails. Surfactant are usually classified into ionic type [e.g. Sodium dodecyl sulfate (SDS), cetyl trimethylammonium bromide (CTAB)] and nonionic such as block copolymer, primary amines and poly(ethylene oxide) surfactants. All these types of surfactant have been used as soft templates[143-145].

It is well known that, when the surfactant concentration reaches a critical value, surfactant molecules spontaneously assemble into the form of aggregating entities such as micelles (sphere-shaped or rod-shaped) or liquid crystal phase, which restrict and direct the growth of a guest structures. Precursor species react in the confined space of surfactant micelles or on the surface of polymer/virus chains, as driven by self-assembly or interaction between functional groups. After separating the template, sphere-like (Figure 2.4a) or wire-like (Figure 2.4b) structures can be fabricated[146], following the basic shape of the aggregates.

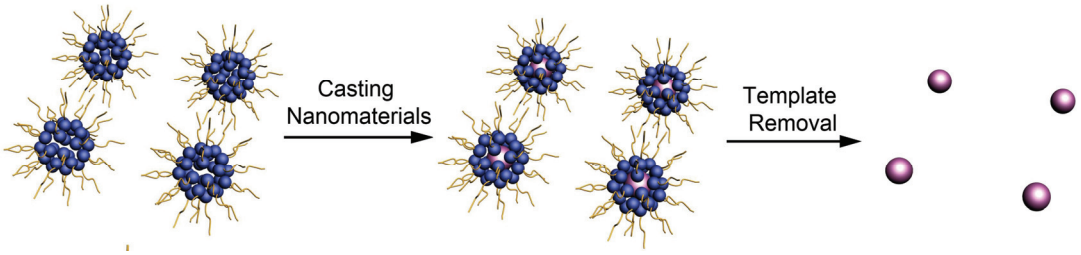

Figure 2.4a Surfactant (micelle) directed growth of nanoparticles

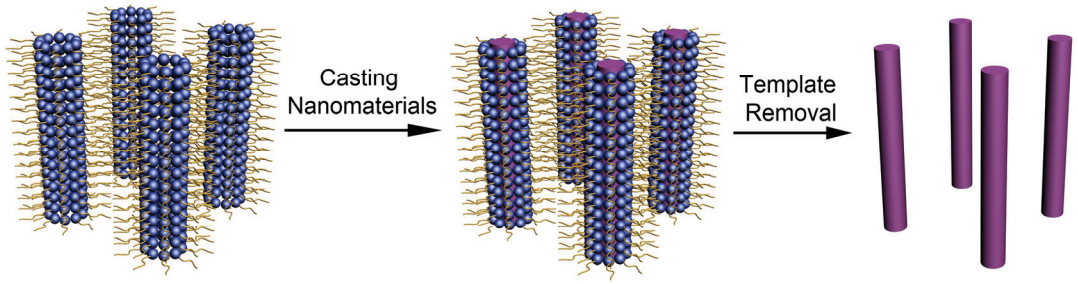

Figure 2.4b Surfactant directed growth of nanowires

Besides the surfactant, another type of soft template based on biomolecules (nanomaterials by biotemplating) has recently emerged and grows with surging speed (Figure 2.5)[147]. Biotemplating seeks to either replicate the morphological characteristics and the functionality of a biological species or use a biological structure to guide the assembly of inorganic materials. Typical biotemplates includes

peptides, proteins, DNA, lipid and virus, etc. The replication process typically leads to the generation of either a negative, positive (or hollow), or exact copy of the template. Nanoparticles, with 1-D, 2-D and 3-D assembly can be fabricated by biotemplated method owing to the sophisticated architectures (1D, 2D, and 3D) of the biotemplates and their degree of complexity achievable. For example, virus has enabled the synthesis and assembly Co_3O_4 nanowires for lithium ion battery materials[67]. Peptides have been used to cast the silver nanowires[148]. Assembly of one-dimensional metallic, semiconducting, and magnetic nanoparticle arrays with the assistance of DNA helix have all been successfully reported with good control over the dimensions, crystallinity, and even chirality[149].

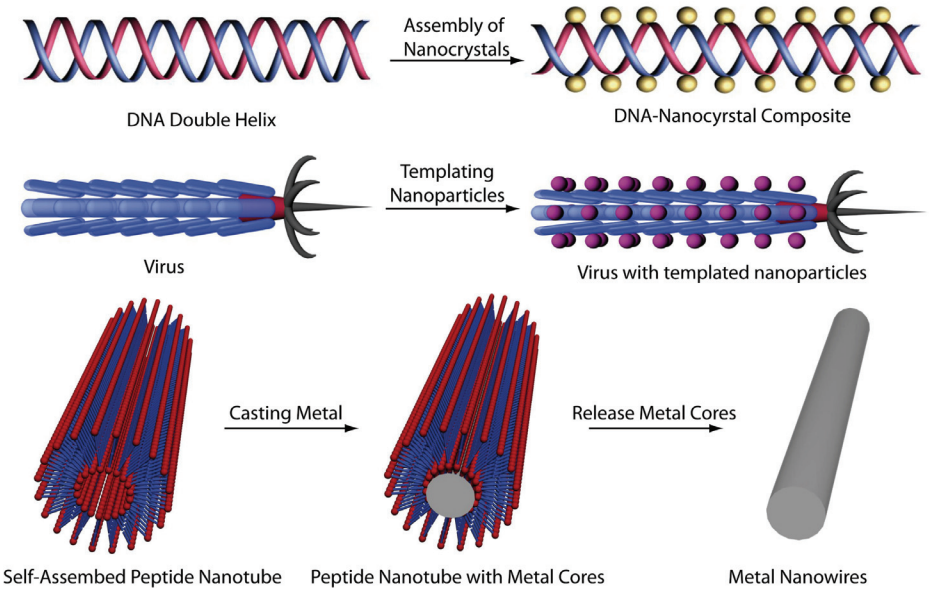

Figure 2.5 Biomolecules templated nanomaterials

2.2 Template synthesis based on different techniques

2.2.1 Electrochemical Deposition

Fundamentals

Electrochemical deposition, also known as electrodeposition, involves the oriented diffusion of charged reactive species through a solution when an external electric field is applied, and the reduction of the charged growth species at the growth or deposition surface (which also serves as an electrode). In industry, electrochemical deposition is widely used when coating metals in a process known as electroplating. In general, this method is only applicable to electrically conductive materials such as metals, alloys, semiconductors, and electrically conductive polymers. After the initial deposition, the electrode is separated from the depositing solution by the deposit and so the deposit must conduct in order to allow the deposition process to continue. When the deposition is confined to the pores of template membranes, nanocomposites are produced. If the template membrane is removed, nanorod or nanowire arrays are prepared.

When a solid is immersed in a polar solvent or an electrolyte solution, surface charge will develop. The electrode potential is described by the Nernst equation.

$$E = E_0 + \frac{RT}{n_i F} \ln(a_i)$$

where E_0 is the standard electrode potential (or the potential difference between the electrode and the solution) when the activity a_i of the ions is unity, F is Faraday's constant, R is the gas constant, and T is the temperature. When the electrode potential is higher than the energy level of a vacant molecular orbital in the electrolyte, electrons will transfer from the electrode to the solution and the electrolyte will be reduced. On the other hand, if the electrode potential is lower than the energy level of an occupied molecular orbital in the electrolyte, the electrons will transfer from the

electrolyte to the electrode, resulting in electrolyte oxidation. These reactions stop when equilibrium is achieved.

When an external electric field is applied between two dissimilar electrodes, charged species flow from one electrode to the other, and electrochemical reactions occur at both electrodes. This process, called electrolysis, converts electrical energy to chemical potential. The system used to perform electrolysis is called an electrolytic cell. In this cell, the electrode connected to the positive side of the power supply, termed the "anode", is where an oxidation reaction takes place, whereas the electrode connected to the negative side of the power supply, the "cathode", is where a reduction reaction proceeds. When is electrochemical deposition occurred on the cathode by reduction reaction, it is cathodic deposition, and vice versa.

Electrochemical deposition of nanomaterials offers several advantages which distinguish from other synthetic methods in template synthesis.

(1) Electrochemical synthesis takes place close to the electrode within the electric double layer, which has a very high potential gradient of 10^5 Vcm^{-1}. Under these conditions, the reactions often lead to products which cannot be obtained in a chemical synthesis.

(2) Electrochemical synthesis is a low-temperature technique limited by the boiling point of the electrolyte. This can be raised by using molten salt electrolytes.

(3) Kinetic control can be exercised by controlling the current passed through the cell, while thermodynamic control can be exercised by choosing the applied cell potential.

(4) An electrochemical synthesis is an oxidation or a reduction reaction. By fine-tuning the applied cell potential, the oxidizing or reducing power can be continuously varied and suitably selected-luxury not afforded by chemical synthesis.

(5) The composition and morphology of nanomaterials can be controlled by varying the bath composition and electrochemical conditions. For example, by coelectrochemical deposition method, our group has successfully synthesized MnO_2/PEDOT coaxial nanowires by one-step[109]. By tuning the potentials, we can control the morphology of the conductive polymer nanostructures such as nanowires or nanotubes.

(6) The experiments are simple to perform and the instruments are inexpensive and readily available.

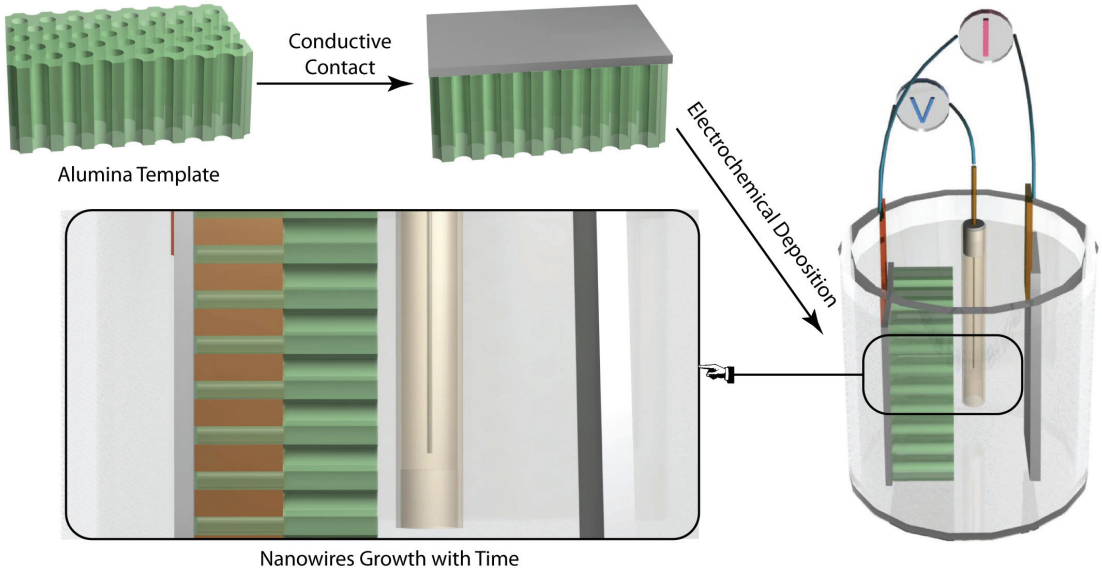

Figure 2.6 Electrochemical deposition of nanowires by AAO template

Figure 2.6 shows a typical electrochemical deposition process in the alumina template. First, one face of the template is required to be coated with a metal film

(usually via plasma sputtering), which serves as the bottom electrode in the electrochemical cell. Thus metal sputtered membrane was then assembled into a three electrode electrochemical cell. It has to be noticed that the metal sputtered face of membrane has to be protected well to avoid unwanted materials deposition. During the electrochemical deposition process, the volume of the pore is continuously filled up beginning from the pore bottom. Thus, the length of a nanostructure can be controlled by varying the amount of material deposited, which is one the advantages of electrochemical deposition. Two common electrochemical methods are used in the electrochemical deposition, one is called potentiostatic method (also called chronoamperometry and chronocoulometry), which is by applying a constant potential (thermodynamic control) while observing the current change or charge. The other one is named as galvanostatic method, which is by applying constant current (kinetic control) while monitoring the potential change.

Metals

Electrochemical deposition of metals is the most straightforward case. When the ions diffuse to the bottom of the pores, it sees the electrons that are supplied from the applied current and gets reduced to its metallic form. This is shown by the following reaction where "M" represents some metal of "n" valency.

$$M^{n+} + ne^- \rightarrow M$$

Based on *Farady's Law*: total charge (can be calculated by integrating current over time) used in the electrochemical deposition, the number of mole of deposited material can be calculated as

$$m = \frac{1}{nF}\int Idt$$

Metal Oxides

Metal oxide can also be electrodeposited into the alumina template. Electrochemical deposition of metal oxide can be mainly classified into two types based on the mechanism of electrochemical reaction[150]. The first one is based on the **electrogeneration of base**. The OH^- group can be possibly generated via the following reactions:

(1) Reactions which consume H^+ ions such as

$$2H^+ + 2e^- \rightarrow H_2 \quad E^0 = 0.0\ V$$

(2) Electrolysis of water

$$2H_2O + 2e^- \rightarrow H_2 + 2OH^- \quad E^\circ = -0.828\ V$$

(3) Anion (for example, nitrate) reduction reactions

$$NO_3^- + H_2O + 2e^- \rightarrow NO_2^- + 2OH^- \quad E^\circ = 0.01\ V$$

All these reduction reactions cause an increase in the pH of the electrolyte, close to the electrode either by the consumption of H^+ ions or by the generation of OH^- ions. Thus electrogenerated OH^- ions can effectively reaction with the metal ion to form metal hydroxide deposition. These metal hydroxides can undergo further reaction to form hydrous metal oxide, or metal oxide when the electrode is subsequently dried or fired at high temperature.

$$M^{n+} + n(OH)^- \rightarrow M(OH)_n \downarrow$$

$$M(OH)_n \longrightarrow MO_{\frac{n}{2}} \bullet \frac{n}{2} H_2O \rightarrow MO_{\frac{n}{2}} + \frac{n}{2} H_2O$$

The second one is based on **Anodic Oxidation.** In this technique, a metal ion in a lower oxidation state is oxidized to a higher oxidation state anodically. The pH of the

electrolyte is chosen in such a way that the lower oxidation state is stable while the higher oxidation state readily undergoes hydrolysis to yield the metal oxide or hydroxide.

$$M^{z+} \rightarrow M^{(z+\Delta)+} + \Delta e^-$$

$$M^{(z+\Delta)+} + (z+\Delta)OH^- \rightarrow M(OH)_{z+\Delta} \rightarrow MO_{(z+\Delta)/2} + (z+\Delta)/2H_2O$$

Semiconductors

Binaries (Groups II-VI, III-V) semiconductor such as CdSe, CdTe, Bi_2Te_3 can be electrodeposited in the alumina template in the forms of nanostructures[126,151]. Such materials are especially important in the applications of solar cells and thermoelectric devices. The electrochemical reaction usually involves the reduction of the oxyanion of group VI, V elements into their corresponding anions, thus electrogenerated anion with react with the group II, III metal cations or the metals to form semiconductor material deposited on the electrode surface. One example is the electrochemical deposition of CdSe.

$$H_2SeO_3 + 6H^+ + 4e^- \rightarrow H_2Se + 3H_2O$$

$$Cd^{2+} + H_2Se \rightarrow CdSe + 2H^+$$

The concentration of the Cd^{2+} is made to be much higher than the selenium salt due to their large difference of the reduction potential. The potential for the electrochemical deposition has also to be carefully chosen to avoid bulk metal deposition.

Conductive Polymers

Conductive polymer is another important class of material can be electrosynthesized in the pores of alumina template. Martin and co-workers have

successfully synthesized polypyrrole nanofibers in the template and demonstrated their high charge transport rate than a conventional film under same conditions[125]. In our group, we have successfully electrodeposited PEDOT (Scheme 2.1)[152], polypyrrole nanotube with diverse inner morphologies (from hollow nanotubes to solid nanowires) to develop fast color switching electrochromic devices[153] and supercapacitors[109,154].

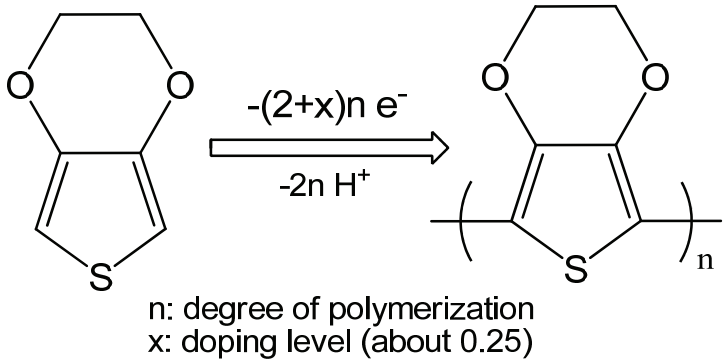

Scheme 2.1 Electropolymerization of EDOT monomer into PEDOT conductive polymer

2.2.2 Sol-Gel Method

Sol gel technology starts from 1970s when scientist attempted to find low temperature routes to glass synthesis. As a powerful approach, it was then extended to synthesize other inorganic materials such as metal oxides, semiconductor, and ceramics[155]. This method for the synthesis of inorganic materials has a number of advantages over more conventional synthetic procedures. For example, high-purity materials can be synthesized at a lower temperature. In addition, homogeneous multi-component systems can be obtained by mixing precursor solutions; this allows for

easy chemical doping of the materials prepared. Such a versatile deposition technique partners well with the template synthesis nanofabrication method.

Colloidal dispersions were prepared using appropriate sol-gel processing techniques. The template was immersed in a stable sol for various periods of time. Shorter immersion time may result in the formation of nanotubes. The capillary force drives the sol into the pores if the sol has good wettability for the template. After the pores were filled with sol, the template was withdrawn from the sol and dried. The sample was fired at elevated temperatures to yield a more crystalline product.

Martin's group has successfully fabricated silica nano test tubes using sol gel method[156]. In our group, we use a slight different approach to synthesized silica nanotubes. This approach is based on the hydrolysis of $SiCl_4$ on the surface of the alumina walls.

2.2.3 Chemical Vapor Deposition Method (CVD) and other methods

In a typical CVD process, the substrate is exposed to one or more volatile precursors, which react and/or decompose on the substrate surface to produce the desired deposit. This method is especially usefully for the fabrication of carbon nanotubes arrays in the alumina template, which involves placing alumina membrane in a high-temperature furnace and passing a gas such as ethane or propene through the membrane. Thermal decomposition of the gas occurs throughout the pores, resulting in the deposition of carbon films along the length of the pore walls. (i.e. carbon nanotube are obtained within the pores[97].)

Atomic Layer Deposition (ALD)

ALD is a process in which a precursor chemical in vapor form reacts with a surface until a monolayer has been chemisorbed. Once the sample surface is saturated with a monolayer of molecules the reaction stops and is self-limiting. Due to the above features, ALD has recently been applied to fabricate nanotubes with well control thin walls in the alumina template[157,158].

Other methods

Besides the above methods, there are many other methods used in template synthesis. Some materials can be fabricated in the alumina template via confined chemical reaction or bonding interactions in pores of the membrane. For example, Au nanotubes can be fabricated by electroless deposition of gold on the pore walls of alumina template. Biomaterials such as DNA nanotubes can be layer by layer assembled into nanotubes via α,ω-diorganophosphonate (α,ω -DOP) Zr(IV)chemistry[159].

Polymers such as polyaniline and PMMA can be chemical polymerized into the template as well. Physical methods can also be used to fabricate nanostructures with the assistance of alumina template. For instance, non-conductive polymer nanotube or nanowires can be synthesized in the alumina template by filling the melting polymer or its solution into the pores[160]. Metallic nanorings[130,131] or nanodots[132] can be fabricated by simply sputtering or evaporations metals on the entrances of the pores in the template. These synthetic methods can be combined to fabricate more complicated nanostructures such as coaxial nanowires[81,109,129], segmented nanowires[161-165], etc.

2.3 Template synthesis based on the different nanostructures

Template synthesis can be used to fabricate various nanostructures via different synthetic routes and synthetic conditions.

2.3.1 Nanowires (Nanorods) and Nanotubes

Nanowires and nanotubes are the mostly common forms of nanostructures fabricated by the template synthesis. The formation of these morphologies can depend on the synthetic route. For instance, CVD method and ALD method usually generate nanotubes, while electrochemical deposition method mostly generates solid nanowires. Also, these morphologies can also be controlled by tuning the synthetic conditions. For example, by controlling the electrochemical potentials during the conductive polymer synthesis, we can fabricate solid nanowires or nanotubes. Silica nanotubes with different wall thickness can be synthesized by controlling the sol-gel conditions (sol concentrations, pH, time, etc).

2.3.2 Heterogeneous Nanostructures

Template synthesis is widely used in fabricating heterogeneous nanostructures such as composite nanowires, segmented nanowires, and coaxial nanowires. (Figure 2.7)

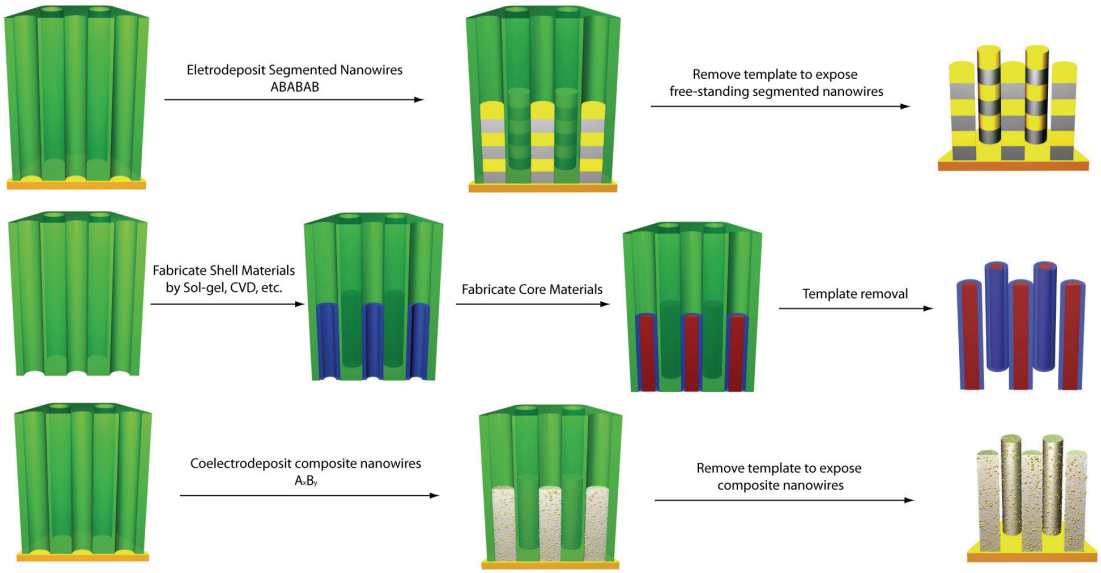

Figure 2.7 Heterostructured nanomaterials fabricated by AAO template synthesis

Composite nanowires or hybrid nanowires such as metal alloy can be coelectrodeposited by in a single electrochemical bath. One good example is the synthesis of Au/Ag alloy nanowires by Pearson's group[166]. The Ag part can be selectively etched to leave porous gold nanowires. Hybrid nanowires such as MnO_2 nanoparticles enriched PEDOT nanowires can be fabricated by soaking PEDOT nanowires in $KMnO_4$, the details of which are described in Chapter 8.

Segmented metal nanowires can be fabricated by subsequent electrodeposition of different materials in a single bath or alternating bath[161]. These metallic multisegmented nanowires have been studied as magnetic materials as well as barcodes for bioanalysis[161]. Segmented nanowires that contain heterojunctions between metal and semiconductor[167] or conductive polymers[163] have also been fabricated and studied for their properties.

Coaxial nanowires can be synthesized via step-wise routes, which includes fabricate shells on the existing nanowires by surface modification or functionalization and fill the nanotubes with inner materials. For example, Mallouk and coworkers has successfully functionalized metal nanowire with layer-by-layer deposition of ZnO-PSS[168,169]. Also, they have successfully coaxial nanowires by first coating the alumina membrane walls with silica then fill the voids with metals as cores[170]. In our group, we have successfully synthesized coaxial nanowires by one-step electrochemical deposition method, which will be discussed in detail in Chapter 6.

2.4 Application of Nanomaterials by Template Synthesis

As other nanomaterials, template synthesized nanomaterials have been found useful in many different applications, which is impossible to be discussed in detail in this thesis. Well-known examples include the applications of electroanalytical (e.g. nanoelectrodes)[171-173], bioanalytical (e.g. biosensors[174,175], bioseparation[176]), optics (photonic crystals[177]), magnetic (giant magnetoresistance[127,178]), biomedical (drug delivery[179,180]) and electrochemical energy conversion (fuel cells[181,182]) and storage (supercapacitors[43,109], lithium ion batteries[96]). The electrochemical energy storage using template synthesis nanomaterials will be the main theme focused in the following chapters.

Chapter 3: Experimental Setups for Template Synthesis

3.1 Fabrication of Alumina Template

Currently, much effort has been undertaken to develop an effective technologically simple method used for the synthesis of nanostructures over a macroscopic surface area. Today, the research spotlight is especially focused on self-organized nanostructured materials with a periodic arrangement of nanopores due to the high expectations regarding their applications. A highly desired densely packed hexagonal array nanoporous structure can be obtained by anodization, which is a relatively easy process for nanostructured material fabrication. The electrochemical formation of self-organized nanoporous structures produced by the anodic oxidation of semiconductors or metals, except aluminum, has been reported for only a few materials such as Si[183] and Ti[184,185] etc. During recent years, the anodization of aluminum, due to its great commercial significance, represents one of the most important and widespread method used for the synthesis of ordered nanostructures consisting of close-packed cells in a hexagonal arrangement with nanopores at their centers.

The anodizing of aluminum has also raised substantial scientific and technological interest due to its diverse applications which include dielectric film production for use in electrolytic capacitors, increasing the oxidation resistance of materials, decorative layers by incorporation of organic or metallic pigments during the sealing of anodized materials, and increasing abrasion wear resistance. A self-organized process that occurs during the anodization of aluminum in acidic electrolytes has become one of

the most frequently employed methods for the synthesis of highly ordered nanostructures.

3.1.1 General Structures of Alumina Template

The specific nature of a porous oxide layer on aluminum has attracted scientific attention over several decades, and determined fully the present applications of anodized aluminum in nanotechnology. Self-organized anodic porous alumina grown by the anodization of aluminum can be represented schematically as a closed-packed array of hexagonally arranged cells containing pores in each cell center (Figure 3.1). High-ordered nanostructures are often characterized by given parameters such as a pore diameter, wall thickness, barrier layer thickness and interpore distance (cell diameter). The uniform pore diameter, which is easily controllably by altering the anodizing conditions, can range from a few nanometers to hundreds of nanometers. The depth of fine parallel channels can even exceed 100 μm, a characteristic which makes anodic porous alumina one of the most desired nanostructures with a high aspect ratio and high pore density. A parallel growth of controlled dimensional pores can proceed throughout the complete anodized material.

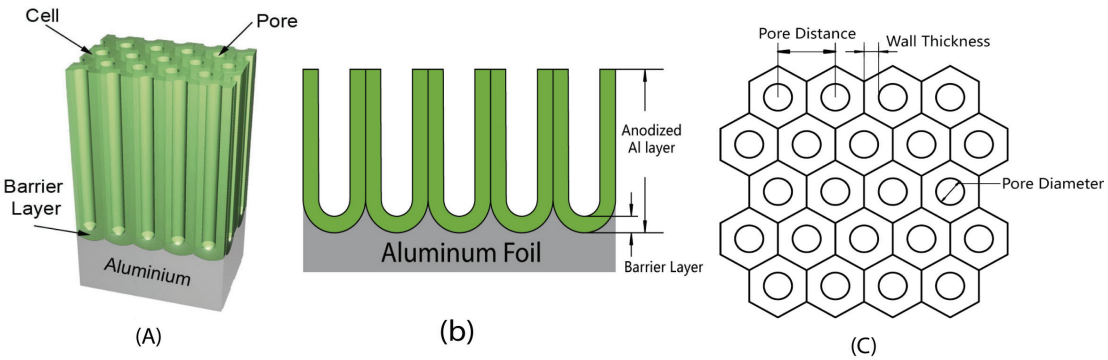

Figure 3.1 General structures of alumina template (a) 3-D view (b) side view (c) top view

(1) Pore Diameter

Generally, for the anodic porous alumina structure, the pore diameter is linearly proportional to the anodizing potential with a proportionality constant λ_p of approximately 1.29 nmV^{-1}:[186]

$$D_p = \lambda_p \cdot U \tag{3.1}$$

where D_p is a pore diameter (nm) and U denotes an anodizing potential (V). The dependence of the diameter on the voltage is not sensitive to the electrolyte. In describing the anodic porous alumina structure, researchers usually list the outer layer of oxide close to the surface, and the inner layer close to the pore bottoms. The diameter of pores in the inner oxide layer does not change significantly with anodizing time. A higher diameter of pores observed in a region close to the film surface is the result of an irregular initial growth of the pores during the very early stages of pore development, and their further reorganization in a hexagonal arrangement. It should be noted that an enhanced chemical dissolution of oxide, resulting in the development of widened pores, may occur also during anodizing at a sufficiently high temperature, or in strong acidic solutions. The solvent chemical action along the cell walls, and especially in the outer oxide layer, increases the diameter of pores measured at the surface of the anodic film.

(2) Interpore Distance

It is generally accepted that the interpore distance of anodic porous alumina is linearly proportional to the forming potential of the steady-state growth of anodic porous alumina with a proportionality constant λ_c of approximately 2.5 nmV^{-1}:[187]

$$D_c = \lambda_c \cdot U \tag{3.2}$$

(3) Wall Thickness

Among other morphological features of anodic porous oxide described by Keller et al.[188], a wall thickness per appears to be of importance.

The transformation of Eq. (3.1) gives the following form for the wall thickness calculation:

$$W = \frac{D_c - D_p}{2} \tag{3.3}$$

(4) Barrier Layer Thickness

During the anodization of aluminum, a very thin, dense and compact dielectric layer is formed at pore bases. The barrier layer has the same nature as an oxide film formed naturally in the atmosphere, and allows the passage of current only due to existing faults in its structure. The existing compact barrier layer at the pore bottoms makes the electrochemical deposition of metals into pores almost impossible. On account of this limit, the thickness of the barrier layer is extremely important and can determine any further applications of nanostructures formed by the anodization of aluminum. The thickness of the barrier layer depends directly on the anodizing potential. The dependence is about 1.3–1.4 nmV^{-1} for barrier-type coatings, and 1.15 nmV^{-1} for porous structures[189]. Nielsch et al.[187] suggested that for optimum self-ordering conditions of anodizing, leading to a 10% porosity of the nanostructure and perfect

hexagonal arrangement of nanopores, the barrier layer thickness is proportional to the interpore distance as follows:

$$B \cong \frac{D_c}{2} \tag{3.4}$$

(5) Porosity

The porosity of nanostructures formed by aluminum anodizing depends heavily on the rate of oxide growth, the rate of chemical dissolution of oxide in acidic electrolyte, and anodizing conditions such as: the type of electrolyte, the concentration of electrolyte, time of anodization, anodizing potential, and temperature. The most important factor governing the porosity of the structure is the anodizing potential and pH of the solution. There is a great inconsistency among experimental data on the porosity of nanostructures, with the estimated porosity of anodic porous alumina varying from about 8% to 30%, and even more. An exponential decrease in porosity with increasing anodization potential has been reported for anodizing in sulfuric acid and oxalic acid[190]. A decrease in the porosity of nanostructures with increasing anodizing potential has been observed for constant potential anodizations conducted in sulfuric, oxalic, phosphoric, and chromic acids. On the other hand, a slight increase in porosity is observed with increasing anodizing potential for anodization carried out in sulfuric acid. As might be expected, the porosity of nanostructures may also be affected by the anodizing time, an extension of which usually results in increasing porosity of the nanostructure formed in tetraborate and phosphoric acid solutions. Increasing the anodizing temperature decreases the porosity of the nanostructure formed in oxalic acid; the opposite effect has been observed in sulfuric acid.

The porosity is defined as a ratio of a surface area occupied by pores to the whole surface area. For a single regular hexagon with one pore inside, the porosity formulation can be written as follows:

$$\alpha = \frac{S_{pores}}{S} = \frac{S_p}{S_h} \tag{3.5}$$

Assuming that each single pore is a perfect circle, the following equations for S_p and S_h can be further evolved:

$$S_p = \pi \cdot \left(\frac{D_p}{2} \right)^2 \tag{3.6}$$

$$S_h = \frac{\sqrt{3} \cdot D_c^2}{2} \tag{3.7}$$

Substitution of Eqs. (3.6) and (3.7) into Eq. (3.5) leads to the following expression for the porosity of a nanostructure with hexagonally arranged cells:

$$\alpha = \frac{\pi}{2\sqrt{3}} \bullet \left(\frac{D_p}{D_c} \right)^2 = 0.907 \bullet \left(\frac{D_p}{D_c} \right)^2 \tag{3.8}$$

(6) Pore Density

The highly ordered nanomaterial with a close-packed arrangement of nanopores or nanotubes is seen as an "object of desire" for the microelectronics industry. Due to the hexagonal symmetry of the cells, anodic porous alumina is a nanostructure with the highest packing density, and consequently the number of pores created during anodization represents one of the most important features of porous alumina. For the hexagonal distribution of cells in the nanostructure, the density of pores defined as a total number of pores occupying the surface area of 1 cm^2 is expressed by

$$n = \frac{10^{14}}{P_h} = \frac{2 \bullet 10^{14}}{\sqrt{3} \bullet D_c^2}$$

(3.9)

where P_h is a surface area of a single hexagonal cell (in nm^2) and D_c is given in nm. The substitution of D_c by Eq. (3.2) leads to the expression as follows:

$$n = \frac{2 \bullet 10^{14}}{\sqrt{3} \bullet \lambda_c^2 U^2} \cong \frac{18.475 \bullet 10^{12}}{U^2}$$

(3.10)

3.1.2 Anodizing of Aluminum into Anodic Porous Alumina Structure

(1) **Incorporation of Anions**

The incorporation of anions into the structure of anodic oxide layer depends heavily on the film type of the formed oxide. The formation of porous alumina during anodizing leads to a higher anion content in the structure than for barrier-type coatings. It is generally accepted that incorporated electrolyte species are present in the oxide films in a form of acid anion derived from the electrolyte used for anodizing[191]. Published data show an agreement with respect to the content of incorporated acid anions in the bulk of the oxide layer. Over the past few decades, much research effort has been focused on the determination of profiles of incorporated anions along the width of the oxide layer thickness. A wide variety of techniques has been employed for a depth profiling analysis of the barrier-type oxide layer, including Auger electron spectroscopy (AES), impedance measurements, Rutherford backscattering spectroscopy (RBS), secondary ion mass spectrometry (SIMS), electron probe microanalysis (EPMA), glow discharge optical emission

spectroscopy (GDOES), and X-ray photoelectron spectroscopy (XPS). An excellent review on methods used to study the distribution of incorporated anions in anodic oxide layers was prepared by Despić and Parkhutik[192], in which the kinetics of anion incorporation into the growing alumina films was also discussed.

(2) Cell-Wall Structure

The properties of porous alumina films formed by anodizing are related to the electrolyte species incorporated into the oxide walls. For instance, the incorporation of anions modifies space charge accumulation in the porous and barrier-type alumina films[192]. Moreover, the mechanical properties of anodic alumina films, including flexibility, hardness and abrasion resistance, are greatly influenced by the incorporation of anions. The content of incorporated species, and their distribution, depend on the anodizing conditions such as anodizing potential/current density and temperature. Consequently, different wall structures can be expected at different anodizing conditions. The duplex structure of the cell walls (Figure 3.2) was proposed by Thompson et al.[191], whereby two different regions – the inner layer containing relatively pure alumina and outer layer with incorporated electrolyte anions – were distinguished. It was reported that the thickness of the inner layer increases in the order:

$H_2SO_4 < C_2H_2O_4 < H_3PO_4 < H_2CrO_4$

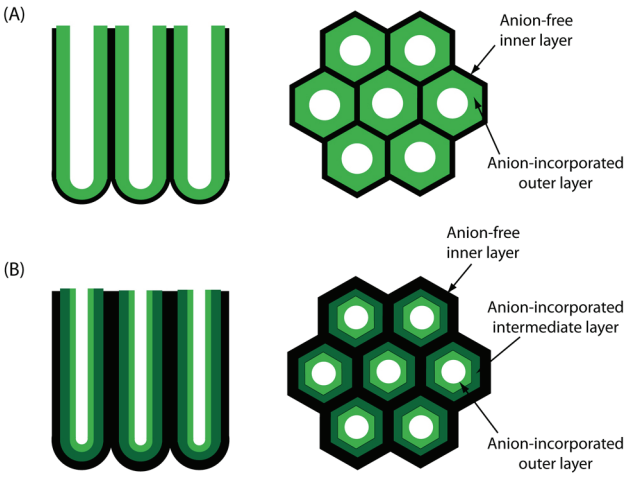

Figure 3.2 Schematic representations of the sectional and plan views of the duplex (A) and triplex (B) structures of porous alumina cell-walls formed in sulfuric and phosphoric acid, respectively.

The formation of voids in the anodic alumina layer has been reported elsewhere[193]. Ono et al.[193] reported voids on the apexes of aluminum protrusions at the oxide/metal interface in the inner layer of cell walls (see Figure 3.3). These authors suggested that this occurred due to oxygen evolution, to existing tensile stress in the film, or to electrostriction pressure. The size of voids formed in the oxide layer were also found to increase with increasing anodizing potential. Moreover, the formed voids could enlarge and merge under electron beam irradiation.

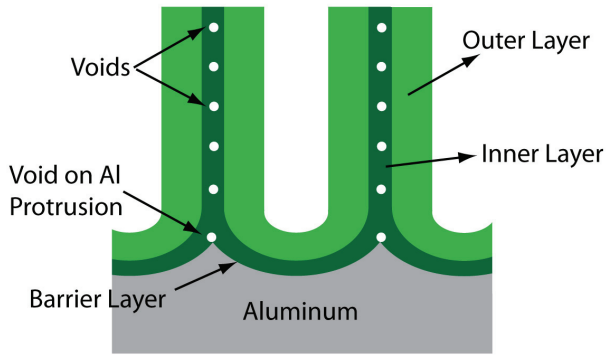

Figure 3.3 Voids in anodic porous alumina film.

3.1.3 Kinetics of Self-Organized Anodic Porous Alumina Formation

(1) Anodizing Regimes and Current/Potential-Time Transient

Hexagonal-shaped oxide cell can easily be formed by anodizing aluminum at a constant current density or constant anodizing potential regime. A typical current density–time and anodizing potential–time transient recorded during the anodization of aluminum in 20% H_2SO_4 at 1 °C are shown in Figure 3.4. When a constant current is applied for porous alumina growth, the potential rises linearly with time until the local maximum is reached, and then decreases gradually to the steady state forming potential. During the initial period of anodization (Figure 3.4, stage a), the linear increase in potential is associated with a linear growth of high-resistant oxide film (barrier film) on aluminum. Further anodizing (stage b) results in the propagation of individual paths (pores precursors) through the barrier film. At the maximum of potential (stage c), the breakdown of the tight barrier film occurs and the porous structure begins to be built. Finally, the steady-state growth of porous alumina proceeds (stage d) and a forming potential is almost unchanged. At the start of the process conducted under the constant anodizing potential, current density decreases rapidly with time, and a minimum of current density is quickly achieved. A linear increase then leads to a local maximum. After reaching the maximum, the current density decreases slightly and a steady-state current density of the porous oxide formation is achieved.

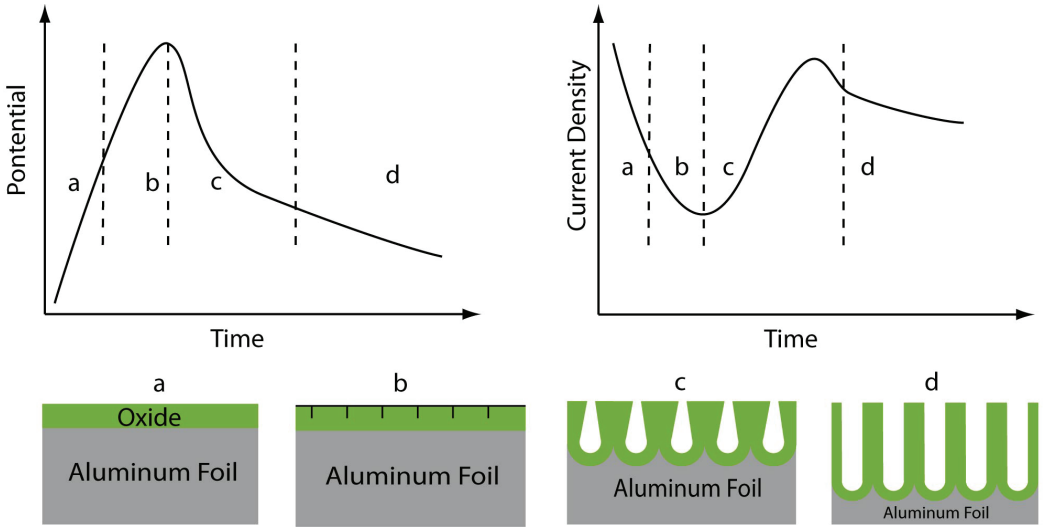

Figure 3.4 Schematic illustration of the kinetics of porous oxide growth in galvanostatic (A) and potentiostatic (B) regimes, together with stages of anodic porous oxide development (C).

(2) Pores Initiation and Porous Alumina Growth

The phenomena of anodic porous alumina film formation has been studied extensively over several decades, with considerable scientific effort directed towards elucidation of the mechanism of self-organized growth of the porous layer. Thus, several theories have been proposed and developed[194]. Although the anodizing of aluminum was successfully and widely applied for the synthesis of high-ordered nanostructures, it remains unclear as to which physical factors control pore ordering during oxide growth, and especially how the surface features of the aluminum affect the ordering of pores.

(3) Volume Expansion: The Pilling–Bedworth Ratio (PBR)

The volume expansion of an anodic porous alumina, R, known also as the Pilling–Bedworth ratio (PBR), is defined as the ratio of the volume of aluminum oxide, which is produced by anodizing process, to the consumed aluminum volume:

$$R = \frac{V_{Al_2O_3}}{V_{Al}} = \frac{M_{Al_2O_3} \bullet d_{Al}}{2 \bullet M_{Al} \bullet d_{Al_2O_3}} \tag{3.11}$$

where:$M_{Al_2O_3}$ is the molecular weight of aluminum oxide, M_{Al} the atomic weight of aluminum, d_{Al} and $d_{Al_2O_3}$ are densities of aluminum (2.7 g cm^{-3}) and porous alumina (3.2 g cm^{-3}), respectively. The theoretical value of the PBR for porous alumina formation with a 100% current efficiency is 1.6. Therefore, the aluminum specimen volume increases significantly during anodizing (see Figure 3.5).

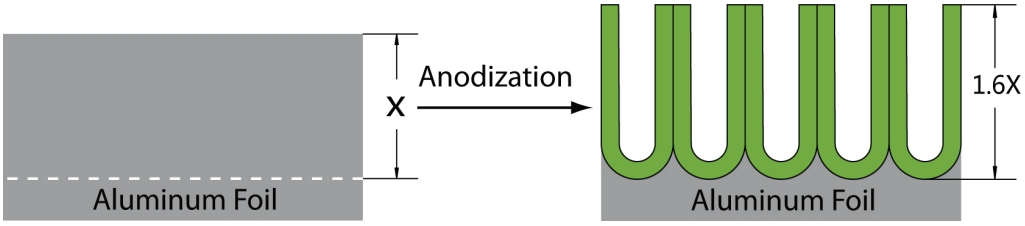

Figure 3.5 Volume expansion observed during anodization of aluminum.

3.2 Two Step Anodizations

The process of alumina template formation by anodization is relatively simple and results in a high density of parallel nanopores. Hence, anodic porous alumina (AAO) is a key template material for the fabrication of various nanostructured materials. In general, there are two widely used methods of AAO template synthesis: (i) a self organized, two-step anodization leading to a quasi-monodomain structure; and (ii) a prepatterned-guided anodization resulting in a perfectly ordered pore lattice. A flow diagram of the self-organized formation of anodic alumina membranes by the anodization of aluminum with a typical two-step anodizing procedure is presented in Figure 3.6. The formation of nanopores by self-organized anodizing of aluminum is a multistage process consisting of a pre-treatment, anodizing, and post-treatment steps.

The pre-treatment procedure includes annealing of aluminum foil in a nonoxidizing atmosphere, degreasing of samples, and electropolishing. The two-step anodizing procedure is usually based on the initial anodizing at the pre-selected cell potential and subsequent chemical etching of the grown aluminum oxide layer.

Following the chemical removal of oxide, a periodic concave triangular pattern formed on the aluminum surface acts as self-assembled masks for the second anodizing. The second anodization is conducted at the same cell potential as used during the first anodizing step. Finally, the synthesized hexagonally arranged nanopore structure can be removed from the base aluminum, and the pores may be opened and widened.

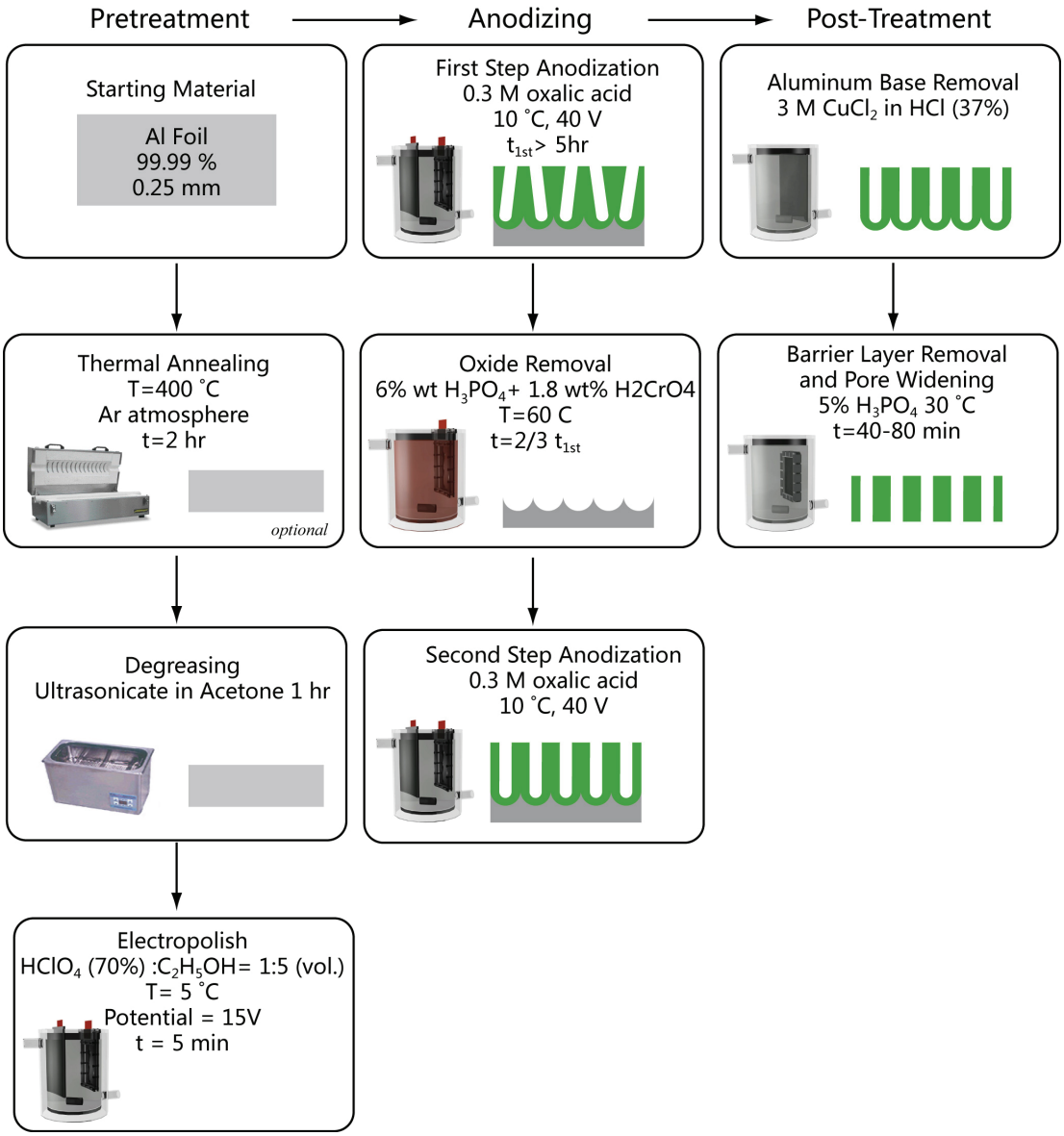

Figure 3.6 Two step anodizations for the fabrication of alumina template

3.2.1 Aluminum Pre-Treatment

The quality of aluminum substrates and their surface pre-treatment have major influences on the surface nanostructuring by self-organized anodizing. The structure of a pre-existing film on the aluminum surface, which may develop in air, thermally or during chemical and electrochemical treatment, depends on the applied pre-treatment procedure. During the self-organized anodizing of aluminum, the process of

pore nucleation is a combination of random nucleation and nucleation at surface faults. Moreover, the grain boundaries and scratches on the aluminum surface are sites for preferential pore development[195]. The pre-treatment process control must be focused on the reduction of surface faults, or on their controlled and reproducible generation, in the required morphology. Therefore, the most desirable starting material for self-organized nanopore array formation by anodizing is a high-purity, annealed aluminum foil. The annealing of foil reduces stresses in the material and increases the average size of the grain, which is usually more than 100 μm. The typical annealing of aluminum foil is conducted under an argon or nitrogen atmosphere at 400 or 500 °C for 3–5h.

The degreasing and polishing of Al samples is then carried out before anodizing. Among various solvents used for degreasing, acetone and ethanol are commonly employed. Due to their moderate or high carcinogenicity, dichloromethane, trichloroethylene, benzene and methanol have been used only sporadically.

The immersion of samples in 5% NaOH at 60 °C for 30 s or 1 min and subsequent neutralization in a 1:1 HNO_3:H_2O solution for several seconds was also proposed for Al degreasing and cleaning. A mixed solution of HF:HNO_3:HCl:H_2O (1:10:20:69) was also proposed for degreasing and cleaning of the aluminum surface before anodizing, leading to a highly ordered, self organized nanopore array. It should be noted that electrochemical polishing in a 60% $HClO_4$:C_2H_5OH (1:4, v/v) solution at 10 °C and 500 $mAcm^{-2}$ for 1 min is commonly used to prepare smooth Al surfaces before anodizing.

3.2.2 Self-Organized Anodizing of Aluminum

The self-organized growth of ordered pores on anodized aluminum occurs within a relatively narrow window of experimental conditions. Generally, a mild anodizing process leading to porous alumina formation is conducted at low temperatures and employs mainly sulfuric, oxalic, and phosphoric acids as an electrolyte. Figure 3.7 show the experimental setup for the Al foil in our lab. Basically, the alumina foil is sandwiched between two pieces of silicon rubber and tightened by two frames of polycarbonate as the working electrode (Figure 3.7) while the counter electrode is simply composed of a stainless steel plate. A stirring bar is placed at the bottom of the beaker to circulate the electrolyte inside the beaker, which allows the even anodization and heat dissipation. The working and counter electrodes are assembled in a parallel manner in a jacket beaker, which can circulate the water and maintain electrolyte temperature (Figure 3.8). For each electrolyte, there is a certain range of potential which can be applied for anodizing without burning or breakdown of the oxide film. Moreover, there is a certain value of the anodizing potential (self-ordering regime) at which, the best arrangement of nanopores is observed. When anodizing is conducted under different values of anodizing potential, the degree of pore ordering is reduced drastically. The temperature of electrolyte and alcohol addition have no influence on the self ordering regime for the certain anodizing electrolyte. In mild, self-organized anodization, the rate of oxide growth is low due to the low current density, and the highest or most moderate rate of oxide growth is observed in sulfuric acid. More recently, hard anodizing (also known as a high-field anodizing) has been

successfully applied for self-organized oxide formation[196]. In this process the range of anodizing potential and self-ordering values of potentials differ widely.

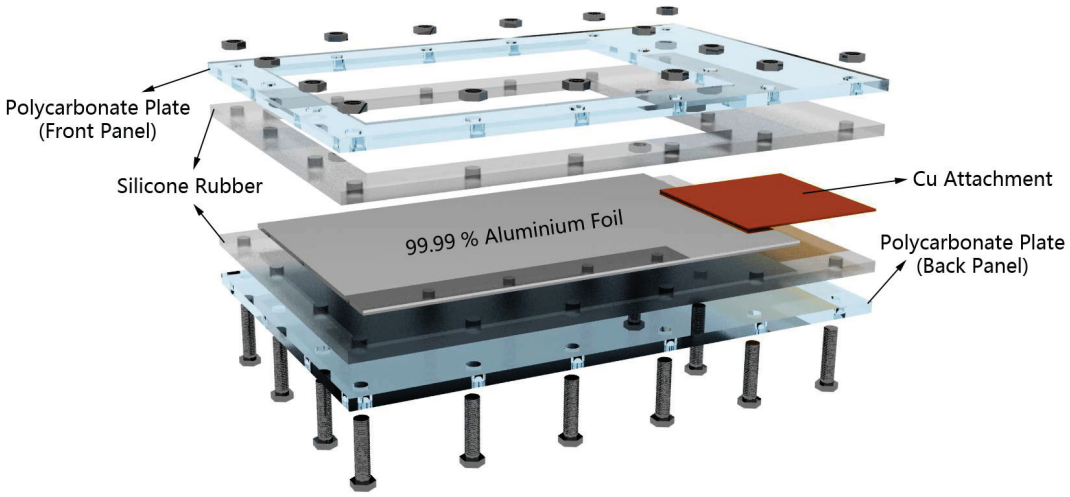

Figure 3.7 Setup of the working electrode for the Al foil anodization

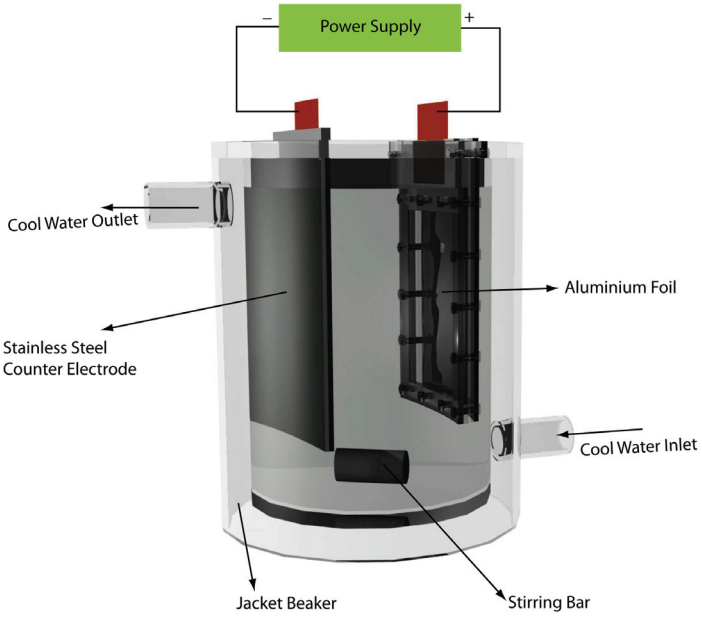

Figure 3.8 Setup for the Al foil anodization in jacketed beaker.

Today, a two-step anodizing procedure is commonly used for the formation of high-ordered arrangements of nanopores by anodizing aluminum in sulfuric, oxalic, or

phosphoric acid. Following an initial anodization at the pre-selected cell potential, chemical etching of the grown aluminum oxide layer is carried out in a mixed solution containing H_3PO_4 (6 wt.%) and H_2CrO_4 (1.8 wt.%) at a temperature of 60–80 °C A slightly modified composition of solution consisting of 0.4 or 0.5M H_3PO_4 and 0.2M H_2CrO_4 was also proposed for the oxide removal. The time required for the chemical etching of oxide depends heavily on the thickness of the oxide film grown during the first anodization, and can vary from a few minutes to several hours. It should be noted that the rate of oxide growth during anodization depends significantly on the anodizing electrolyte, with the highest rate being observed for sulfuric acid anodizing. A completely different method for the removal of oxide formed during the first-step of anodization was proposed by Schneider et al.[197] This method employs a voltage detachment procedure, whereby a reverse voltage is applied to the anodized sample (the value of the reverse voltage is the same as was used for the anodization). Such a voltage detachment procedure allows the production of a fully flexible anodic porous alumina membrane, as opposed to oxide removal by chemical etching. The enhanced mechanical flexibility of the membrane is an undeniable advantage of the voltage detachment procedure over the chemical etching. One application of the electrochemical voltage pulse technique for the effective detachment of oxide layer at various electrolytes was investigated systematically[198]. The procedure results in a freestanding detached AAO membrane with open pores. The proposed mechanism of the pulse detachment involved oxide removal independently of the applied procedure, and resulted in the formation of a periodic concave pattern on the aluminum surface, which acted as a mask for the second anodizing. Following oxide removal, a second

anodization is carried out at the same anodizing potential as used for the first anodization.

3.2.3 Post-Treatment of Anodic Porous Alumina

Anodic porous alumina films with a regular arrangement of nanopores have been widely used as templates for the fabrication of other nanomaterials. Therefore, AAO films fabricated by self-organized anodization are usually subjected to an optional further post-treatment procedure which included removal of the aluminum base, removal or thinning of the barrier layer, and re-anodizing. In order to detach the aluminum oxide from the remaining aluminum base, an electrochemical detachment method employing a reversal and pulse voltage techniques can be used. The separation of aluminum oxide from the remaining aluminum substrate might also be performed by using electrochemical etching in 20% HCl, with an operating potential between 1 and 5 V. However, the most widespread method is based on a wet chemical removal of aluminum. For this procedure, the unoxidized aluminum substrate is usually dissolved by immersing an anodized sample for a few hours in a saturated $HgCl_2$ solution. Another effective way is to soak the unoxidized aluminum in the solution of 0.2 M $CuCl_2$ in 36% HCl. A brief sonication needs to be applied to remove the copper that may stick onto the alumina template.

Indeed, following removal of the aluminum substrate, the spherical pore bottoms can be observed. The AAO template preparation consists of pore opening after separation of the oxide from the Al substrate, or pore widening before the subsequent deposition of metals and semiconductors into pores. Removal of the barrier layer in a separated AAO membrane, formed by self-organized anodization, is usually carried

out by chemical etching of the oxide. The nanopore bottoms are opened by immersing in a H_3PO_4 solution, with the opening time depending directly on the barrier layer thickness, and consequently on anodizing conditions.

If the opening time is prolonged, the widening of pores can occur simultaneously. The diameter of the opened pores can be adjusted by changing the time of the chemical etching treatment in a phosphoric acid solution. Pore opening and widening were studied in detail by Xu et al.[199] Samples before widening treatment were anodized in 0.3M $H_2C_2O_4$ at 40 V and 12 °C. The dissolution rate of the barrier layer in 0.5M H_3PO_4 was found to be approximately 1.3 nm/min, and to decrease inside the columnar pore channel with increasing pore depth. The horizontal and vertical dissolution rates were also distinguished. The horizontal rate of oxide dissolution is mainly responsible for barrier layer removal, whereas the vertical rate plays a key role in the widening of pores and nanopore thickness reduction. A different etching technique using a reactive ion-beam (mainly Ar^+) was also proposed for removal of the barrier layer in anodic porous alumina[200]. Most importantly, it should be noted that dry etching by ion-beams requires the use of a sophisticated apparatus. In order to obtained an array of ordered nanopores with a desired pore diameter, it is important first to carry out a widening treatment.

3.3 Electrochemical Synthesis of Nanomaterials in Alumina template

3.3.1 General Setup for three electrodes electrochemical cells

(1) Working Electrode

As mentioned earlier, one face of AAO membrane has to be coated with metal film to serve as the working electrode in the electrochemical cell. For home-made membrane, it doesn't matter which face is chosen to be coated. However, for the commercial membrane which purchased from Whatman, the metal is usually sputtered on the O-ring support side (branched side) (Figure 3.9) because the other side often have over-etched problems, which will make the nanomaterials connected and hard to be dispersed after template removal.

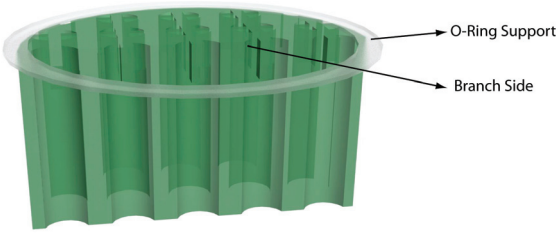

Figure 3.9 O-ring support on the commercial AAO template

In order to sputter metals such as Au or Pt, we use Denton Vacuum Desk III and Au or Pt foil as targets. Based on the sputtering rate (0.3-0.4 nm/s), 10 min deposition will give us around 200 nm metal film, which offers sufficient electrical conductivity, but not completely covers the pores if the pores size are over 200 nm. Ring structured electrode will be created (especially on the commercial 200 nm pore size membrane). These ring structured electrodes have important roles in directing the growth of conductive polymer nanotubes in the template. If the pores need to be completely closed, two methods can be utilized. The first one is by simply sputtering longer time such as 30 min. Another way is to electrodeposit Au nanorods first to seal the pores[201], which is more effective than longer sputtering (Figure 3.10).

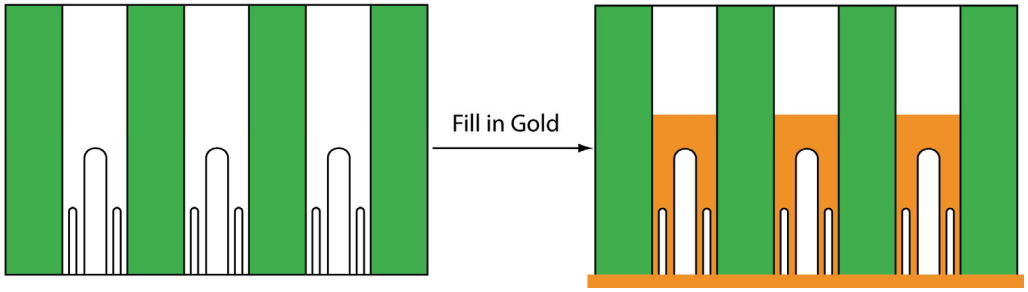

Figure 3.10 Removing branched structures by electrodeposition of Au nanorods

After the membrane has been sputtered metals, it has to been carefully cut and further assembled into working electrode, in order to confine the electrochemical deposition inside the channel of alumina template while not on the sputtered metals, the metal sputtered face of membrane has to be well insulated. In our lab, we use silicone rubbers to achieve this goal. Figure 3.11 is the schematic view of the working electrode assembly. The alumina template (with metal sputtered on one face) is sandwiched between two sheets of silicone rubber. One piece of the silicone rubber has to be punched with a hole to not only expose the alumina template to the electrolyte, but also fix the electrode area. A Teflon sheet with a bigger hole and a glass slides are attach onto the soft silicone rubber as mechanical support, finally the whole device is clamped using stainless clippers.

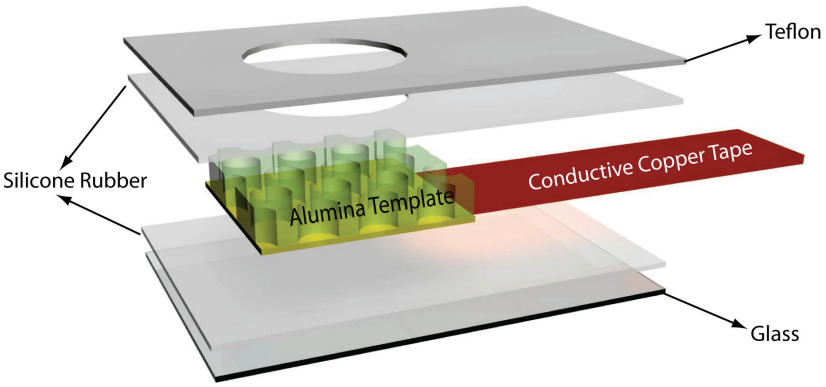

Figure 3.11 Assembly of working electrode for the electrochemical deposition in alumina template.

(2) Reference electrode:

The reference electrode used in this thesis is Ag/AgCl electrode, which has a standard potential of 0.197 V (v.s. standard hydrogen electrode) if the electrode are stored in saturated KCl solution. Figure 3.12 shows a typical scheme view of the Ag/AgCl reference electrode.

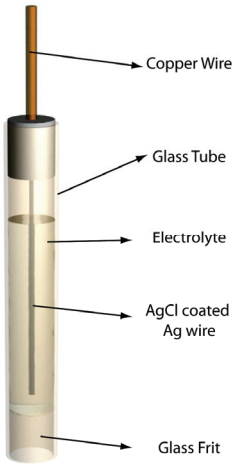

Figure 3.12 Reference electrode in the three electrode system for the electrochemical deposition in alumina template

(3) Counter electrode:

The counter electrodes in this thesis are simply made by stripes of platinum foil, which is chemical inert.

The working, reference, and counter electrode are subsequently immersed in a beaker that is filled in the electrolyte to compose a three electrode electrochemical cell.

3.3.2 Electrochemical Depositions of Various Materials

The principle of electrochemical synthesis of nanomaterials in alumina template has been described in details in chapter 1. In this section, we'll first list synthesis details of various materials based on their categories such as metals, metal oxide, conductive polymer, semiconductors (Table 3.1).

Categories	Materials	Electrolyte	Synthetic Conditions
Metals	Gold[202]	Commercial Available Gold plating solution Ortemp 24 from Technic. Inc	-0.9 V constant potential, or constant current -0.5 mA/cm^2
		10-20 mM $HAuCl_4$	0.2 V, or -0.3 mA/cm^2
	Nickel[127]	Nickel chloride	-0.85 V or -0.5 mA/cm^2
	Platinum[203]	20 mM K_2PtCl_6	0.2 V or -0.3 mA/cm^2
	Silver[204]	$AgNO_3$ in boric acid	0 V or -0.3 mA/cm^2
	Copper[205]	$CuSO_4$ in boric acid	-0.2 V or -0.5 mA/cm^2
Metal Oxide	MnO_2[109]	Manganese acetate	0.6 V or 0.5 mA/cm^2
	WO_3[206]	Na_2WO_4+H_2O_2+$HClO_4$	-0.25 V
	RuO_2[42]	50 mM $RuCl_3$	CV -0.2 V to 1 V at 50 mV/s
Conductive Polymer	PEDOT[152]	10-100 mM EDOT monomer, 0.1 M $LiClO_4$ in acetonitrile	1.2 V or 0.5 mA/cm^2
	polypyrrole[207]	10-100 mM pyrrole monomer, 0.1 M $LiClO_4$ in water	0.8 V or 0.5 mA/cm^2
	polyaniline[208]	0.1 M aniline 0.1 M sulfuric acid	0.6 V or 0.5 mA/cm^2
Semiconductor	CdSe[126]	0.2 M $CdSO_4$, 2 mM SeO_2 in acidic solution	-0.65 V
	CdTe[126]	0.2 M $CdSO_4$, 2 mM SeO_2 in acidic solution	-0.65 V

Table 3.1 Conditions for electrochemical depositions of various materials

The successful synthesis of nanomaterials in alumina template relies on a few important factors:

(1) Electrochemical Methods

Choosing proper electrochemical methods (potentiostatic, galvanostatic, cyclic voltammetry) and conditions (concentrations, time, charge, temperature, stirring, etc.) for the electrosynthesis is very important because it not only affects the growth speed of the nanomaterials but also it plays very important role in controlling the morphologies of the nanostructures. For example, our group has successfully controlled the synthesis of PEDOT nanostructures with different morphologies such as nanowires and nanotubes[152]. As mentioned earlier, two methods are often used in electrochemical deposition. The popular method is potentiostatic method. This method is very straightforward because the potential can be easily chosen based on the standard reduction or oxidation potential of the electroactive species in the electrolyte. For example, under the standard conditions, based on the standard reduction potential of Ag^+ (0.8 V), it is easy to know that the applied potential has to be less than 0.8 V in order to reduce the Ag^+ in to Ag. The difference between the applied potential and the standard potential is called overpotential, which drives the electrochemical reaction to occur. The amplitude of the overpotential and other parameters (such as species concentration, temperature, diffusions) determines the reaction rate of the electrochemical rate, which is corresponding to the current that can be measure dynamically and intergraded into the charge passed. The advantage of this potentiostatic method is that we can thermodynamically control the electrochemical reaction. One we fixed the potential (over potential), the current (reaction rate) will be determined by the concentration of the electrolyte. However, under non-standard conditions, or when the electrolyte contained complex species, it may be hard to choose appropriate potential. Under these circumstances, we need to

either experimentally determine the potential that can drive the electrochemical reaction by cyclic voltammetry method or we can use another method called galvanostatic method which can directly determined the reaction speed because a constant current will be applied. In this case, the potential will be automatically determined to maintain the current that has been applied. Similarly, the corresponding potential will be dynamically measured and monitored by the electrochemical workstation.

(2) **Electrochemical Conditions:**

Concentration: the concentration of the electroactive species is the most important parameter for the electrochemical synthesis. At a certain overpotential, higher concentration leads to higher reaction speed, which is corresponded to higher deposition rate. In addition, higher concentration (especially at lower potentials or low current) usually leads to the formation of more solid nanostructures, like nanowires. Lower concentration (especially at high over potentials or high current) may lead to the formation of more loosy, porous nanostructures or nanotubes, a lot of research has been done on this. (Figure 3.13) This phenomenon is usually because the diffusion of the species limits the electrochemical reaction[152].

Electrode Shapes: The ring shape electrodes which are resulted from the metal sputtering also play very important roles in the nanotube formation. (Figure 3.13) These ring shape electrodes can be modified into flat top electrode by first electrodepositing metals on the bottom of the template. Modifying these electrode shapes do have impact on the morphologies of grown nanomaterials. Detailed study can be seen in a paper published by our group[152].

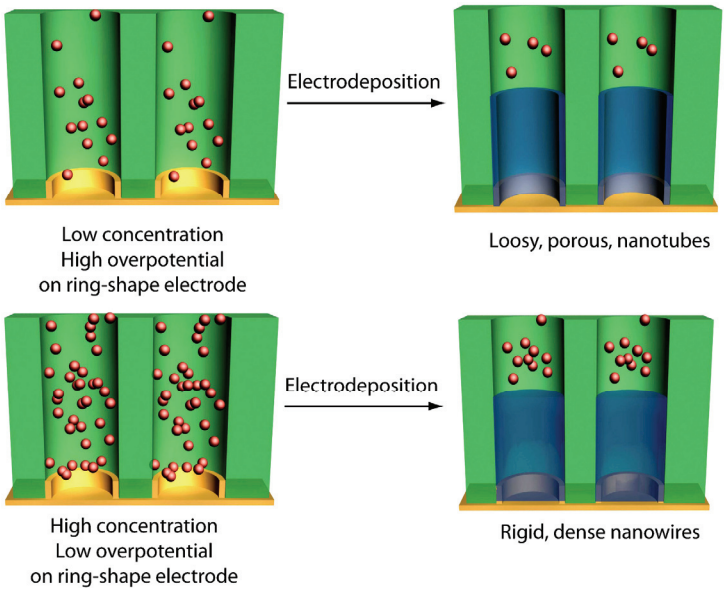

Figure 3.13 Impact of synthetic conditions on the morphologies of nanomaterials

Time and charge: the charge is continuously accumulated as the time goes by. Based on faraday law, the amount of material is determined by the charge passed. This will give us the control of the length of the 1-D nanomaterials we synthesized from the membrane.

Temperature: the temperature is another important parameter in controlling the reaction speed because high temperature leads to the faster diffusion of the electroactive species. In addition, the structures of the nanomaterials (e.g. crystalline structures) can also be affected.

Stirring: as we mentioned, when the electrochemical occurs at high overpotential in low concentration, the diffusion of the electroactive species may limit the electrochemical reaction. However, by stirring the solution will attenuate this problem by external disturbing the electrolyte to facilitate the diffusion of the electroactive species.

3.3.3 Characterizations of template Synthesized nanomaterials

The structures of the template synthesized nanomaterials are characterized by electrons microscopes. The chemical composition is analyzed by Energy dispersive X-ray analysis (EDS) or XPS. The electrochemical properties are characterized by different electrochemical methods performed by electrochemical workstations.

(1) Structures Analysis

Scanning electron microscope (SEM)

The scanning electron microscope (SEM) is a type of electron microscope that images the sample surface by scanning it with a high-energy beam of electrons in a raster scan pattern. The electrons interact with the atoms that make up the sample producing signals that contain information about the sample's surface topography, composition and other properties such as electrical conductivity. Figure 3.14 shows the Hitachi-2000 SEM used for the nanomaterials analysis in this thesis, which is located at NISP lab at university of Maryland.

Figure 3.14 Image of the Hitachi SEM used in NISP lab at University of Maryland

Figure 3.15 Image of the JOEL TEM used in NISP lab at University of Maryland

Transmission electron microscopy (TEM)

Transmission electron microscopy (TEM) is a microscopy technique whereby a beam of electrons is transmitted through an ultra thin specimen, interacting with the specimen as they pass through. An image is formed from the interaction of the electrons transmitted through the specimen, which is magnified and focused onto an imaging device, such as a fluorescent screen, as is common in most TEMs, on a layer of photographic film, or to be detected by a sensor such as a CCD camera. Figure 3.15 showed the Joel TEM used for the nanomaterials analysis in this thesis, which is located at NISP lab at university of Maryland.

Electron Diffraction Pattern

Electron diffraction is a technique used to study matter by firing electrons at a sample and observing the resulting interference pattern (Figure 3.16). Experiments are usually performed in a TEM. The periodic structure of a crystalline solid acts as a diffraction grating, scattering the electrons in a predictable manner. Working back

from the observed diffraction pattern, it may be possible to deduce the structure of the crystal producing the diffraction pattern.

For thin crystalline samples, this produces an image that consists of a pattern of dots in the case of a single crystal, or a series of rings in the case of a polycrystalline or amorphous solid material. For the single crystal case the diffraction pattern is dependent upon the orientation of the specimen and the structure of the sample illuminated by the electron beam. This image provides the investigator with information about the space group symmetries in the crystal and the crystal's orientation to the beam path.

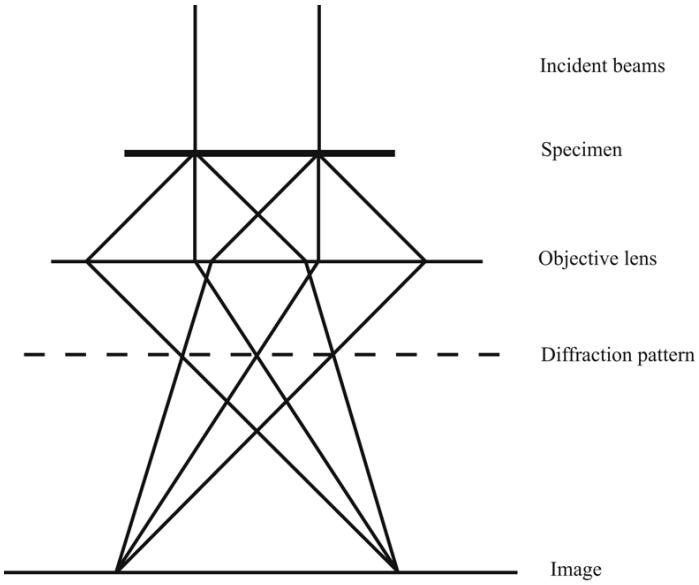

Figure 3.16 Electron Diffraction Patterns under TEM

(2) Chemical Information

EDS

EDS is an analytical technique which utilizes x-rays that are emitted from the specimen when bombarded by the electron beam to identify the elemental composition of the specimen. To explain further, when the sample is bombarded by

the electron beam of the SEM, electrons are ejected from the atoms on the specimens surface. A resulting electron vacancy is filled by an electron from a higher shell, and an X-ray is emitted to balance the energy difference between the two electrons. The EDS X-ray detector measures the number of emitted X-rays versus their energy. The energy of the X-ray is characteristic of the element from which the X-ray was emitted. A spectrum of the energy versus relative counts of the detected X-rays is obtained and evaluated for qualitative and quantitative determinations of the elements.

XPS

X-ray photoelectron spectroscopy (XPS) is a quantitative spectroscopic technique that measures the elemental composition, empirical formula, chemical state and electronic state of the elements that exist within a material. XPS spectra are obtained by irradiating a material with a beam of X-rays while simultaneously measuring the kinetic energy (KE) and number of electrons that escape from the top 1 to 10 nm of the material being analyzed (Figure 3.17). Figure 3.18 shows the XPS instrument in the Department of Chemistry at University of Maryland.

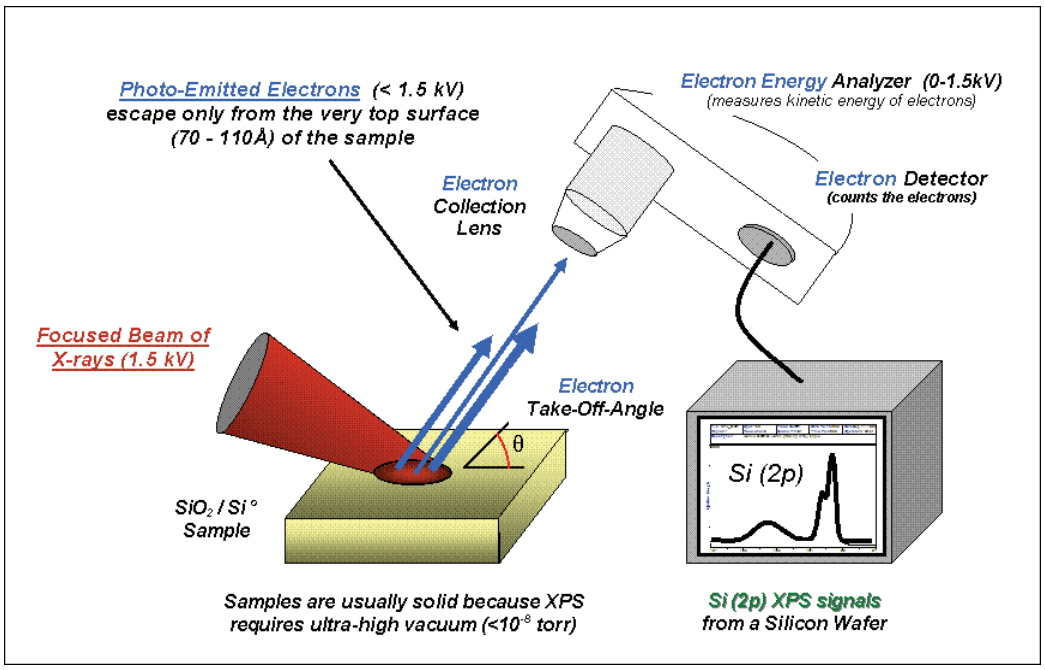

Figure 3.17 Schematic view of XPS analysis technique

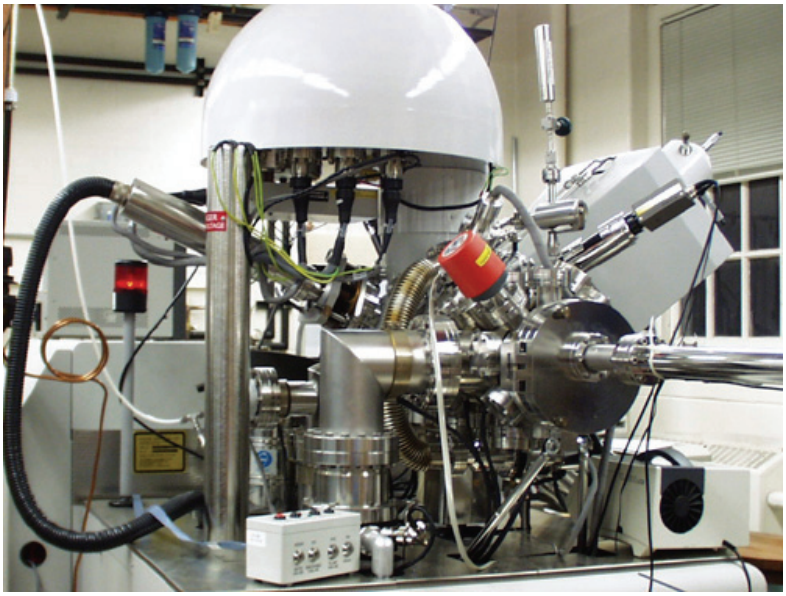

Figure 3.18 XPS equipment in Department of Chemistry at University of Maryland

(3) Electrochemical Characterization

Cyclic Voltammetry (CV)

Cyclic voltammetry or CV is a type of potentiodynamic electrochemical measurement. In a cyclic voltammetry experiment the working electrode potential is ramped linearly versus time like linear sweep voltammetry (Figure 3.19). Cyclic voltammetry takes the experiment a step farther than linear sweep voltammetry which ends when it reaches a set potential. When cyclic voltammetry reaches a set potential, the working electrode's potential ramp is inverted. This inversion can happen multiple times during a single experiment. The current at the working electrode is plotted versus the applied voltage to give the cyclic voltammogram trace. Cyclic voltammetry is generally used to study the electrochemical properties of an analyte in solution. In this thesis, the cyclic voltammetry is used to characterize the electrochemical properties of supercapacitor. Ideal supercapacitor should exhibit square shape on a CV graph, while in reality, the CV shape of a supercapacitor is usually deviated from the square shapes due to the internal resistance (Figure 3.20). Also, the capacitance can be easily calculated from the current and the scan rate.

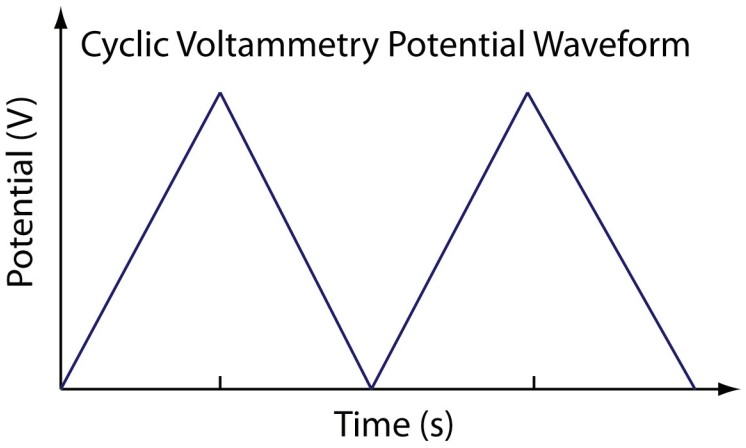

Figure 3.19 Pontential waveform for the cyclic voltammetry

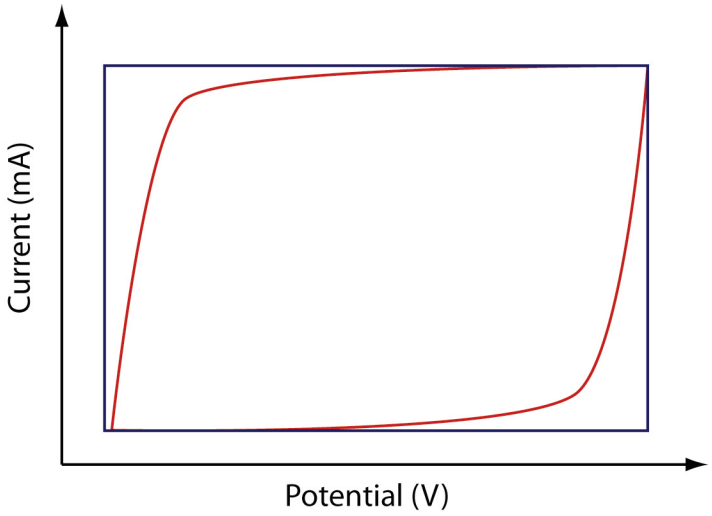

Figure 3.20 Cyclic Voltammetry graphs of ideal supercapacitor (blue) and deviated supercapacitor (red)

Galvanostatic charge discharge

This technique corresponds to supercapacitor or battery cycling under galvanostatic mode. The current is imposed but some potential limitations are possible for both charge and discharge. By applying a constant positive current, the supercapacitor or battery is charged, the potential is recorded until a limitation is reached. And the discharge tested is performed by apply a constant negative current. For the lithium ion battery, the charge/discharge profile is recorded as potential v.s. capacity. (Figure 3.21 a) The plateau part (stable potential over the discharge) on the curve is corresponding to the working potential of the batteries materials, which is related to the crystal phase change during the discharge. For the supercapacitor, the galvanostatic charge discharge is recorded as potential v.s. time. (Figure 3.21 b) The shape of the galvanostatic charge/discharge curve for the supercapacitor is usually composed of symmetric lines, of which the slope can be used to calculate the specific capacitance.

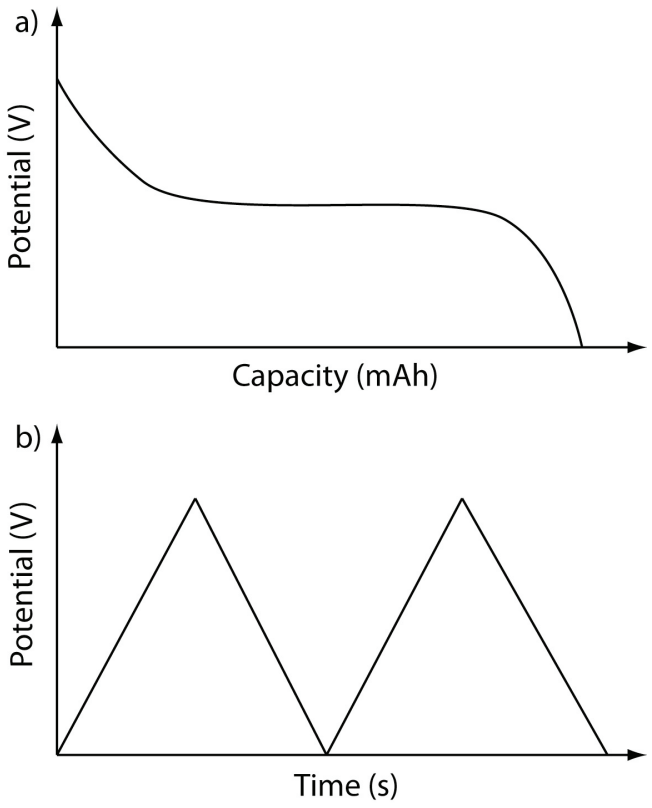

Figure 3.21 Glavanostatic charge/discharge curves for (a) lithium ion batteries and (b) supercapacitors

Chapter 4: Poly(3,4-ethylenedioxythiophene) nanotubes as electrode materials for high-powered supercapacitor

4.1 Introduction

As mentioned in Chapter 1, supercapacitors have received growing interests with the increasing need of high-powered energy storage devices for electrical vehicles and mobile electronic devices[209-211]. The supercapacitors work in conjunction with batteries to provide necessarily high peak power and enhance the life expectancy of the batteries. Based on the charge-storage mechanism, the supercapacitors are classified into (i) an electrochemical double-layer capacitor (EDLC)[8] that stores the energy non-faradaically by charging an electrochemical double layer at the interface between the porous electrode and the electrolyte, and (ii) a redox supercapacitor[212] that stores energy faradaically using the pseudocapacitance behaviour of a redox-active material. In recent times, studies have been focused on investigating the redox supercapacitors because they feature high energy densities (or specific capacitances).

Conductive polymers[7,213,214] and transition metal oxides[24,215] are promising materials for a redox supercapacitor because they can be readily converted between oxidized (doped) and reduced states (dedoped) by switching applied potentials. This conversion process involves diffusion of counter-ions into/out of conductive polymer or metal oxide films to keep their electroneutrality, which is a fundamental characteristic of a redox capacitor. Conductive polymers have been intensively investigated as electrode materials for supercapacitor because of their excellent electrochemical reversibilities, fast switching between redox states, high conductivity

in a doped state, mechanical flexibility, low toxicity, and low cost[216,217]. In particular, poly(3,4-ethylenedioxythiophene) (PEDOT) is a good candidate for the supercapacitor because of its high stability among other conductive polymers[218-222]. To date, most of the studies on PEDOT-based supercapacitors have been focused on enhancing their specific capacitances. For example, Lota et al.[220] achieved a high specific capacitance of ca. 150 F/g by using PEDOT/carbon nanotube composites. Li et al.[221] enhanced the specific capacitance of PEDOT from 72 to 100 F/g using sponge-like PEDOT structures synthesized under ultrasonic irradiation. Jang et al.[223] reported that high specific capacitance (155-170 F/g) of PEDOT was achieved by selective fabrication of PEDOT nanocapsules and mesocellular foams. Besides achieving high specific capacitance (high energy density), how to obtain high power from PEDOT as electrode materials for supercapacitor also needs immediate attention because more and more modern electronic devices require not only high energy but also high power.

In a redox supercapacitor, the high power can be achieved by enhancing the charge/discharge rate for the redox reaction. However, the conversion between redox states is governed by the mass transfer of counter ions[224]. The difficulty in keeping pace with fast charging/discharge process at high power demand will lead to inefficient utilization of the electrode material, i.e. a loss of usable energy. Similar problem exists in the lithium ion batteries: the slow diffusion of lithium ion in the solid phase of electrode materials limits its rate capability.[42,152,225-228] Using arrays of one dimensional hollow nanotubular structures have recently emerged as a solution achieving fast charge/discharge rate with their intrinsic structural characteristics. The

thin nature of the nanotube wall enables the rapid redox processes of electroactive materials such as conductive polymers and metal oxides by providing a short diffusion distance to the counter-ions. Furthermore, long nanotubes can provide high surface area and enough mass-loading for electrode materials to store sufficient energy. Martin's group, one of the pioneers in achieving fast charge/discharge rate of battery materials, has reported the enhanced charge transport rates in template-synthesized one-dimensional nanomaterials[125,229,230]. For example, they showed that higher lithium ion insertion rates could be achieved using the nanofibers of vanadium pentoxide[77,231], tin oxide[101,103] and $LiFePO_4$/carbon composite[76] and the nanotubes of $LiMn_2O_4$[107] and TiS_2[232]. Fast switching between coloured and decoluored states of PEDOT can be found in our recent development of a nanotube-based devices[226,227]. However, the application of PEDOT nanotubes as supercapacitor electrode materials has not been reported.

In this chapter, we investigate the supercapacitive properties of PEDOT nanotube arrays electrochemically synthesized in the cylindrical pores of an alumina template membrane. The micron-long, thin-walled nanotubular structures enable us to develop a supercapacitor exhibiting both a high power density and high energy density (or specific capacitance). Alumina membrane is used as the template to direct the growth of PEDOT nanotube owing to its advantages in tailoring the diameter and length of desirable nanomaterials. The PEDOT nanostructures were synthesized by an electrochemical method rather than chemical one to provide higher conductivity[125,222]. Cyclic voltammetry was used to characterize specific capacitance and rate capability of PEDOT-nanotube-based electrode. The energy densities and power densities were

evaluated by galvanostatic charge/discharge cycling for the supercapacitor with two symmetric PEDOT-nanotube-based electrodes. All the electrochemical tests on the nanotube array were performed without removing the template, which offers the following advantages: First, the alumina template can directly serve as a substrate to support the electrode materials; Second, the alumina template can be used as a separator between the electrodes, and the porous channels can store the electrolyte; Third, the electrode materials are well protected inside the alumina pores to prevent the nanostructure aggregation and electrode surface damage. Finally impedance spectroscopy was used to investigate the diffusion resistance of the PEDOT nanotubes.

4.2 Experimental Section

4.2.1 Chemicals and Materials

3,4-Ethylenedioxythiopene (EDOT), lithium perchlorate and anhydrous propylene carbonate were purchased from Sigma Aldrich (Milwaukee, WI). Tetraethylammonium tetrafluoroborate (Et_4NBF_4) (electrochemical grade) was obtained from Fluke. Acetonitrile was obtained from Fisher Scientific (Fair Lawn, NJ). Gold plating solution (Orotemp 24) was from Technic (Cranston, RI). De-ionized water (ca. 18 $M\Omega \cdot cm^{-1}$ in resistivity) was made by a Milli-Q water purification system (Millipore; Dubuque, IA). Alumina membranes of 200 nm in pore diameter and 60 μm in thickness are commercially available from Whatman (Clifton, NJ).

4.2.2 Synthesis

PEDOT nanotubes were synthesized potentiostatically at 1.6 V in an acetonitrile solution of 20 mM EDOT, while PEDOT nanowires were done at 1.4 V in 100 mM EDOT. All electrode potentials were measured relative to an Ag/AgCl reference electrode using a Pt foil as a counter electrode, if not specified otherwise. The preparation of a working electrode is as follows. A thin layer of gold (ca. 500 nm) was sputtered onto the branched side of an alumina membrane by using a sputtering system (Denton Vacuum Desktop III). The Au-coated membrane was connected to an electrical circuit using a copper tape (3M). An electroactive window (0.32 cm^2 in nominal area) was defined using Parafilm. Considered the porosity of a membrane (60 %), the corrected surface area of the electroactive window was 0.2 cm^2. For the synthesis of PEDOT nanowires, flat-top electrodes at the bottom of the pores were prepared by further electrodepositing gold galvanostatically at 1.0 mA/cm^2 for 15 min in gold plating solution. The mass of the resulting PEDOT nanostructures was controlled by fixing the total charges passed during the electropolymerization.

4.2.3 Characterizations

The PEDOT nanostructures were investigated using a field-emission scanning electron microscope (SEM; Hitachi S-4700, operated at an acceleration voltage of 5 keV) and transmission electron microscope (TEM; Zeiss EM10CA, operated at 80 keV). The sampling methods for SEM and TEM analysis were described in detail previously[226,227]. Briefly, the gold-coated side of a small piece of an alumina template was tightly attached onto an SEM specimen holder by using a carbon tape. The template was dissolved in 3 M NaOH to expose the nanomaterials. After rinsing them

with de-ionized water repeatedly, the samples were dried in air before observation. For TEM sampling, the gold layer was removed by using an aqua regia solution after growing desired nanostructures in a gold coated alumina template. The alumina template was dissolved in 3 M NaOH. The released nanomaterials were repeatedly rinsed with de-ionized water and ethanol. Then, 6 μL of the nanomaterial solution was dropped and dried on a TEM grid.

Cyclic voltammetry was performed in a potential range between 0 and 1.2 V at various scan rates of 10–1000 mV/s in 1 M $LiClO_4$ using the three-electrode system. Type I supercapacitor was built with two PEDOT-nanotube-based electrodes into an electrochemical cell and proper amount of electrolyte (1 M Et_4NBF_4 in propylene carbonate) in between. Galvanostatic charge/discharge curves for the Type I supercapacitor were obtained by cycling potential from 0 to 1.2. All the above electrochemical experiments were performed using a bi-potentiostat (BI-STAT; Princeton Applied Research). The impedance measurement was carried out using a potentiostat (CHI 660A) at 0 V (v.s. Ag/AgCl) with a perturbation amplitude of 5 mV over a frequency range 0.01–10^4 Hz.

4.3 Results and Discussion

4.3.1 Structure characterization and basic growth mechanism

Controlling the total charge during electropolymerization well regulates the amount of PEDOT loaded in the pores of the template. By depositing PEDOT with a charge density of 500 mC/cm^2, we obtained the mass loading of around 0.3 mg/cm^2. PEDOT can be electrodeposited up to 3 C/cm^2 (PEDOT starts to grow out of the membrane around 3 C/cm^2), which gives us 1.8 mg/cm^2 mass loading. By stacking the alumina

membranes, higher mass loading can be achieved. The total-charge dependence of PEDOT nanostructures is complicated because not only length but also the wall thickness of nanotubes is affected by total charge. The previous mechanism study showed that nanotubes grow at high overpotentials (>1.4 V) at low monomer concentrations (<50 mM).

The SEM images of PEDOT nanotubes (data not shown) have a similar appearance as before: highly collapsed and aggregated structures (data not shown)[152], which are caused by the intensive aggregation of nanostructures at their tops driven by the strong surface tension generated at the interface between the nanotubes and solvent during the solvent evaporation[173]. These structural defects can affect the charge/discharge performance of nanostructured electrode materials due to hindered diffusion of counter ions. However, such structural defects of nanostructures can be avoided in this study since our electrochemical tests were performed under the support of a rigid template.

We investigated detailed nanostructures as a function of charge density to understand the capacitive properties. Figure 4.1 shows the TEM images of PEDOT nanotubes synthesized in 20 mM EDOT at 1.6 V for a total charge density of 200, 300 and 500 mC/cm^2, which correspond to 40±5, 60±5 and 110±5 s in the electropolymerization time, respectively. Nanotubes with thin, uniform, and smooth wall were grown along the template pore at the beginning (Figure 4.1a). As the total charge was increased further, the nanotube length increased in proportion while the wall thickness and porosity changed in a complicated way. For example, we obtained nanotubes with gradually-thinning walls along the nanotubes' axis rather than ones

with uniform wall thickness at the total charge density of 300 mC/cm^2 (Figure 4.1b). This can be attributed to the gradually-decreasing monomer supply at the tips of the nanotubes during their growth, resulting from fast monomer depletion when the PEDOT is electropolymerized at lower monomer concentration and higher overpotential. Under the same conditions, we found the upper part of the nanotubes became more porous with increased charge density (Figure 4.1). This porous, loose structure at higher oxidative overpotentials was also observed in a film by Fröberg and co-workers[233]. The limited monomer supply also elucidated why the bottom of the nanotubes was porous (distinct from the solid nanowires) even though they were filled at the high charge density of 500 mC/cm^2 (Figure 4.1e).

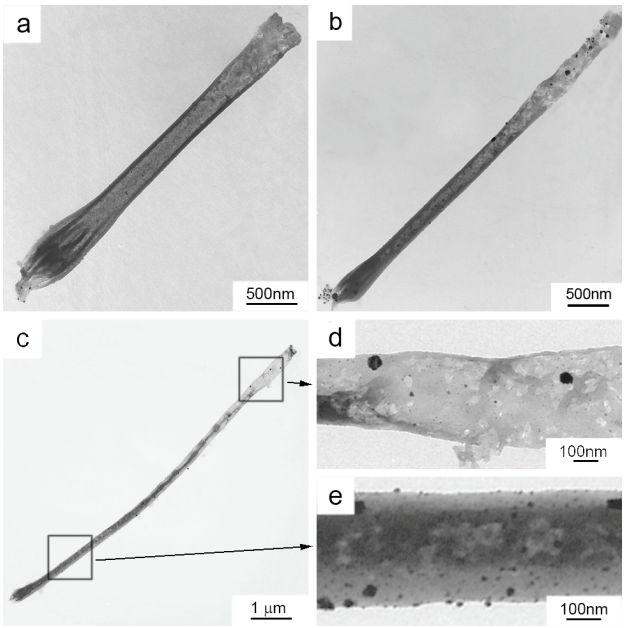

Figure 4.1. TEM images of PEDOT nanotubes synthesized in 20 mM EDOT at 1.6 V with the charge density of (a) 200, (b) 300 and (c) 500 mC/cm^2. Figures (d) and (e) are the magnified images to show the detailed nanostructure.

4.3.2 Electrochemical Characterizations

The electrochemical performances were tested for the PEDOT nanotubes electropolymerized at the various total charge densities of 100, 200, 300, 400, and 500 mC/cm^2. Best electrochemical performances for fast switching between redox states were obtained from the nanotubes with lowest total charge density (100 mC/cm^2) because of the facile electrochemistry caused by their thin wall structures. However, the mass loading at the lowest charge density was too limited to provide high mass loading, which is required to achieve high capacitance. Therefore, electrochemical experiments were performed at the charge density of 500 mC/cm^2 if not specified otherwise. For notational convenience, we call nanotubes with total charge density of 500 mC/cm^2 "NT 500" and do likewise for other charge densities.

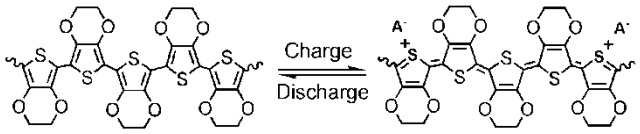

Scheme 4.1. Molecular structures of oxidized and reduced forms of PEDOT. A^- represents counter anion (here, ClO_4^-)

Cyclic voltammetry was used to characterize the capacitive properties of the PEDOT nanostructures. The pseudocapacitance behaviour of PEDOT is originated from diffusion of charged counter ions (here, ClO_4^-) during the redox processes, as shown in Scheme 4.1. All cyclic voltammetric scans were performed in a potential range from 0 to 1.2 V, within which high conductivity and good electrochemical reversibility of PEDOT can be maintained[234]. Figure 4.2a shows the cyclic voltammograms of NT 500 at different scan rates of 50, 100, 250, 500 and 1000 mV/s. The shape of CV of PEDOT nanotubes closely resembles a rectangle even at

the high scan rate of 1000 mV/s, showing its ideal capacitor behavior. Furthermore, the resulting anodic current in nanotubes increases in proportion to the scan rate, as shown in Figure 4.2b. This helps to achieve a constant specific capacitance, which is independent of the scan rate, as expected by the following equation:

$$C_{spec} = \frac{i}{m_e \frac{\Delta V}{\Delta t}} , \tag{4.1}$$

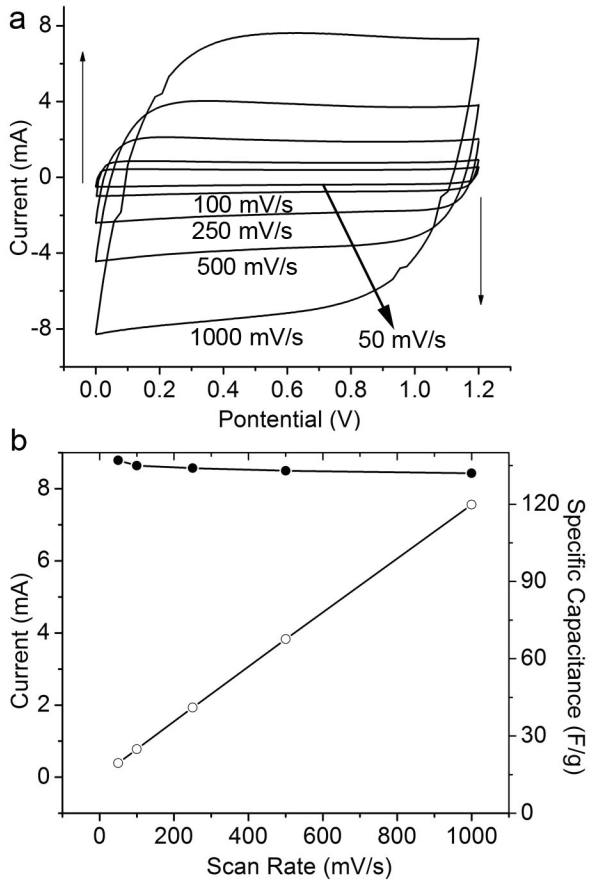

Figure 4.2. (a) Cyclic voltammograms of NT 500 at different scan rates of 50, 100, 250, 500 and 1000 mV/s in a potential range between 0 and 1.2 V. The arrow points the direction of scan rate increase. (b) Plots of the average anodic current (open circle) and specific capacitance (closed circle) v.s. scan rate.

where, C_{spec} is the specific capacitance in F/g, i is the charge/discharge current in mA, m_e is the weight of the one electrode material (PEDOT weight) in mg, and $\Delta V/\Delta t$ is the scan rate in V/s. The specific capacitance for NT 500 is approximately 140 F/g, calculated using the current of ca. 0.8 mA from the CV in Figure 4.2b, m_e of 5.72×10^{-2} mg and scan rate of 100 mV/s. This value is satisfactory and comparable to previous works mentioned earlier in this chapter[220,221]. Compared to the theoretical maximum specific capacitance of PEDOT (ca. 200 F/g), which is determined by the molecular weight of polymer (142 g per mol) and the doping level of counter ions (0.3)[235], the specific capacitance here is around its 70%.

Conductive-polymer-based supercapacitors can be classified into three types[213]. Type I is a symmetric system using p-dopable conductive polymer as each electrode of the capacitor. Type II is an asymmetric system based on two different p-dopable conducting polymers. Type III: a symmetric system based on a conducting polymer which can be both p- and n-doped[236]. Due to the difficulties of n-doping for PEDOT. in this chapter we attempt to build Type I supercapacitor using two identical electrodes with PEDOT nanotubes. Galvanostatic charge/discharge cycles were performed to evaluate the power density and energy density of PEDOT nanotube based supercapacitors. Here, only the weight of electroactive polymers is taken into account. Figure 4.3 shows the galvanostatic charge/discharge curves of PEDOT nanotube based supercapacitors at the current density of 5 mA/cm^2. As expected, the galvanostatic measurements agreed well with the CV studies: the nanotubes produced linear and symmetrical curves, and the specific capacitances of PEDOT nanotube based supercapacitors from Figure 4.3 are 132 F/g. This high linearity and symmetry

in the galvanostatic charge/discharge curve of a nanotube-based supercapacitor indicate high charge/discharge efficiency (η) of 99.5%, which is the ratio of discharge time t_d and charge time t_c. The slower potential change rate, $\Delta V/\Delta t$, indicates higher specific capacitance according to Eq. 4.1. Figure 4.4 shows the summarized specific capacitances of supercapacitors made of nanotubes which synthesized at the various electropolymerization charges (100, 200, 300, 400, 500, 1000, 2000 and 3000 mC/cm^2). The specific capacitance for nanotubes decreased less than 20 % when the electropolymerization charge density was increased from 100 to 3000 mC/cm^2. This small decrease in the specific capacitance at the high electropolymerization charge indicates that the conductive polymers are effectively charged and discharged independent of nanotube lengths.

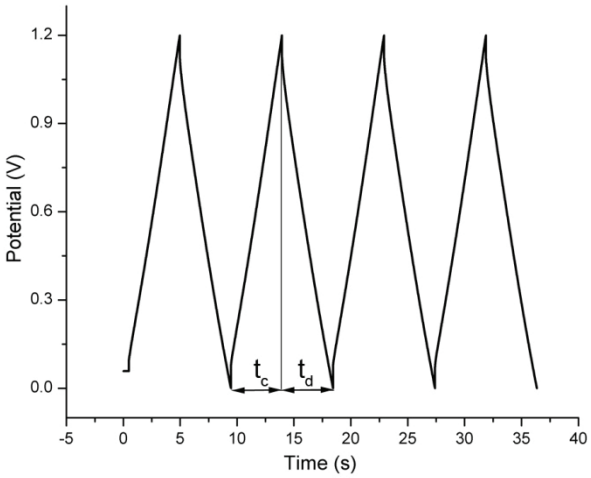

Figure 4.3. Galvanostatic charge/discharge curves of supercapacitors made of NT 500. Potentials were cycled from 0 to 1.2 V at a current density of 5 mA/cm^2 in an acetonitrile solution of 1 M $LiClO_4$. Here t_c and t_d represent charge and discharge time respectively.

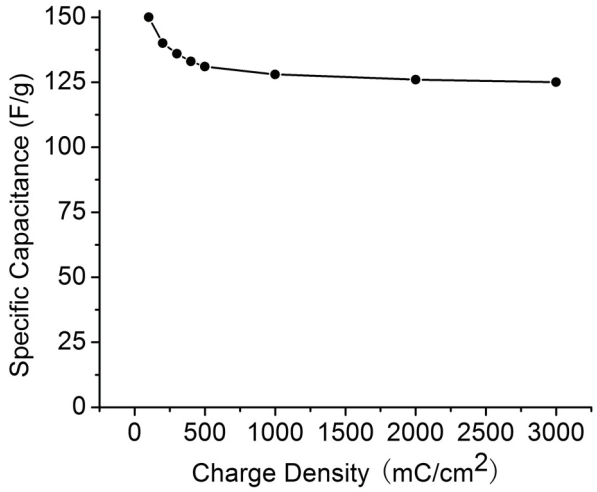

Figure 4.4. Specific capacitances of Type I supercapacitor based on PEDOT nanotubes synthesized at various total charge densities (100, 200, 300, 400, 500, 1000, 2000 and 3000 mC/cm^2).

As in a conventional battery, the maximum power (P_{max}) that can be delivered by a supercapacitor is given by

$$P_{max} = \frac{V^2}{4R}, \tag{4.2}$$

where V is the potential range for the charge/discharge cycling in V and R is the equivalent series resistance (ESR) in Ohm. In order to maximize the deliverable power, many efforts have been made to minimize the ESR[237-239]. Practically, however, high power requires fast charge/discharge rate and is always accompanied by the loss of usable energy especially in a redox supercapacitor because of the incomplete utilization of redox-active materials. Thus, the efficient use of the materials is an important issue to achieve the optimal high power density while maintaining the high energy density.

The energy density (E_d in Wh/kg) of a symmetric supercapacitor at a constant current is expressed as

$$E_d = \frac{i\int V dt}{m_{total}}, \tag{4.3}$$

where m_{total} is the total mass of two electrode materials (2 m_e). When the voltage varies linearly from 0 to V_{max} over time, in Type I supercapacitor, Equation 4.3 becomes

$$E_d = \frac{1}{8} C_{spec} V_{\max}^2 . \tag{4.4}$$

This is also used in calculating energy density[240].

Power density (P_d in kW/kg) can be calculated as

$$P_d = \frac{E_d}{t_d} \tag{4.5}$$

The experimental values for P_d and E_d were obtained by analyzing the charge/discharge curve of PEDOT nanostructures at various current densities. Figure 4.5 shows the plot of E_d *vs* P_d, known as Ragone plot, for Type I supercapacitor made of NT 500. Nanotube-based-supercapacitor can maintain their energy densities (5.6 Wh/kg) and specific capacitance (120 F/g) at least 80% even when the power density increases from 5 to 25 kW/kg. The power density (specific power) obtained by this PEDOT-nanotube-based supercapacitor is higher than previously reported PEDOT and other conductive polymer film based supercapacitors[241-252]. Some of these reports demonstrated that energy densities lost dramatically when the power density is boosted less than 10 kW/kg. Therefore, nanotubular structure is an excellent candidate to provide high power density with less loss of energy density as a

supercapacitor. The energy density of this system is comparable the work that uses similar Type I or even Type III supercapacitors design. However, based on equation 4.4, higher energy density can be obtained using different conductive polymers that has high specific capacitance. Also, designing supercapacitor with higher voltage range can help to achieve higher energy density according to Equation 4.4. One approach is to build Type III supercapacitor because additional voltage range can be obtained from the n-doping region. Another solution is to build a hybrid-type supercapacitor, i.e. find a suitable material such as activated carbon that can store electrochemical energy under negative potentials as the counter electrode to the conductive polymer.

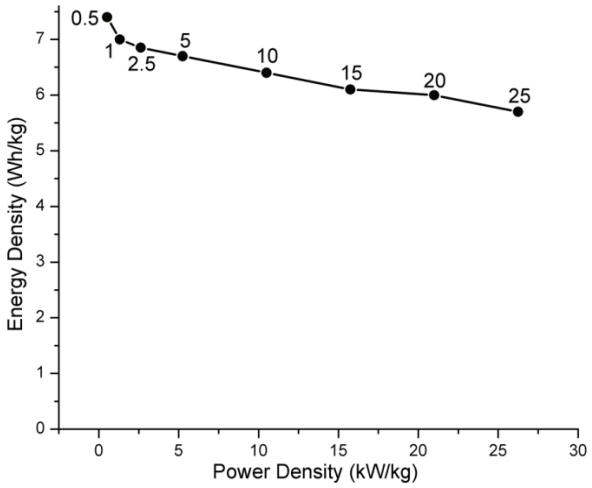

Figure 4.5 The plot of energy density versus power density (Ragone plot) for Type I supercapacitor made of NT 500. The inserted numbers represent the current densities (mA/cm^2) for the charge/discharge.

4.3.3 Mechanism of fast charge/discharge behavior in nanotubes.

The charge/discharge process of a PEDOT-based supercapacitor is different from that of EDLC: the PEDOT-based supercapacitor uses the redox reaction of PEDOT while the EDLC utilizes the electrostatic charges built on the electrode surface. PEDOT-based supercapacitors requires the diffusion of counter-ions in/out the polymer (doping and dedoping of conductive polymer) to balance charges generated during the redox reaction. The criterion for a PEDOT-based supercapacitor to exhibit ideal capacitor behaviours is that the doping/dedoping rates should be fast enough to provide constant current during the redox reaction. This doping/dedoping process involves not only the charge (electrons or holes) transport but also the ion transport. Here, the ion transport rate determines the charge/discharge rate of PEDOT because it is slow compared to charge transport. The ion transport rate, limited by the diffusion of counter-ions, is highly influenced by the thickness of the polymer layer. The thinner film has a lower resistance to counter-ion diffusion due to its shortened diffusion distance. Therefore, thinner film can charge/discharge counter-ions more efficiently at a given current. In other words, the voltage change rate ($\Delta V/\Delta t$) in a thin film is smaller than in thick one to provide constant current. This leads to a higher specific capacitance in the thin film as shown in Equation 4.1.

Now, if we take a close look at one single nanotube out of the nanotube array, as illustrated in Scheme 4.2, hollow nature of the nanotube allows the electrolyte ions to penetrate into the polymer and access internal polymer surface easily. Because the thickness of nanotube wall can be approximated to the film thickness, it is natural that NT 100 and NT 200 can have highest specific capacitance values (Figure 4.4). It is also notable that the specific capacitance change as a function of charge density (up to

500 mC/cm^2) is not significant in nanotubular structure (Figure 4.4). This can be well understood by taking into account the structure of NT 500, which still has thin walls at the top and the porous structures at the bottom (Figure 4.1d and 4.1e and Scheme 4.2).

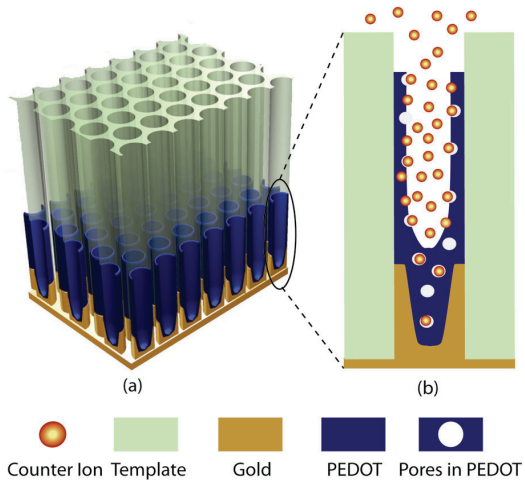

Scheme 4.2. (a) Electrode made of PEDOT nanotubes in a porous alumina template for a supercapacitor. (b) Schematic of ion transport (doping or charging) in a single nanotube. Complete and fast doping of anions can be achieved in the PEDOT nanotubes because of their short diffusion distance and high porosity.

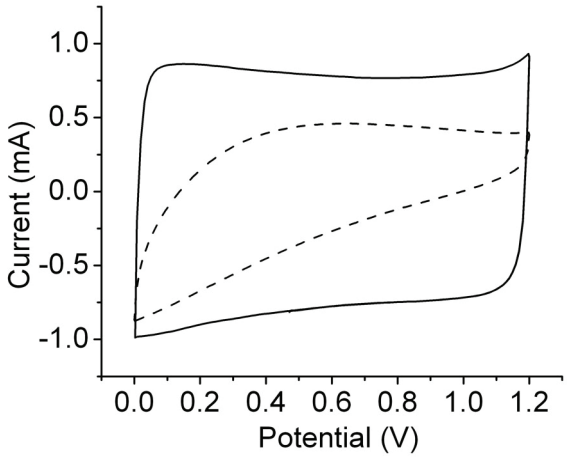

Figure 4.6. Cyclic voltammograms of solid nanowires (charge density 500 mC/cm^2) shielded (dashed line) and unshielded (solid line) by an alumina template at the scan rate of 100 mV/s in a potential range between 0 and 1.2 V.

In order to prove the mechanism of fast charge/discharge of the nanotubes, we studied the electrochemical properties of solid nanowires protected by the alumina template. Solid nanowires were grown on the gold flat-top electrode at 1.4 V in 100 mM EDOT solution. The charge density of solid nanowires was controlled to be the same as in the NT 500. Here we note them as NW 500. Figure 4.6 shows that solid nanowires shielded by alumina template have much less capacitive current compared to the NT 500 at the same scan rate (Figure 4.2). The specific capacitance estimated based on average current density is only 50 F/g. In addition, it has significantly distorted rectangular shape that corresponds to the deviated potential-dependent capacitive behaviour (non-ideal capacitive behaviour). This can be explained as follows: First, nanowires have denser and more rigid structure (higher diffusional resistance) than hollow nanotubes. Second, the side wall of the nanowires is completely shielded by a template so that the diffusion of counter-ions is only allowed from the tops of the nanowires. Here, the diffusion length of counter-ions is corresponding to the lengths of nanowires (equivalent to the thickness of dense bulk film). Thus, the counter-ion transport in the dense and long nanowires is very sluggish, and only some part of the nanowire is involved in the charge/discharge process at the high scan rate or current. After template removal, however, the capacitive current increased significantly and are comparable to that of the nanotubes (Figure 4.2 and 4.6). In addition, the rectangle-like shape also indicated better

capacitive properties. This is because the cylindrical side of the nanowires can be accessed by the electrolyte after the template has been removed. However, after template removal, the exposed nanostructures are subject to be lost and damaged mechanically without the template protection. The thin conductive substrate (sputtered metal) may easily crack after wetting and drying, which will affect the electrochemical performance. The above facts indicate that the nanotubes indeed take the advantage of their internal surface to allow the ions transport owing to the unique hollow nature.

4.3.4 Electrochemical AC Impedance Spectroscopy.

To support our explanation, we used AC impedance spectroscopy, which is an essential tool to study the ion transport occurring during doping/dedoping process. Figure 4.7 shows the impedance plots of PEDOT nanostructures recorded using perturbation amplitude of 5 mV in a frequency range from 10^4 to 0.01 Hz at the applied voltage of 0 V v.s. Ag/AgCl. Our electrochemical system has finite nanostructured electrodes in template pores and can be described by using the 'classical' finite-length transmission line model developed by Macdonald[253]. The useful electrochemical information can be extracted from the impedance plot in Figure 4.7 by considering the limiting behaviour at high and low frequencies. At the high frequency region, it is hard to observe a well-defined semi-circle. This indicates that charge transfer resistance is small, and our electrochemical system is kinetically fast. Thus, charges (electrons) can be readily transferred into the highly-conductive PEDOT solid phase. This favorable charge transfer between the PEDOT and electrode surface is natural because the PEDOT was grown electrochemically in good

contact with the base electrode. The *x*-intercepts provide quantitative information on effective internal resistances, R_s, mostly contributed by the uncompensated solution resistance. Since we used the same electrolyte solution, the R_s values for NT 500 and NW 500 systems are very close (18 and 17 Ω, respectively).

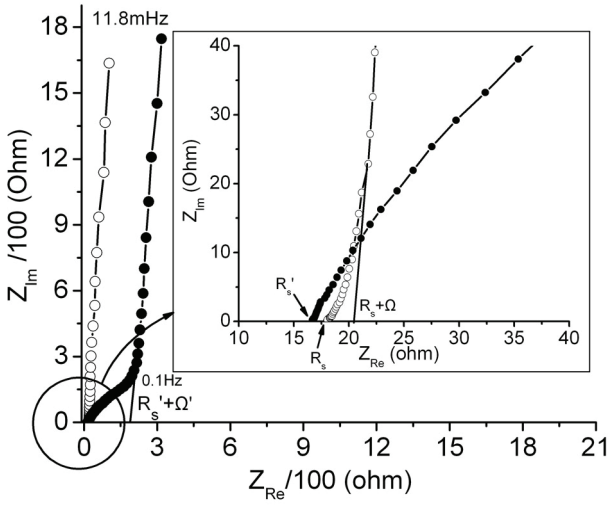

Figure 4.7 Impedance plot of NT 500 (open circle) and NW 500 (closed circle) in a frequency range between 0.01 and 10^4 Hz. The x-intercepts (Rs and Rs') in the inset represent the solution resistance, while Ω and Ω' represent one-third of the ionic resistance caused by the diffusion.

At the low frequency region, we can obtain information on the ion transport: the extrapolation for the low-frequency data gives another *x*-intercept equal to R_s + Ω, where Ω represents one third of ionic resistances in the pores for the distributed RC network of the nanoelectrode in the pore[254]. Thus-obtained resistance values for nanotubes and nanowires are 6 and 170 Ω, respectively. Almost pure capacitive behaviour in nanotubes is manifested by this low internal resistance. The abnormally large ionic resistance in nanowires is related to the slow ion diffusion into the dense, rigid nanowires. The knee frequency for the nanowires, at which they start to behave

like a capacitor, is ca. 0.1 Hz. This suggests that nanowires in the template are not suitable for a high-power supercapacitor which requires fast charge/discharge response.

From the impedance curve (Figure 4.7), the specific capacitances of the nanotubes and nanowires can be calculated by

$$C_{spec} = \frac{1}{2\pi f m_e Z_{\mathrm{Im}}}, \tag{6}$$

where f and Z_{Im} are the frequency in Hz and the imaginary part of impedance in ohm, respectively. The calculated specific capacitances for NT 500 and NW 500 at low frequency (11.8 mHz) are 144 and 133 F/g, respectively. The C_{spec} value for NT 500 is in good agreement with that from the galvanostatic study (132 F/g in Figure 4.3). On the other hand, the C_{spec} for NW 500 is much higher than the value (50 F/g) in Figure 4.6. This means that NW 500 can be operated with almost full use of its capacitance at low frequency. As the frequency is increased to 1 Hz, the calculated C_{spec} of NT 500 is kept as high as 126 F/g, while the C_{spec} of NW 500 dropped dramatically to 30 F/g. At the much higher frequency of 1000 Hz, both nanotubes and nanowires suffer from insufficient counter-ion diffusion, and the calculated C_{spec} values for NT 500 and NW 500 dropped significantly to 26 and 6 F/g, respectively.

4.4 Conclusion

We have demonstrated that nanotubular structures could dramatically improve the electrochemical performance in a PEDOT-based supercapacitor. The thin-walled nanotubes provided short diffusion paths and low ionic resistance for the diffusion of counter-ions to make all PEDOT available during complete charge/discharge even at

a fast scan rate. This fast electrochemical reaction enables us to achieve high power density without much loss of energy density (specific capacitance), which is the basic requirement for the supercapacitor to meet the demand of modern instruments on high peak power. The electrochemical performance of nanotube-based supercapacitors can be further improved by the optimizing electrolytes, electrode materials, and cell design. This study will also provide the fundamental understanding for the high performance in other nanotubes-based organic electronic devices which require fast charge/discharge processes such as batteries, electrochromic displays, sensors, and actuators.

Chapter 5: Synthesis and Characterization of RuO_2/poly (3,4-ethylenedioxythiophene) (PEDOT) Composite Nanotubes for Supercapacitors

5.1 Introduction

In our previous chapter, we have successfully demonstrated high-power poly(3,4-ethylenedioxythiophene) (PEDOT) nanotubes as electrode materials for a high-power supercapacitor. The thin-walled nanotubes provided short diffusion paths and low ionic resistance for the diffusion of counter-ions to make the entire PEDOT available during the complete charge/discharge even at a fast scan rate. However, the energy density of a supercapacitor composed of the PEDOT nanotubes is restricted by the moderate specific capacitance of PEDOT (140 F/g), which is an intrinsic property of the PEDOT itself[218-221,255]. Combining PEDOT with materials that have high specific capacitance has been used to address this problem. For example, in our recent paper, we have successfully improved the specific capacitance up to 210 F/g by fabricating the composite MnO_2/PEDOT coaxial nanowires using one step electrochemical deposition[109]. The core MnO_2 provides high energy storage capacity while the highly conductive, porous, and flexible PEDOT shell facilitates the electron transport and ion diffusion into the core MnO_2 and protects it from significant collapsing and breaking. These combined properties enable the coaxial nanowires to have high specific capacitances at high power. In another example, Zang et al reported sputtering RuO_2 thin layer onto the polypyrrole nanocones to form nanostructured polypyrrole/RuO_2 composite, which has achieved enhanced specific capacitance up to 302 F/g[256].

In this chapter, we will report the step-wise template synthesis of RuO_2/PEDOT nanotubes, which can further enhance the specific capacitance of PEDOT nanotubes to 640 F/g brought by high specific capacitance of RuO_2 (1217 F/g), while maintaining the high power (20 kW/kg) featured by the nanotubular structures. Thus obtained specific capacitance is higher than the specific capacitance obtained by the PEDOT/RuO_2 films (420 F/g)[257] benefited from the high surface area brought by the nanotubular structures as well as the fast ion diffusions from the thin walls of nanotubes. In this study, an alumina template is used to direct the growth of PEDOT nanotubes by electropolymerization, and then the RuO_2 is electrodeposited into the porous network of the PEDOT nanotubes to form composite RuO_2/PEDOT nanotubes. The deposited RuO_2 utilizes the free void spaces available in the PEDOT nanotubes, and due to the high specific surface area from the nanotubular structure, the RuO_2 exhibited high specific capacitance of (1217 F/g), which is higher than that of RuO_2 (930 F/g) in the bulk RuO_2/PEDOT film[257]. Microscopic characterizations reveal that the PEDOT nanotubes indeed serve as the template to direct the growth of RuO_2 onto their rough porous internal surface. Furthermore these flexible PEDOT nanotubes can prevent the RuO_2 nanostructures from breaking and detaching from current collector after template removal. At the same time, the more rigid RuO_2 helps the PEDOT nanotubes to maintain their nanotubular shapes by keeping them from collapsing. Cyclic voltammetry was used to qualitatively analyze the capacitive properties of the composite RuO_2/PEDOT nanotube based electrode. The specific capacitance, energy density and power density was evaluated by galvanostatic charge/discharge cycling of the supercapacitor.

5.2 Experimental Details

5.2.1 Chemicals and Materials

3,4-Ethylenedioxythiopene (EDOT), lithium perchlorate, ruthenium (III) chloride and sulfuric acid were purchased from Sigma Aldrich (Milwaukee, WI). Acetonitrile was obtained from Fisher Scientific (Fair Lawn, NJ). De-ionized water (ca. 18 $M\Omega \cdot cm^{-1}$ in resistivity) was made by a Milli-Q water purification system (Millipore; Dubuque, IA). Alumina membranes of 200 nm in pore diameter and 60 μm in thickness are commercially available from Whatman (Clifton, NJ).

5.2.2 Synthesis

PEDOT nanotubes were grown in the alumina template potentiostatically at 1.6 V in an acetonitrile solution of 20 mM EDOT until the charge reached 60 mC. electrode potentials were measured relative to an Ag/AgCl reference electrode using a Pt foil as a counter electrode, if not specified otherwise. The preparation of a working electrode is as follows. A thin layer of platinum (ca. 250 nm) was sputtered onto the branched side of an alumina membrane by using a sputtering system (Denton Vacuum Desktop III). The Pt-coated membrane was connected to an electrical circuit using a copper tape (3M). An electroactive window (0.32 cm^2 in nominal area) was defined using silicone rubber. Considering the porosity of a membrane (60 %), the corrected surface area of the electroactive window was 0.2 cm^2. The PEDOT nanotube electrode was then immersed in 20 mM $RuCl_3$. RuO_2 was then electrodeposited by cyclic voltammetry (CV) scanned from -0.2 V to 1.0 V at the scan rate of 50 mV/s[258] while maintaining the temperature at 50 ˚C using a VWR heated/refrigerated circulator 1140S. The amount of electrodeposited RuO_2 can be controlled by the number of CV

cycles. RuO_2 nanowires were synthesized using similar method directly on the Pt bottom electrodes while not on the PEDOT nanotubes.

5.2.3 Characterizations

The PEDOT, RuO_2, and RuO_2/PEDOT nanostructures were investigated using a field-emission scanning electron microscope (SEM; Hitachi S-4700, operated at an acceleration voltage of 5 keV) and transmission electron microscope (TEM; Zeiss EM10CA, operated at 80 keV). The sampling methods for SEM and TEM analysis were described in detail previously[259]. Briefly, the Pt-coated side of a small piece of an alumina template was tightly attached onto an SEM specimen holder by using a carbon tape. The template was dissolved in 3 M NaOH to expose the nanomaterials. After rinsing them with de-ionized water repeatedly, the samples were dried in air before observation. For TEM sampling, the sample was soaked in 3M NaOH to remove the alumina template and then followed by carefully and repeatedly rinsed with de-ionized water. Finally the sonication is applied to disperse these nanomaterials in ethanol. Then, 6 μL of the nanomaterial solution was dropped and dried on a TEM grid.

Cyclic voltammetry was performed in a potential range between 0 and 1 V at a scan rate of 50 mV/s in 1 M sulfuric acid using the three-electrode system. Galvanostatic charge/discharge curves were obtained by cycling the potential from 0 to 1 V at different current densities of 5-25 mA/cm^2 in the same electrolyte. All the above electrochemical experiments were performed using a bi-potentiostat (BI-STAT; Princeton Applied Research).

5.3 Results and Discussion

5.3.1 Growth Scheme and Structure characterizations

The synthesis of RuO_2/PEDOT can be illustrated in Scheme 5.1. First, the PEDOT nanotubes are grown on the ring-shaped bottom electrodes at high over potential (>1.4 V) under low EDOT concentration (<50 mM) based on our previous proposed mechanism: the bottom ring-shaped electrode defines the tubular shapes due to limited diffusion of monomer with low concentration preventing the formation of solid nanowires. Controlling the amount of charge per unit area during electropolymerization regulates the amount of PEDOT loaded in the pores of the template well. In this work, we electrodeposited 300 mC/cm^2 PEDOT, which corresponds to 0.18 mg/cm^2 mass loading. The hollow PEDOT nanotubes allow easy access of $RuCl_3$ (20 mM) solution into their voids so that the hydrous RuO_2 can be further electrodeposited onto the rough internal surfaces of PEDOT nanotubes as well as into the porous walls of PEDOT nanotubes using cyclic voltammetry method that cycled between -0.2 V to 1V at 50 ˚C. The detailed growth process of RuO_2 can be found elsewhere[258]. Figure 5.1 shows the cyclic voltammogram of RuO_2 growth on PEDOT nanotubes by first 40 cycles. As the cycle number increases, both anodic and catholic current increase, which corresponds to the continuous growth of RuO_2. Therefore the loading amount of RuO_2 can be controlled by the cycle numbers. In the rest of this chapter, the term PEDOT nanotubes refers to PEDOT nanotubes that are electrodeposited by the charge density of 300 mC/cm^2, and the term RuO_2/PEDOT composite nanotubes refers to the same PEDOT nanotubes but with further electrodeposition of RuO_2 by 60 CV cycles. The 60 cycle number is the optimum

number for the deposition of RuO_2 in the hollow PEDOT nanotubes to utilize their free void spaces while not filling up the nanotubes completely.

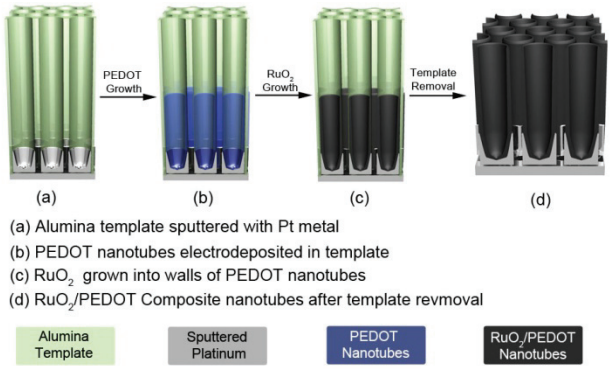

Scheme 5.1. Step-wise electrodeposition of RuO_2/PEDOT composite nanotubes in alumina template

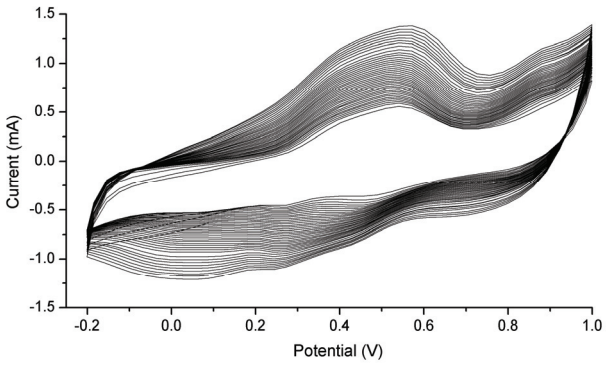

Figure 5.1. Cyclic voltammetry growth of RuO_2 into PEDOT nanotubes between -0.2 V and 1.0 V at the scan rate of 50 mV/s in 20 mM $RuCl_3$ solution at 50 ˚C.

Figure 5.2a shows the SEM image of typical PEDOT nanotubes after template removal, which have a similar appearance as before: highly collapsed and aggregated structures, which are caused by the intensive aggregation of nanostructures at their tops driven by the strong surface tension generated at the interface between the nanotubes and solvent during the solvent evaporation. As we can see, the top part of the each PEDOT nanotube is collapsed into belt shape and does not show any open

pore end. These structural defects can negatively affect the charge/discharge performance of nanostructured electrode materials due to hindered diffusion of counter ions. Figure 5.2b shows the SEM image of RuO_2 nanorods after template removal. Due to the brittle nature of metal oxide, these RuO_2 nanorods are found to be broken either at their bottoms or in the middle. Figure 5.2c shows the SEM image of RuO_2/PEDOT composite nanotubes. Some open entrances can be clearly found at the top of these composite nanotubes. Compared to the closed tips of PEDOT nanotubes shown in Figure 5.2a, we can see that the inclusion of rigid RuO_2 helps keep the soft PEDOT nanotubes from collapsing into the belt shapes effectively. On the other hands, much less breakage is found for the composite nanotubes compared to the Figure 5.2b, which is offered by the added flexibility of PEDOT to the rigid RuO_2.

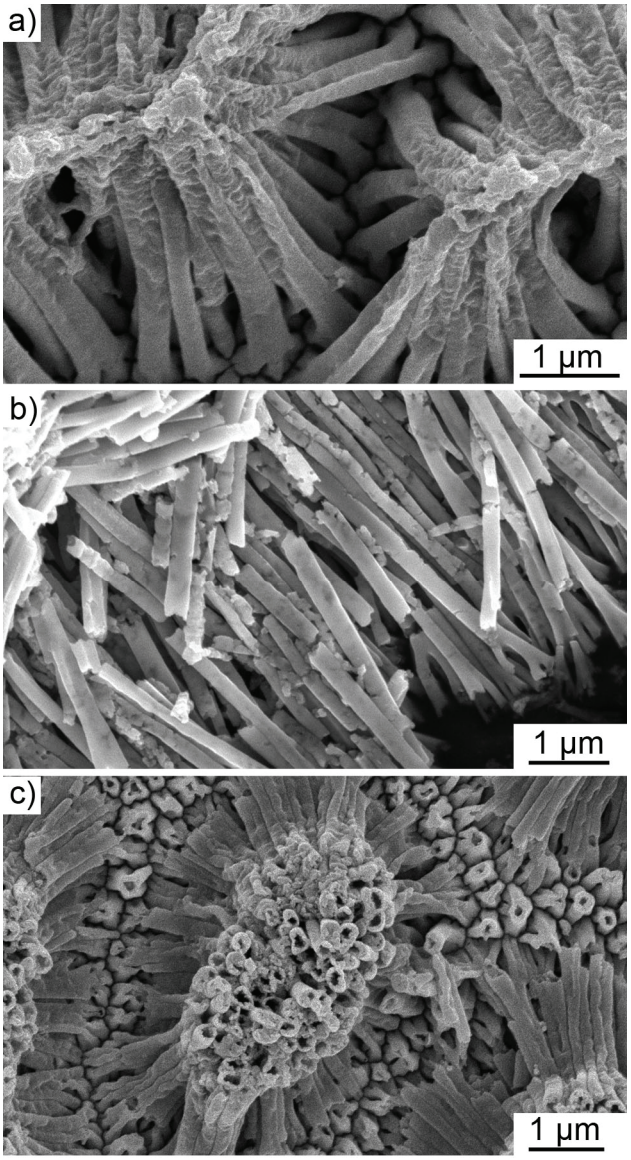

Figure 5.2. SEM images of a) PEDOT nanotubes electrodeposited by the charge density of 300 mC/cm^2 after template removal b) RuO_2 nanowires electrodeposited by 120 CV cycles after template removal c) RuO_2/PEDOT nanotubes after template removal. (RuO_2 is electrodeposited into PEDOT nanotubes by 60 CV cycles.)

Figure 5.3a shows the TEM image of PEDOT nanotubes. The walls of the PEDOT nanotubes can be clearly identified as they appear to be darker under the TEM, while the hollow parts look brighter. As we have observed before, these PEDOT nanotubes

have gradually-thinning walls along with the nanotubes' axes, which can be explained by the gradually-decreasing monomer supply at the tips of the nanotubes during their growth when the PEDOT is electropolymerized at low monomer concentration and high overpotential. Also, these thin, porous top parts of the PEDOT nanotubes cause serious aggregations[260] and collapsing as shown in Figure 5.2a. Figure 5.3b shows a typical TEM image of RuO_2/PEDOT nanotube. The grain-like RuO_2 nanoparticles can be found inside the hollow tubes as well as on the walls, which suggest the RuO_2 is not only deposited onto the internal rough surfaces of PEDOT but also into the their porous walls. Most of the RuO_2/PEDOT composite nanotubes were found broken under TEM due to the sonication during the sample preparation. EDS analysis (Figure 5.4) clearly showed that existence of Ru element and the molar ratio of RuO_2 to PEDOT (sulfur on the thiophene group represents the PEDOT) is 0.95:1.

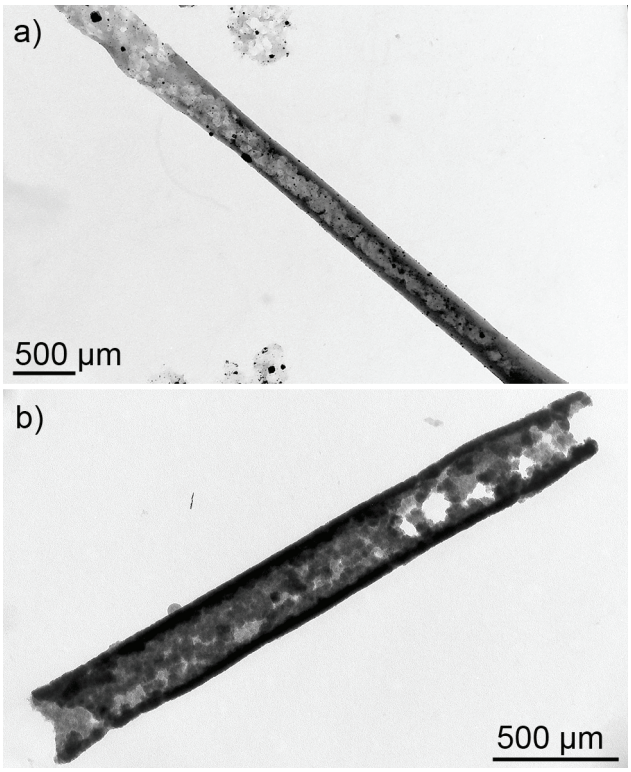

Figure 5.3. TEM images of a) PEDOT nanotubes electrodeposited by the charge density of 300 mC/cm^2 after template removal b) Broken part of RuO_2/PEDOT composite nanotubes after template removal.

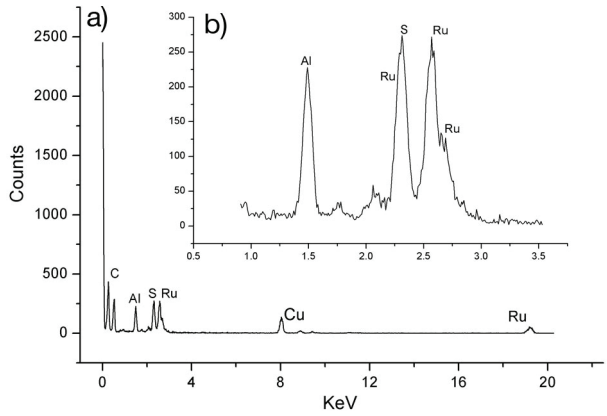

Figure 5.4. EDS analysis of RuO_2/PEDOT composite nanotubes. (a) Overview of the EDS spectra of RuO_2/PEDOT nanotubes (b) Detailed view of S and Ru peaks from the overall EDS spectra of RuO_2/PEDOT nanotubes. Qualitative analysis can be done based on the peak information.

5.3.2 Charge Storage Mechanism and Electrochemical Characterizations of RuO_2/PEDOT composite nanotubes

The charge storage mechanism of RuO_2/PEDOT composite nanotubes as the electrode materials for supercapacitors can be illustrated in Scheme 5.2. Scheme 5.2 (a) is the overview of the charge/discharge process of composite nanotubes. The electrolyte can easily penetrate into the hollow nanotubular structures and access their internal surface. The electrons that are involved in the redox process are transported by the sputtered platinum on the bottom of the alumina template. Scheme 5.2 (b) focuses on the detailed charge storage mechanism of RuO_2/PEDOT composite

nanotubes. The pseudocapacitance behaviors of these composite nanotubes are originated from the ions diffusions during the simultaneous and parallel redox process of RuO_2 and PEDOT. The thin walls of the nanotubular structures allow the fast ion diffusions owing to their small nanoscaled dimensions. During the charge process, the Ru species expel protons (H^+) and are oxidized into their higher oxidative forms. At the same time, the neutral PEDOT is also oxidized into its oxidative form and doped with counterions (A^-, here SO_4^{2-}). The discharge process is the reverse step of the charge process, which is the reduction route of PEDOT and Ru species. During these charge/discharge processes, the protons and counterions are simultaneously provided by the protons and sulfate ions from the dissociated sulfuric acid in the water.

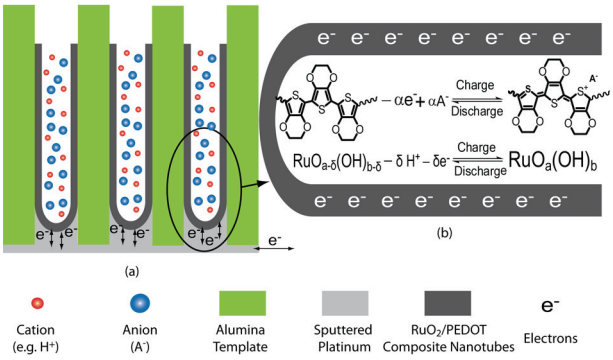

Scheme 5.2. Charge storage mechanism of RuO_2/PEDOT composite nanotubes. (a) overview of the charge/discharge process of composite nanotubes in the supporting electrolyte (b) detailed charge storage mechanism of composite nanotubes.

The electrochemical properties of RuO_2/PEDOT composite nanotubes were studied using cyclic voltammetry and galvanostatic charge/discharge methods. In order to study the impact of RuO_2 deposition on the electrochemical performances of the composite RuO_2/PEDOT nanotubes, we have compared the CV graphs of the PEDOT nanotubes and RuO_2 loaded PEDOT nanotubes in Figure 5.5. It is obvious that

addition of RuO_2 increases the resulting capacitive current dramatically due to the high specific capacitance of RuO_2. The CV shape of the composite nanotubes resembles the CV shapes from the electrochemical growth of RuO_2 (Figure 5.1) since the similar redox process is involved in the RuO_2 charge/discharge process as well as in its electrodeposition process. Because the shape of the CV graph is not ideal rectangular shape and the current is not maintained as a stable value, it is difficult to estimate precisely the specific capacitance from the CV graph based on the equation (5.1). Thus the galvanostatic charge/discharge method is also performed to estimate the specific capacitance and evaluate the power density and energy density.

$$C_{spec} = \frac{i}{m_e \frac{\Delta V}{\Delta t}} \quad , \tag{5.1}$$

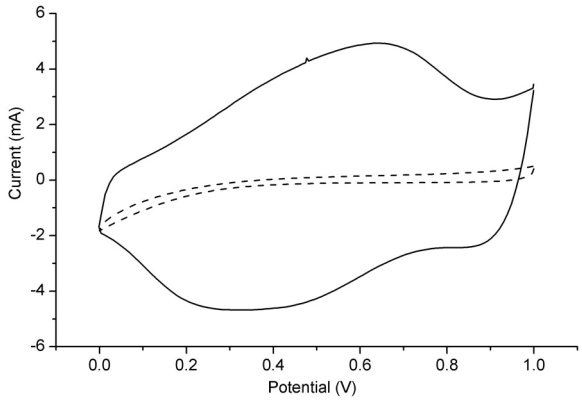

Figure 5.5. Cyclic voltagrams of PEDOT nanotubes (dotted line) and RuO_2/PEDOT composite nanotubes (solid lines) at the scan rate of 50 mV/s from 0-1 V in 1 M sulfuric acid as the electrolyte.

Figure 5.6 shows the galvanostatic charge/discharge curve of RuO_2/PEDOT composite nanotubes obtained at the current density of 5 mA/cm^2 in the standard three electrode system. The high linearity and symmetry of this curve indicate the

high charge/discharge efficiency, which is due to the sufficient ion diffusions into/out of the thin walls of nanotube during its the charge/discharge process. The specific capacitance can be calculated based on equation (5.1), where i is the current used for the galvanostatic charge/discharge experiment, $\Delta V/\Delta t$, potential change rate, can be measured from the reciprocal of the slope on the galvanostatic charge/discharge curve.

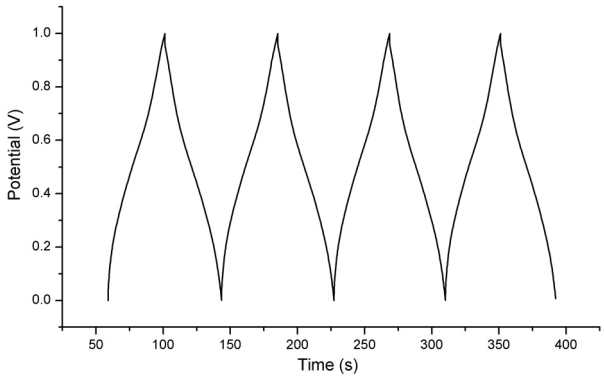

Figure 5.6. Galvanostatic charge/discharge curve of RuO_2/PEDOT composite nanotubes, cycled from 0-1 V at current density of 5 mA/cm^2 in the electrolyte of 1 M sulfuric acid.

m_e is the mass of the electrode, which can be estimated by adding up the mass of the electrodeposited RuO_2 and the PEDOT nanotubes. The mass of the PEDOT nanotubes can be calculated by the total charge used during the electropolymerization of PEDOT. However, the mass of RuO_2 is hard to be estimated in a similar way because the amount of RuO_2 can not be directly associated to the charge accumulated during the CV electrodeposition. But different approach can be used to calculate the mass of RuO_2: since the amount of PEDOT can be determined first, the molar ratio of RuO_2 to PEDOT can also be quantitatively analyzed based on the elemental ratio of Ru to S from the EDS data (Figure 5.4), then the amount of RuO_2 can be easily

deduced. For example, in this chapter, 300 mC/cm^2 charge density of PEDOT on 0.2 cm^2 electrode would give us 0.0343 mg material, and equal mole of RuO_2 would give us 0.0321 mg material. Based on the molar ratio of RuO_2 to PEDOT (0.95:1), the total mass of RuO_2/PEDOT composite nanotubes could be estimated as 0.0648 mg. Thus the specific capacitance for the composite nanotube $C_{spec}^{composite}$ can be directly estimated as 664 F/g based on equation (5.1). The total capacitance of the composite nanotubes can be viewed as the sum of the capacitances from each nanotube because all the nanotubes are connected in parallel on the bottom electrode:

$$C_{composite} = n \times C_{nanotube}^{composite} \tag{5.2}$$

where n is the number of composite nanotubes, $C_{nanotube}$ represents the capacitance value for each nanotube.

The capacitance of each nanotube can be viewed as the contribution from the capacitance of PEDOT nanotube and from the RuO_2 which is later electrodeposited on the PEDOT nanotube because the PEDOT and RuO_2 worked in a parallel manner on a single nanotube during the charge/discharge process, as mentioned earlier in this chapter.

$$C_{nanotube}^{composite} = C_{nanotube}^{PEDOT} + C_{nanotube}^{RuO_2} \tag{5.3}$$

where $C_{nanotube}^{composite}$ represent the capacitance of each composite nanotube, $C_{nanotube}^{RuO_2}$ is the capacitance of PEDOT nanotube before RuO_2 deposition, $C_{nanotube}^{RuO_2}$ is the capacitance contributed from the later deposited RuO_2.

Based on the equation (5.2), (5.3), the total capacitance of composite nanotubes can be simply viewed as the sum of the total capacitance of PEDOT nanotubes and the total capacitance of RuO_2 on PEDOT nanotubes.

$$C_{composite} = C_{PEDOT} + C_{RuO_2} \tag{5.4}$$

where $C_{composite}$ is the total capacitance of composite nanotubes, C_{PEDOT} is the total capacitance of PEDOT nanotubes, C_{RuO_2} is the total capacitance of RuO_2 electrodeposited on PEDOT nanotubes.

The ~~total~~ capacitance of each material can be calculated as the product of specific capacitance of each materials and its mass:

$$C_{spec}^{composite} m_{composite} = C_{spec}^{RuO_2} m_{RuO_2} + C_{spec}^{PEDOT} m_{PEDOT} \tag{5.5}$$

where $C_{spec}^{composite}$ is the specific capacitance of the composite nanotubes, $m_{composite}$ is the mass of the composite nanotubes, $C_{spec}^{RuO_2}$ is the specific capacitance of the RuO_2 that is later deposited, m_{RuO_2} is the mass of RuO_2, C_{spec}^{PEDOT} is the specific capacitance of PEDOT nanotubes, m_{PEDOT} is the mass of the PEDOT nanotubes.

The specific capacitance of PEDOT nanotube is measured as 150 F/g before the loading of RuO_2 (data not shown), while the specific capacitance of composite nanotube is calculated as 664 F/g as mentioned earlier. Based on the equations (5.4) and (5.5), given the mass of the composite, PEDOT, and RuO_2, the specific capacitance of RuO_2 can be derived as 1217 F/g. This specific capacitance value of RuO_2 is much higher than that of the previously reported RuO_2 film, which is also synthesized using similar CV electrodeposition method. The high specific capacitance of RuO_2 is mainly due to its the high surface area that benefits the full utilization of

RuO_2 with the nanotubular structures, which is also reported in elsewhere[42,261]. In addition, because the RuO_2 is directly grown on the PEDOT surface, the rough porous PEDOT surface provides additional high surface area to allow the efficient charge/discharge of RuO_2.

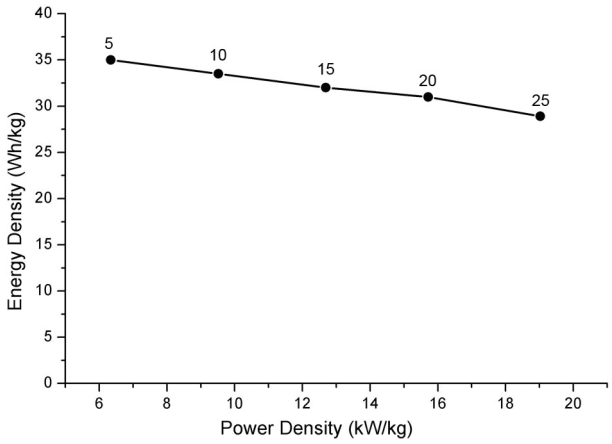

Figure 5.7. The plot of energy density versus power density (Ragone plot) for RuO_2/PEDOT composite nanotubes. The inserted numbers represent the current densities (mA/cm^2) for the charge/discharge.

The experimental values for P_d and E_d were obtained by analyzing the charge/discharge curve of RuO_2/PEDOT composite nanotubes at various current densities using the same method, the detail of which can be found in our previous chapter. Figure 5.7 shows the plot of E_d *vs* P_d, known as Ragone plot, for the composite nanotubes. These composite nanotube are promising electrode materials for supercapacitors, which can maintain 80% their energy densities (28 Wh/kg) and specific capacitance (530 F/g) even when the power density increases from 6 to 20 kW/kg. The high power density (specific power) obtained by the composite nanotubes is benefited from the fast and efficient charge/discharge process that is associated with the fast ion diffusions into/out of the thin walls of the nanotubes. The

similar fast charge/discharge mechanism based on the nanotubular structures is also reported in our previous paper[262]. The high energy density obtained by the composite nanotubes is several folds higher than that of the previously reported pure PEDOT nanotubes because of the high specific capacitance nature of RuO_2. Therefore, the composite RuO_2/PEDOT nanotube is an excellent candidate to provide high power density with little loss of energy density as an electrode material for a supercapacitor.

5.4 Conclusion

We have successfully synthesized RuO_2/PEDOT composite nanotubes by a step-wise electrochemical deposition method in an alumina template and demonstrated these composite nanotubes as promising electrode materials for supercapacitors. The flexible PEDOT and rigid RuO_2 provide mutual mechanical supports for each other. The addition of RuO_2 on the PEDOT nanotubes dramatically enhance the energy density (specific capacitance) of PEDOT nanotubes. The high surface area from the nanotubular structures allows the better utilization of RuO_2 to realize its high specific capacitance value of 1217 F/g. The thin-walled composite nanotubes provided short diffusion paths and low ionic resistance for the diffusion of counter-ions to make all RuO_2/PEDOT composite materials available during complete charge/discharge even at a fast scan rate. This fast electrochemical reaction enables us to achieve high power density without much loss of energy density (specific capacitance), which is the basic requirement for the supercapacitor to meet the demand of modern instruments at high peak power. In order to use these composite nanotubes in supercapacitor devices, optimizations of electrolytes, electrode materials, and cell design needs to be done. This chapter provides the fundamental understandings of electrochemical reactions

that occur on the nanostructured composite materials and also studies their electrochemical properties, which paves the way for the development of other types of composite nanomaterials for the application of electrochemical energy storage.

Chapter 6: MnO_2/Poly(3,4-ethylenedioxythiophene) Coaxial Nanowires by One Step Coelectrodeposition for Electrochemical Energy Storage

6.1 Introduction

As we mentioned in Chapter 1, one-dimensional (1D) nanostructured materials have been intensively investigated as building components in electrochemical energy storage[42,47,263] and solar energy conversion devices[264,265] because they provide short diffusion path lengths to ions and excitons, leading to high charge/discharge rates[42,47,263] and high solar energy conversion efficiency[264,265]. And more recently, heterostructured coaxial nanowires have attracted greater attention in this field due to their added synergic properties (e.g. high conductivity)[84] or functionalities (e.g. core/shell p-n junction)[266,267] arising from the combination of different material. Various materials such as semiconductor/semiconductor, metal/metal oxide, and metal oxide/metal oxide, have been employed as core/shell in coaxial nanowires[41,164,267-269]. However, there have been few studies on the coaxial nanowires with transition metal oxide and conductive polymer, although both of them are important electroactive materials used in electrochemical energy storage[80,209,270]. The combination of these two materials at 1D nanostructures may exhibit excellent electrical, electrochemical, and mechanical properties for electrochemical energy storage. To date, only a few reports have been published on the synthesis of metal oxide/conductive polymer with core/shell structures. In all of these reports, a step-wise synthetic approach was adopted: metal oxide nanoparticles, nanostrands or

nanotubes were first synthesized and subsequently coated chemically by conductive polymers as shells[108,271,272].

In this chapter, we introduce a simple one-step method to synthesize MnO_2/poly(3,4-ethylenedioxythiophene) (PEDOT) coaxial nanowires by coelectrodeposition in a porous alumina template. MnO_2 is one of the most popular electrochemical energy storage materials due to its high energy density, low cost, environmental friendliness and natural abundance[273], but it has poor conductivity[270]. PEDOT has merits of excellent conductivity, high stability, and mechanical flexibility[274], but it provides low electrochemical energy density. Electrodeposition is used here because it is a simple yet versatile method in controlling structures and their composition by tuning applied potentials and electrolyte ingredients[166,275,276]. In this report, MnO_2/PEDOT coaxial nanowires are found to be promising electrochemical energy storage materials. The core MnO_2 provides high energy storage capacity while the highly conductive, porous, and flexible PEDOT shell facilitates the electron transport and ion diffusion into the core MnO_2 and protects it from structurally significant collapsing and breaking. These combined properties enable the coaxial nanowires to have very high specific capacitances at high current densities.

6.2 Experiemtal Details

6.2.1 Chemicals and Materials

3,4-Ethylenedioxythiopene (EDOT), manganese acetate and lithium perchlorate ($LiClO_4$) were purchased from Sigma Aldrich (Milwaukee, WI). Sodium dodecyl sulphate and sodium sulfate were obtained from Fisher Scientific (Fair Lawn, NJ). De-ionized water (ca. 18 $M\Omega \cdot cm^{-1}$ in resistivity) was made by a Milli-Q water

purification system (Millipore; Dubuque, IA). Alumina membranes of 200 nm in pore diameter and 60 μm in thickness are commercially available from Whatman (Clifton, NJ). Indium tin oxide (ITO) glass (R_s=4-8 ohms, thickness 1.1 mm) was commercial available from Delta Technologies Limited.

6.2.2 Synthesis

Coaxial MnO_2/PEDOT nanowires were synthesized potentiostatically at 0.7-0.8 V an aqueous solution of 10 mM manganese acetate, 80 mM EDOT, 100 mM $LiClO_4$ and 140 mM SDS (pH=6.5). MnO_2 nanowires were synthesized at 0.75 V in an aqueous solution of 10 mM manganese acetate. PEDOT nanowires were synthesized at 1 V in 80 mM EDOT, 100 mM $LiClO_4$ and 140 mM SDS. Bulk MnO_2 film was synthesized at 0.5 V in aqueous solution of 100 mM manganese acetate on ITO glass. All electrode potentials were measured relative to an Ag/AgCl reference electrode using a Pt foil as a counter electrode, if not specified otherwise. The preparation of a working electrode is as follows: First, a thin layer of gold (ca. 500 nm) was sputtered onto the branched side of an alumina membrane by using a sputtering system (Denton Vacuum Desktop III). The Au-coated membrane was connected to an electrical circuit using a copper tape (3M). Defining and sealing an electroactive window (0.32 cm^2 in nominal area) was performed using silicone rubber or parafilm. Considering the porosity of the membrane (60 %), the corrected surface area of the electroactive window was 0.2 cm^2. The mass and the length (thickness in film) of the resulting MnO_2 nanowires, PEDOT nanowires, MnO_2/PEDOT coaxial nanowries, MnO_2 bulk film, was controlled by fixing the total charges passed during the electrodeposition.

Typically coaxial nanowires with lengths of 10 μm can be obtained after the charge passed about 200 mC. Diameters of these nanowires are corresponded to the pore diameters of alumina template (ca. 300 nm).

6.2.3 Characterizations

The nanowires were investigated using a field-emission scanning electron microscope (SEM; Hitachi S-4700, operated at an acceleration voltage of 5 keV) and transmission electron microscope (Jeol 2100F Field Emission Transmission Electron Microscope (FE-TEM), 200 keV). The sampling methods for SEM and TEM analysis were briefly described: gold-coated side of a small piece of an alumina template was tightly attached onto an SEM specimen holder by using a carbon tape. The template was dissolved to expose the nanowires by using 3 M NaOH. After rinsing it with de-ionized water repeatedly, the sample was dried in air before observation. For TEM sampling, 3M NaOH was used to remove the template and aqua regia was used to remove the gold layer and core MnO_2. The released nanowires were repeatedly rinsed with de-ionized water and ethanol. Then, 6 μL of the nanowire solution was dropped and dried on a TEM grid.

In order to calculate specific capacitance, galvanostatic charge/discharge test were performed by cycling potential from 0 to 1 V at different current densities. Cyclic voltammetry was performed in a potential range between 0 and 1 V at different scan rates of 250 mV/s in 1 M Na_2SO_4. All the above electrochemical experiments were performed using a bi-potentiostat (BI-STAT; Princeton Applied Research).

6.2.4 Calculations

Specific capacitance $C_{spec}=I/(dV/dt)m_e$, dV/dt is the potential change rate determined from galvanostatic charge/discharge curve, m_e is the mass of electrochemically active materials. For MnO_2 nanowires, MnO_2 bulk film and PEDOT nanowires, the mass of electrode is calculated from the charge passed for the electrochemical deposition. For MnO_2/PEDOT nanowires, their mass is obtained based on the total charge and the molar ratio of MnO_2 to PEDOT determined by the EDS.

6.3 Results and Discussion

Scheme 6.1 illustrates the growth of MnO_2/PEDOT coaxial nanowires. Under a constant potential (typically 0.75 V v.s. Ag/AgCl), Mn^{2+} (10 mM manganese acetate) is converted to its higher oxidization state, which can readily undergo hydrolysis to yield MnO_2. Simultaneously, EDOT monomer (80 mM) is electropolymerized into PEDOT in the pores of the template[277]. Very interestingly, this coelectrodeposition gives rise to formation of coaxial nanowires.

Figure 6.1a shows the SEM image of free standing coaxial nanowires grown at 0.75 V after removal of template. Figure 6.1b shows the TEM image of a single coaxial nanowire. Although the core MnO_2 and shell PEDOT can be easily distinguished by their morphologies in TEM images, energy dispersive X-ray spectroscopic (EDS) elemental maps of S and Mn (Figure 6.1c and 6.1d) from the designated area in Figure 6.1b clearly confirms the coaxial nanostructure. The electron diffraction pattern reveals that the core MnO_2 is amorphous (Figure 6.2).

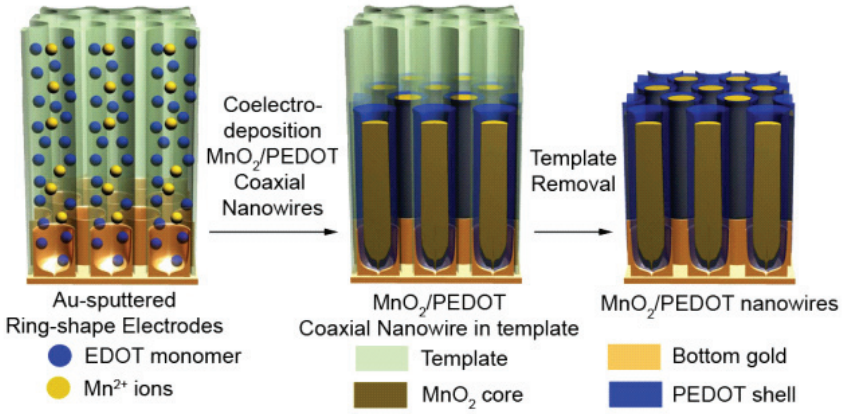

Scheme 6.1. One step synthesis of MnO_2/PEDOT coaxial nanowires

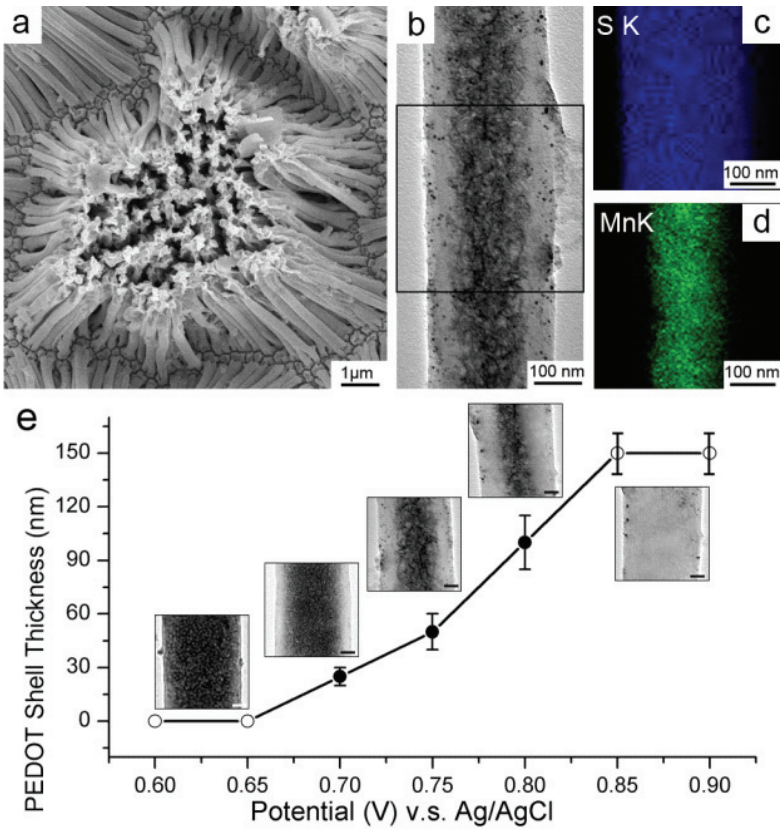

Figure 6.1. a) SEM image of MnO_2/PEDOT coaxial nanowires (0.75 V) b) TEM image from a single coaxial nanowire (0.75 V) c) and d) EDS maps of S and Mn from

the boxed area in Figure 6.1b e) PEDOT shell thickness variation with applied potential, scale bar, 50 nm.

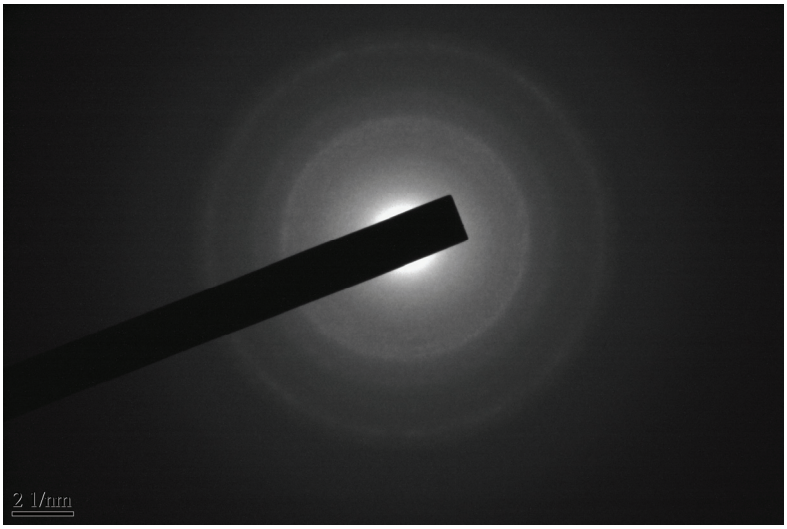

Figure 6.2. Electron diffraction pattern on coaxial nanowires synthesized at 0.75 V

We can easily control the structures of coaxial nanowires such as PEDOT shell thickness and nanowire length by varying the applied potential. This should provide us with the ability to tune electrochemical properties of the coaxial nanowires. Since the onset growth potential of MnO_2 (0.5 V) is lower than that of PEDOT (0.75 V), MnO_2 nanowires can be selectively grown below 0.6 V, while PEDOT nanowires are grown at the potentials above 0.85 V due to higher growth rate of PEDOT given the concentration of EDOT monomer is 8 times of Mn^{2+}. Between these two extreme potentials, coaxial nanowires with various PEDOT shell thicknesses (25 to 100 nm) can be obtained, as shown in Figure 6.1e. After the MnO_2 cores in these coaxial nanowires are selectively removed by wet etching, PEDOT nanotubes with different wall thicknesses are obtained and clearly observed by TEM (Figure 6.3).

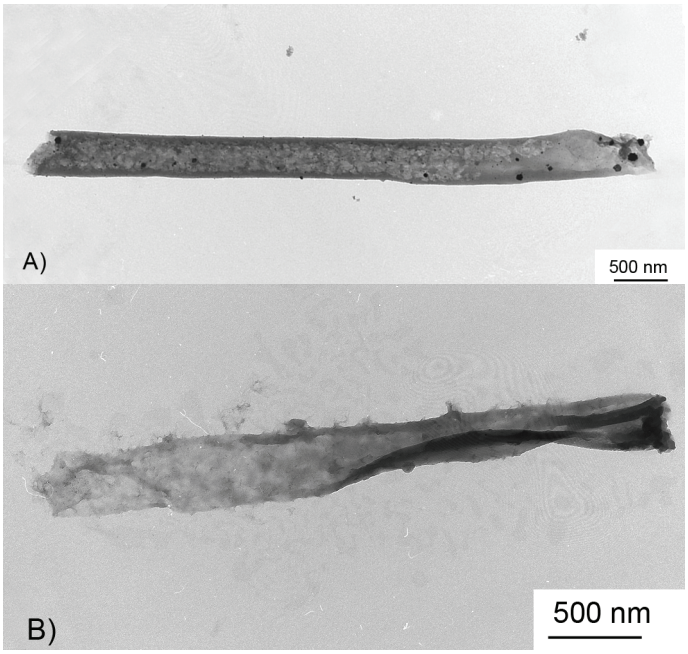

Figure 6.3. TEM of the corresponding PEDOT nanotubes after removal of the template and the core MnO_2 (A) PEDOT nanotubes obtained from MnO_2/PEDOT coaxial nanowire synthesized at 0.75 V (B) thin PEDOT nanotubes (collapsed and twisted) obtained from MnO_2/PEDOT coaxial nanowire synthesized at 0.7 V.

Interestingly, the inner surface morphology of PEDOT nanotubes appears somewhat rough and spiky. It suggests the PEDOT may have grown into the MnO_2 core layer. This can be supported further by EDS line-scan profile on a single coaxial nanowire (Figure 6.4). Such PEDOT penetrations may play important roles in further improving the core conductivity.

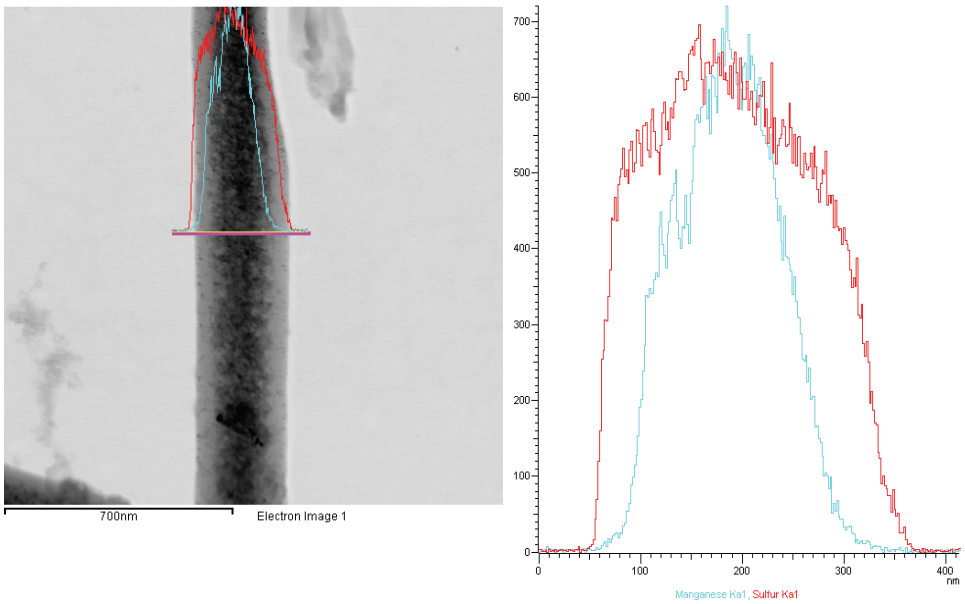

Figure 6.4. EDS line-scan elemental analysis of sulfur (red) and manganese (blue) on a single coaxial nanowire. When compared to elemental mapping cross-section from coaxial nanowires that have pure phases in their cores and shells, the elemental mapping profile of sulfur indicates that PEDOT may have grown into the MnO_2 core.

The growth mechanism of coaxial nanowires, although not completely understood, is briefly suggested as follows. We have previously proved that the sputtered ring-shape Au electrodes at the bottom of the pores can direct the growth of PEDOT nanotubes at low overpotential. This may explain the preferential formation of the PEDOT shell. In addition, MnO_2 and PEDOT tend to have phase segregation when coelectrodeposited at bulk electrode surface (Figure 6.5). The phase segregation of these two materials may force the MnO_2 grow in the spaces left by the PEDOT shells as the cores.

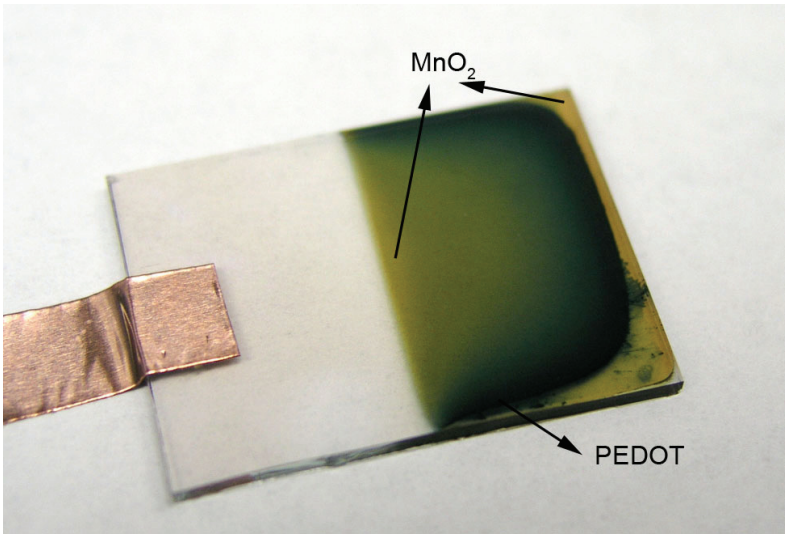

Figure 6.5: Phase segregation when PEDOT and MnO_2 are coelectrodeposited on the bulk ITO electrode at 0.75 V in the same aqueous solution used for the synthesis of coaxial nanowires.

Finally, we investigate electrochemical properties of the coaxial nanowires for an electrochemical supercapacitor: an electrochemical energy storage device required to provide high power while it maintains its energy density (or specific capacitance) at high charge/discharge rate. Specific capacitance values of coaxial nanowires (grown at 0.75 V), MnO_2 nanowires, PEDOT nanowires, and MnO_2 thin film at different current densities are shown in Figure 6.6.

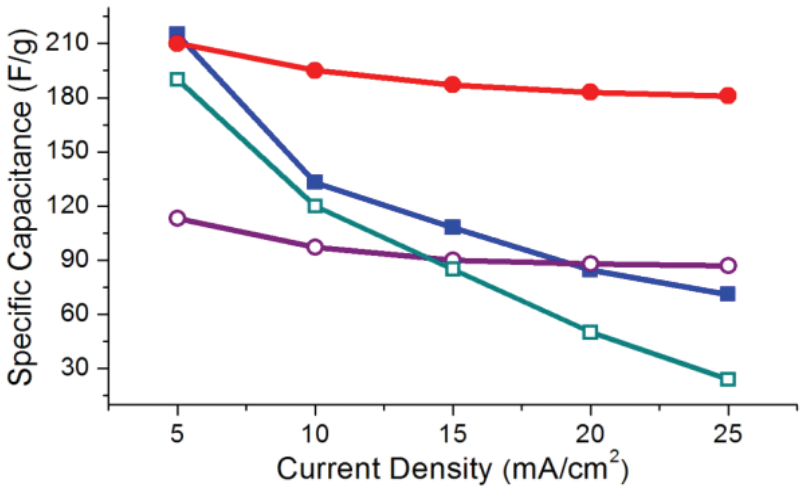

Figure 6.6. Specific capacitance of MnO_2 nanowires (closed blue square), PEDOT nanowires (open purple dots), MnO_2 thin film (open green square) and MnO_2/PEDOT coaxial nanowires (closed red dots) at difference charge/discharge current densities.

Coaxial nanowires exhibit not only high specific capacitance values but also maintain them well at high current density compared to the others. As shown in Figure 6.6, the coaxial nanowires preserved 85% of its specific capacitance (210 to 185 F/g) as the current density increases from 5 to 25 mA/cm^2. These specific capacitance values are comparable to those of electrodeposited MnO_2 films (190-240 F/g), which, however, decreased significantly with increased current densities (e.g. 210 to 40 F/g at current density of 1 to 10 mA/cm^2). The specific capacitance of coaxial nanowires is higher than that of PEDOT nanowires due to the inclusion of MnO_2 as cores. The well-maintained specific capacitance is mainly due to short paths of ion diffusion in the nanowires. Therefore, even at high current density (high power demand), the nanowire materials can be fully utilized. The porous nature of the PEDOT shell allows such fast ion diffusion into the core MnO_2 of the coaxial

nanowires. In addition, the highly electrical conductive PEDOT shell facilitates electron transport to the core MnO_2, which has low conductivity that can limit its charge/discharge rate (cyclic voltammogram in Figure 6.7).

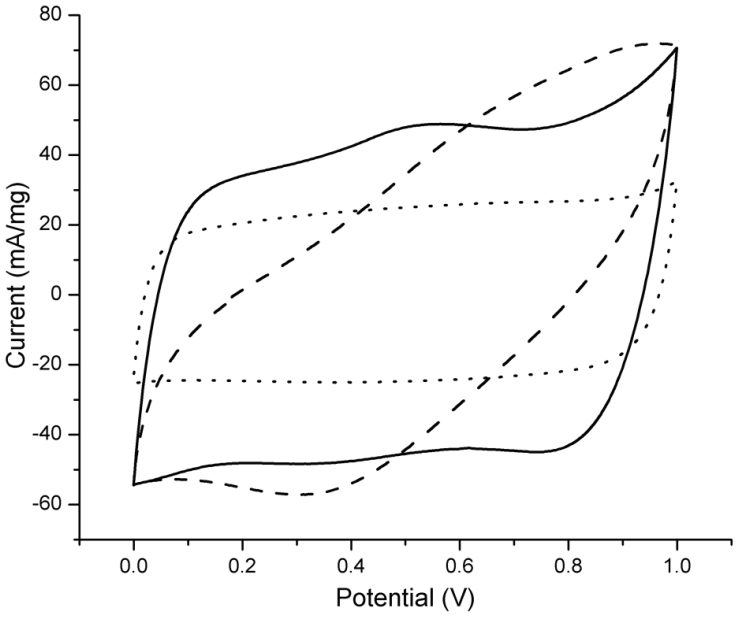

Figure 6.7. Cyclic voltammograms (CV) of PEDOT nanowires (dotted line), MnO_2 nanowries (dashed line), MnO_2/PEDOT coaxial nanowires (solid line) scanned from 0-1 V in 1 M Na_2SO_4 (aq) at the scan rate of 250 mV/s. The CV shape of coaxial nanowires is more rectangular-like than that of MnO_2 nanowires, suggests that coaxial nanowires exhibit the behaviors more like an ideal capacitor.

It also explains the significant decrease of specific capacitance of pure MnO_2 nanowires. With regard to mechanical stability, the solid core MnO_2 and the flexible PEDOT shell prevent, synergistically, the coaxial nanowires from significant collapsing and breaking after removal of the template and the drying process that downgrades their electrochemical performance (Figure 6.8 and 6.9).

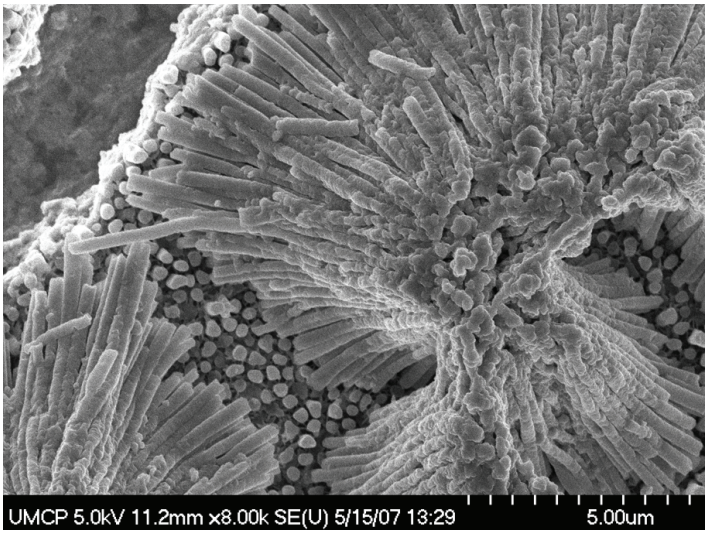

Figure 6.8: SEM image of MnO_2 nanowires after removal of template and drying process. Significant breaking and collapsing can be clearly seen.

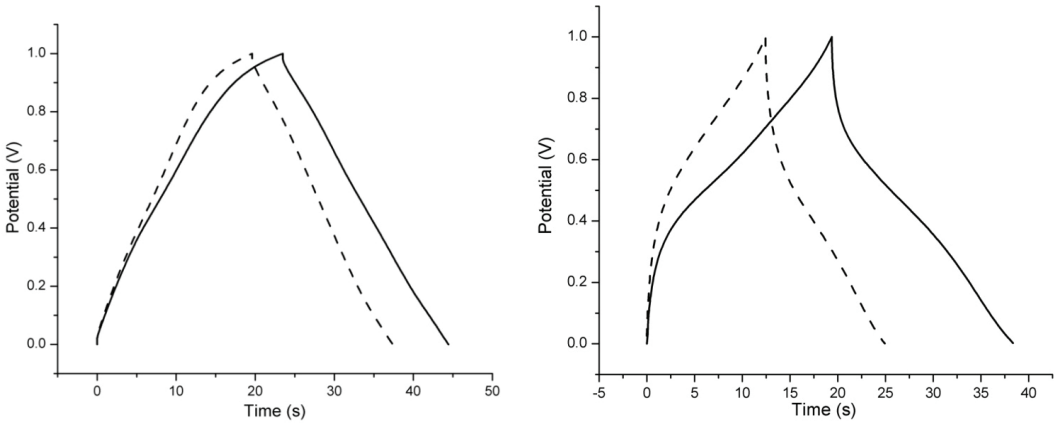

Figure 6.9: Galvanostatic charge/discharge curve before (solid) and after drying (dashed) for (A) MnO_2 nanowires, and (B) MnO_2/PEDOT coaxial nanowires. MnO_2 nanowires lose the specific capacitance more significantly than MnO_2/PEDOT nanowires.

6.4 Conclusion

In conclusion, MnO_2/PEDOT coaxial nanowires were fabricated by a one-step coelectrodeposition method. The structures of the coaxial nanowires could be controlled by applied potential. The combination of MnO_2 and PEDOT into 1D nanostructures showed excellent electrochemical and mechanical properties for energy storage applications. The synthetic method presented here will be further investigated for the extension to fabricating other heterogeneous 1D nanocomposite structure with other metal oxides[150] and conductive polymers, which may lead to new types of materials in electrochemical energy storage devices.

Chapter 7. Exploring the Formation Mechanism and Tuning the Nanostructures of the Coelectrodeposited MnO_2/Poly (3,4-ethylenedioxythiophene) Coaxial Nanowires for the Applications of Electrochemical Energy Storage.

7.1 Introduction

As we mentioned in Chapter 1, nanomaterials with single material may not be able to fulfill the requirements of future EES due to its limitations, such as low energy densities, slow kinetics (low power densities), poor conductivities and weak mechanical stabilities[79,278]. Thus, in order to meet the challenges for nano-based energy storage, heterogeneous nanostructured materials, which have multi-nanocomponents, each tailored to address different demands (e.g. high energy density, high conductivity and excellent mechanical stability), are necessitated. The resulting materials will exhibit synergic properties of each component, which can realize the full potentials of the materials with excellent performance (e.g. high energy density and high power density). However, the success of applying heterogeneous nanostructured materials in the energy storage will hinge on a few factors (1) how to choose a proper combination of different materials (2) how to design and optimize the heterogeneous nanostructure, for example, coaxial nanowires[81,84,109], segmented nanowires, core-shell nanoparticles[82,83]. (3) how to synthesize or assemble the nanocomponents into the desired and proposed nanostructures.

The second factor is especially important because the material properties can be dramatically enhanced if the appropriate nanostructure is chosen. One-dimensional

nanostructure array is one of the ideal nanostructure that has been intensively studied in the field of energy storage not only because the radically small dimensions can effectively shorten the diffusion lengths of the ions which can improve the charge/discharge rate capabilities but also because the axially big dimensions can provide high surface area and enough mass loading for electrode materials to store sufficient energy[42,76,97,103,107,152,154,263]. For example, Martin's group, has reported enhanced charge transport rates in template-synthesized one-dimensional nanomaterials. Nanotubes of RuO_2 and PEDOT have been reported for high power supercapacitors by Hu's group[42] and our group respectively[43]. The next question rises on how to accommodate different materials into a heterogeneous nanostructure and how to optimize the structure and composition of each nanocomponent to fully bring its potentials into play. In order to achieve these aims, a well understood, mature synthetic approach has to be developed. Core-shell nanoparticles composed with $LiFePO_4$/Carbon have been reported for enhanced conductivities as well as fast charge/discharge rate[83]. Coaxial nanowires or nanotubes have also attracted an increasing amount of attention due to their advantages of added synergetic properties of functionalities as well as the benefits from the one dimensional nanostructures mentioned earlier. For example, SnO_2-In_2O_3 heterostructured nanowires[84] and coaxial MnO_2/Carbon nanotube array electrodes[81] have been reported for high performance lithium ion batteries. The previous chapter also demonstrated the coaxial MnO_2/PEDOT nanowire for the applications of supercapacitor. The core MnO_2 provides high energy density, while the highly conductive, porous, and flexible PEDOT shell facilitates the electron transport and ion diffusion into the core MnO_2

and protects it from structurally significant collapsing and breaking. These combined properties enable the coaxial nanowires to have very high specific capacitances at high current densities. However, there is a lack of completely understanding of coaxial nanowire formation mechanism and also fine tuning of nanostructures of the coaxial nanowires to realize their full potentials.

In this chapter, we investigate the detailed growth mechanism of coaxial manganese oxide/poly (3,4-ethylenedioxythiophene) (MnO_2/PEDOT) by performing the coelectrodeposition of MnO_2 and PEDOT on the sputtered nanoelectrodes with different shapes and different sizes (200 nm and 60 nm) within the alumina template channels. The sharp ring shape electrode is found to have crucial role to direct the growth of the PEDOT nanotube shells while the flat top electrode is more favorable to the deposition of MnO_2. The formation of the coaxial nanowires can be viewed as the concurrent growth of core MnO_2 and shell PEDOT. The structures of the MnO_2/PEDOT coaxial nanowires were optimized for their applications of supercapacitors by tuning the potential for the coelectrodeposition. 0.70 V is found to be the best condition to synthesize MnO_2/PEDOT coaxial nanowires which can have high specific capacitance of 270 F/g at cyclic voltammetry scan rate of 250 mV/s. Such high specific capacitance is due to the minimal usage of shell PEDOT materials, which can provide the high conductivities while not dragging down the high specific capacitance of MnO_2. By simply altering the potentials and controlling the charge for the electrochemical deposition, bar-coded MnO_2/PEDOT nanowires with different lengths of MnO_2 or PEDOT segments can be fabricated.

7.2 Experimental Details

Chemicals and Materials. 3,4-Ethylenedioxythiopene (EDOT), manganese acetate and lithium perchlorate ($LiClO_4$) were purchased from Sigma Aldrich (Milwaukee, WI). Sodium dodecyl sulphate was obtained from Fisher Scientific (Fair Lawn, NJ). De-ionized water (ca. 18/ MΩ·cm resistivity) was made by a Milli-Q water purification system (Millipore; Dubuque, IA). Alumina membranes of 200 nm in pore diameter and 60 μm in thickness are commercially available from Whatman (Clifton, NJ). An alumina template with a pore diameter (ca. 80 nm) was fabricated by using a two-step anodization process. The briefs of this process are as follows. An electropolished aluminum foil (99.99%, Alfa Aesar) was anodized at 40 V and 10 °C by using 0.3 M oxalic acid as an electrolyte. This generated an alumina layer with irregular pores. For better pore structures, this porous alumina layer was removed by using an aqueous mixture of phosphoric acid (6 wt %) and chromic acid (1.8 wt %), which exposed the barrier layer with a well-defined prepattern. The second anodization was performed as in the first anodization to generate well-defined pores until a desired thickness (ca. 100 μm) was reached. After the residual aluminum was dissolved using a mixture of 0.5 M $CuCl_2$ and 37 % HCl aqueous solution, the removal of the alumina barrier layer and pore-widening were performed by using phosphoric acid (5 wt %) at 30 °C for 80 mins.

Synthesis. Coelectrodeposition of heterostructured MnO_2/PEDOT nanowires on ring shaped electrodes in different pore size membrane as well as on the flat top electrodes were performed potentiostatically at 0.6-1 V an aqueous solution of 10 mM manganese acetate, 80 mM EDOT, 100 mM $LiClO_4$ and 140 mM SDS (pH=6.5).

Gold bottoms for flat top electrodes were electrochemically deposited at the current density of -1 mA/cm^2 for 30 mins in the Orotemp 24 gold plating solution. All electrode potentials were measured relative to an Ag/AgCl reference electrode using a Pt foil as a counter electrode, if not specified otherwise. The preparation of a working electrode is as follows: First, a thin layer of gold (ca. 500 nm) was sputtered onto the branched side of an alumina membrane by using a sputtering system (Denton Vacuum Desktop III). The Au-coated membrane was connected to an electrical circuit using a copper tape (3M). Defining and sealing an electroactive window (0.32 cm^2 in nominal area) was performed using silicone rubber or parafilm. Considering the porosity of the membrane (60 %), the corrected surface area of the electroactive window was 0.2 cm^2. The mass and the length of the resulting heterogeneous nanowires or MnO_2 and PEDOT segments are controlled by fixing the total charges passed during the electrodeposition. Diameters of these nanowires are corresponded to the pore diameters of alumina template.

Characterizations. The heterogeneous MnO_2/PEDOT nanowires were investigated using a field-emission scanning electron microscope (Hitachi SU-70 SEM, operated at an acceleration voltage of 10 keV) and transmission electron microscope (JEOL JEM 2100 Field Emission Transmission Electron Microscope (FE-TEM), 200 keV). The sampling methods for SEM and TEM analysis were briefly described: gold-coated side of a small piece of an alumina template was tightly attached onto an SEM specimen holder by using a carbon tape. The template was dissolved to expose the nanowires by using 3 M NaOH. After rinsing it with de-ionized water repeatedly, the sample was dried in air before observation. For TEM sampling, sonication is applied

to the heterostructured MnO_2/PEDOT nanowires to disperse them in ethanol. The released nanowires were repeatedly rinsed with de-ionized water and ethanol. Then, 6 μL of the nanowire solution was dropped and dried on a TEM grid.

In order to calculate specific capacitance, cyclic voltammetry at different scan rate (50-500 mV/s) and galvanostatic charge/discharge test at different current density (10-50 mA/cm^2) were performed by cycling potential from 0 to 1 V in 1 M $LiClO_4$ in water. Detailed calculation method can be found in our previous paper. All the above electrochemical experiments were performed using a bi-potentiostat (BI-STAT; Princeton Applied Research).

7.2 Results and Discussion

In our previous paper, we have proposed a simple growth mechanism for MnO_2/PEDOT coaxial nanowires: PEDOT nanotubes are preferentially grown on the sputtered ring-shape Au electrodes at the bottom of the pores via the electropolymerization of EDOT. And MnO_2 is grown as the cores due to the phase segregation by the hydrolysis of oxidized manganese ions from Mn^{2+}, as illustrated in Scheme 7.1a. In order to prove this mechanism, we performed coelectrodeposition of MnO_2 and PEDOT on the flat top Au electrode as a comparative study. (Flat-top Au electrodes are obtained by flattening the ring-shape electrodes via electrodepositing Au into the alumina membranes.) Our experimental results showed that the nanostructures of the coelectrodeposited MnO_2 and PEDOT on the flat top electrodes are very different from MnO_2/PEDOT coaxial nanowires on the ring-shape

electrodes. Our previous paper showed that, the PEDOT nanotubes with different thickness can be obtained by controlling potentials for the electrodeposition from 0.7 V to 0.8V. Lower potential (0.6-0.65 V) will result in the growth of pure MnO_2 nanowires while higher potentials (0.85 to 1 V) will lead to the formation of pure PEDOT nanowires. However, in this chapter, we found on the flat top electrodes, no coaxial nanowires growth can be discovered. Also, the onset potential of PEDOT growth on the flat top electrodes is shifted higher value compared to the PEDOT growth on the ring-shape electrodes. For example, on the ring-shape electrode, 0.75 V will lead to the formation the MnO_2/PEDOT coaxial nanowire with Mn/S mole ratio of approximate 1:1. However, on the flat top electrode, at 0.75 V, almost pure MnO_2 are grown, no PEDOT shells can be distinctively seen. (data not shown) We found the PEDOT can only be clearly indentified when potential higher 0.85V is applied for the electrodeposition. And very interestingly, the PEDOT is not grown as uniform shells which surround the MnO_2 cores. Instead, the PEDOT is grown on the top of a gradually thinning MnO_2 segment, which is first deposited on the flat Au electrodes. (Scheme 7.1b) Figure 7.1a shows the TEM image of a typical heterostructured MnO_2/PEDOT nanowire that is grown the flat top electrode at 0.85 V. As seen in our previous paper, the MnO_2 bottom appears darker than the top PEDOT part. Figure 7.1b and shows the EDS element line scan profiles along the axis of this nanowire (Mn represents the MnO_2 and S from the thiophene ring represents the PEDOT, which is from the sulfur on the thiophene ring). As we can see, the Mn EDS line show that right on the top of the flat electrode, the MnO_2 has much higher concentration than the PEDOT, thereafter, the MnO_2 ratio starts to fall off, and the

diameter of the MnO_2 segment becomes smaller. The PEDOT concentration shows exactly the opposite trend along the axis. At the tip of this nanowire, only pure PEDOT is grown. Figure 7.1c shows the EDS mapping of Mn and S, which further proves the distribution of MnO_2 and PEDOT on the heterostructured MnO_2/PEDOT nanowire. This phenomenon alludes that the flat top electrode has strong selectivity to the growth of MnO_2 while not to the growth of PEDOT. This also reinforce the formation mechanism of coaxial nanowires stated earlier: MnO_2 core is grown the smooth inner surface of the rings and PEDOT shell is selectively grown on the sharp edge of the ring. The phase separation between these two materials keeps them from separated as cores and shells. (Scheme 7.1a) The gradually thinning of the MnO_2 is due to depletion of Mn^{2+} due to the limited diffusion of low concentration of Mn^{2+} at high over potential. Once the Mn^{2+} is almost depleted, the PEDOT becomes overwhelmed on the top of MnO_2, which may block the further growth of MnO_2 because mutual exclusion of MnO_2 and PEDOT.

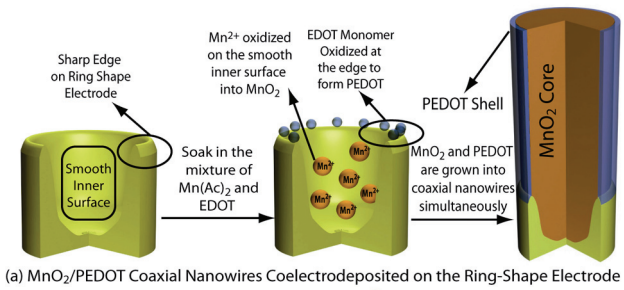

(a) MnO_2/PEDOT Coaxial Nanowires Coelectrodeposited on the Ring-Shape Electrode

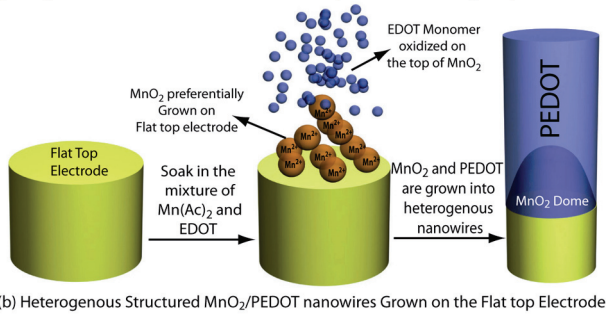

(b) Heterogenous Structured MnO_2/PEDOT nanowires Grown on the Flat top Electrode

Scheme 7.1. Growth mechanisms of heterogeneous nanostructured MnO_2/PEDOT by performing coelectrodeposition of MnO_2 and PEDOT on (a) ring-shape (b) flat-top electrodes

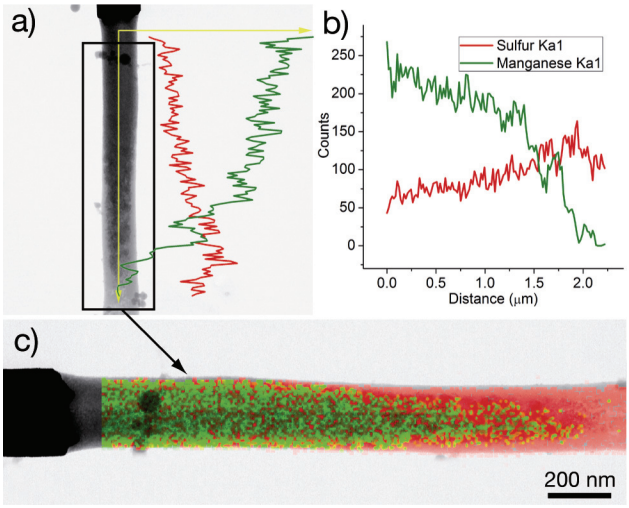

Figure 7.1. (a) TEM image of a heterostructured MnO_2/PEDOT nanowire grown on flat Au electrode at 0.85 V (b) Mn (green) and S (red) EDS line scan profiles along the axis of same nanowire in (a). (c) Mn (green) and S (red) EDS mapping on the framed area in (a).

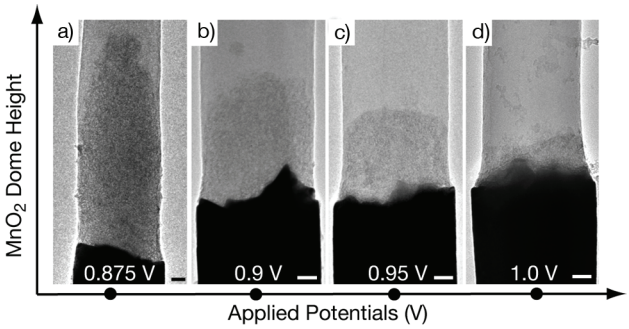

Figure 7.2. MnO_2 nano-dome height versus the potentials applied for the electrodeposition of MnO_2 and PEDOT on the flat top electrodes.

It is worth of noting that when the potential is further increased for the coelectrodeposition of MnO_2 and PEDOT on the flat top electrodes, the MnO_2

segment on the flat top electrode becomes shorter, which may further be reduced into a "dome" shape as shown in the Figure 7.2b-7.2d. This can be explained by the quicker depletion of Mn^{2+} driven by the higher over potentials as well as the faster coverage of PEDOT top.

In order to further prove the proposed mechanism of MnO_2/PEDOT coaxial nanowires growth, we studied the electrodeposition of MnO_2, PEDOT and MnO_2/PEDOT using cyclic voltammetry (CV) methods as well as potential static methods. Figure 7.3 shows the CV graphs of MnO_2 and PEDOT electrodeposition in the alumina template, respectively. The occurrence of symmetric peaks (Figure 7.3b) in the CV graph of MnO_2 deposition is due to the limited diffusion of low concentration Mn^{2+} on the nanosized electrode surface, while the position of the peaks indicates the oxidation of Mn^{2+} and the reduction of MnO_2 or other Mn species with higher oxidation valence status. As we can see, the MnO_2 starts to grow at 0.5 V. The CV graph of PEDOT is much easier to understand: the resulting current is sharply increased after 0.8 V due to the high concentration of EDOT monomer.

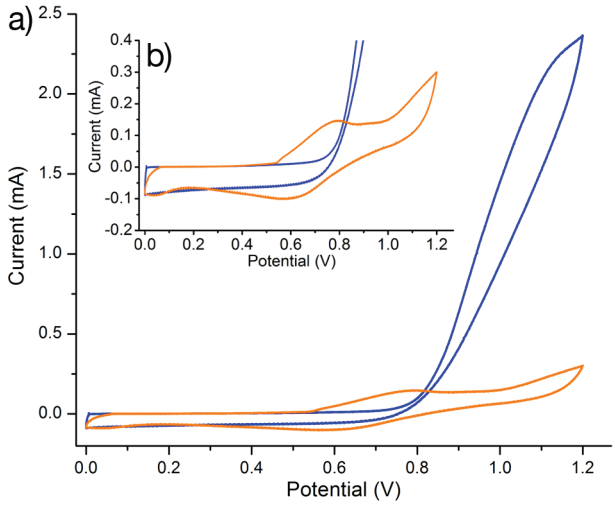

Figure 7.3. (a) Cyclic voltammetry graphs of MnO_2 (10 mM) and PEDOT (80 mM) growth on the ring shape electrodes in the alumina template at the scan rate of 100 mV/s from 0 to 1.2 V. (b) magnified view of MnO_2 cyclic voltammetry graph

We also studied and listed the steady currents (Table 7.1) for the potential static electrodeposition of single component of MnO_2 (i_{MnO_2}) and PEDOT (i_{PEDOT}) as well as the current for MnO_2/PEDOT coelectrodeposition (i_{co}) in the alumina template. As we can see, the sum of the i_{PEDOT} and i_{MnO_2} matches the observed i_{co} very well at 0.75V and 0.85 V. This provides additional proof for the previous stated mechanism. The growth of coaxial nanowires (related to i_{co}) can be viewed as sum of the separate growth of MnO_2 core (resulting i_{MnO_2}) on the ring inner surface and the PEDOT shell (i_{PEDOT}) growth on the ring edge. However, the i_{co} at higher potentials (0.85 V) only matches the i_{PEDOT}, which suggested the overwhelmed growth of PEDOT quickly covers the edges and grows into solid nanowires, which may exclude the further deposition of MnO_2. i_{PEDOT} measured at 0.6 V and 0.70 V can be larger than the real current contributed from PEDOT growth during the coelectrodeposition of MnO_2/PEDOT coaxial nanowires. (Resulting steady current of i_{PEDOT} is proportional to the electrode area, which can become larger because the PEDOT growth is not restricted to the bottom ring: further deposition of PEDOT can occur on the inner surface of initial formed PEDOT nanotubes.) We can also predict the mole ratio of MnO_2 to PEDOT based on i_{MnO_2} and i_{PEDOT} resulted from their electrochemical reactions for the electrodeposition. We also listed the experimentally observed Mn/S mole ratio and compare them with the predicted Mn/S ratios by i_{PEDOT} and i_{MnO_2}, which can be obtained by

$$(Mn/S)_{current} = \frac{i_{MnO_2}}{i_{PEDOT}} \quad (1)$$

As we can see, at 0.75 and 0.80 V, the $(Mn/S)_{current}$ matches very well with the $(Mn/S)_{EDS}$. At higher potentials the $(Mn/S)_{eds}$ is much lower than $(Mn/S)_{current}$, which is due to the overwhelming growth of PEDOT stated earlier. At lower pontetinals, $(Mn/S)_{current}$ is lower than $(Mn/S)_{EDS}$ due to the larger i_{PEDOT} than real current contributed from PEDOT growth during the coelectrodeposition of MnO_2/PEDOT stated earlier.

Pontential (V)	i_{PEDOT}	i_{MnO_2}	$i_{PEDOT} + i_{MnO_2}$	i_{co}	$(Mn/S)_{current}$	$(Mn/S)_{EDS}$
0.6	2	25	25	30	18	32
0.70	20	50	65	70	3.78	9
0.75	70	60	130	120	**1.29**	**1.05**
0.8	200	70	270	250	**0.53**	**0.43**
0.85	400	75	475	410	0.28	0.05
0.90	600	80	680	620	0.2	0.03
1.0	950	90	1010	980	0.14	0.01

Table 7.1. Steady currents for the potential static electrodeposition of single component of MnO_2 (i_{MnO_2}) and PEDOT (i_{PEDOT}) as well as the current for MnO_2/PEDOT coelectrodeposition (i_{co}) in the alumina template. $(Mn/S)_{current}$ the predicted mole ratio of MnO_2 to PEDOT based on i_{MnO_2} and i_{PEDOT} resulted from their electrodepositions. $(Mn/S)_{EDS}$ is experimental observed Mn/S mole ratio.

We further investigated the electrochemical performance of the MnO_2/PEDOT coaxial nanowires electrodeposited at different potential in order to find the optimized nanostructures for the electrochemical energy storage application. Figure 7.4 shows the CV graphs of the coaxial nanowires deposited at 0.65 V, 0.70 V, 0.75 V and 0.8 V. We divided the four CV curves into two groups (Group I is from 0.65V and 0.70V. Group II is from 0.75 V and 0.80 V) The capacitive current from Group I is

higher than Group II due to the more inclusion of MnO_2, which possesses higher specific capacitance than PEDOT. However the CV shape of Group II is more rectangular, suggesting the more capacitive behaviors of Group II due to the more incorporation of highly conductive PEDOT. However, if we carefully compare the CV curves from 0.65 V and 0.7 V, we can find that capacitive current from the 0.7 V is higher than that of 0.65 V. However, at even higher scan rate of 500 mV/s, the CV curve of 0.70 V and 0.65 V start to deviate a lot from the envelop shape, which is due to the low conductivity of MnO_2. At 0.75 V, the CV shape deviation is improved but can't be eliminated. But, the CV shape resulted from the coaxial nanowires electrodeposited at 0.8V is maintained square even at high scan rate of 500 mV/s, which is due to large amount of inclusion of PEDOT.

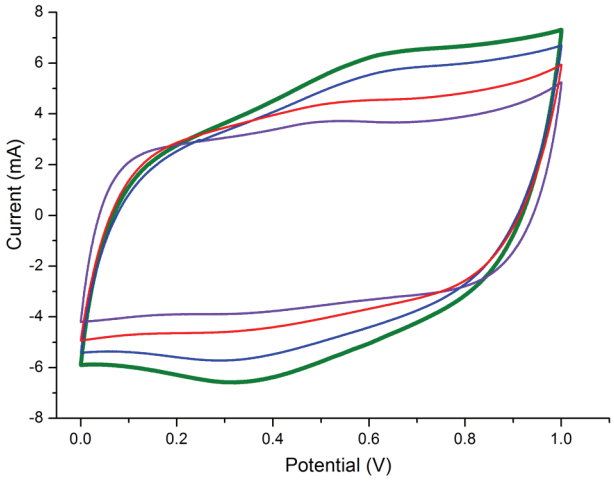

Figure 7.4. Cyclic voltammetry graphs of MnO_2/PEDOT coaxial nanowires coelectrodepsited at potentials of 0.65 V, 0.70 V, 0.75 V and 0.8 V obtained at 250 mV/s in the solution of 1 M $LiClO_4$ from 0-1 V.

Figure 7.5a showed the specific capacitance calculated from the CV graphs or galvanostatic charge discharge curves (data not shown) for the coaxial nanowires

deposited from 0.65V, 0.70 V, 0.75 V and 0.80V. Detailed calculation methods can be found in our previous paper. The specific capacitance of coaxial nanowire synthesized at 0.70 V is found to be the highest (270 F/g), which also explained the MnO_2/PEDOT nanowires synthesized at 0.70 V has highest capacitive current in Figure 7.4. Such high specific capacitance is due to the minimal usage of shell PEDOT materials, which can provide the high conductivities while not dragging down the high specific capacitance of MnO_2. At this potential, the PEDOT is deposited as thin shells, which can be seen in Figure 7.5b, the PEDOT nanotubes obtained after core MnO_2 etching is in Figure 7.5c.

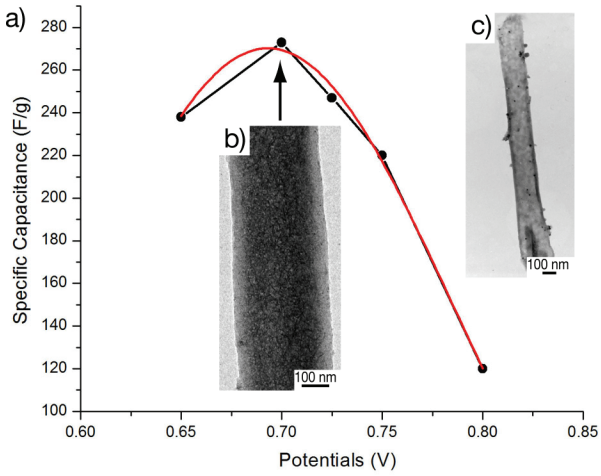

Figure 7.5. Specific capacitance calculated from the CV graphs or galvanostatic charge discharge curves for the MnO_2/PEDOT coaxial nanowires deposited from 0.65V, 0.70 V, 0.75 V and 0.80V.

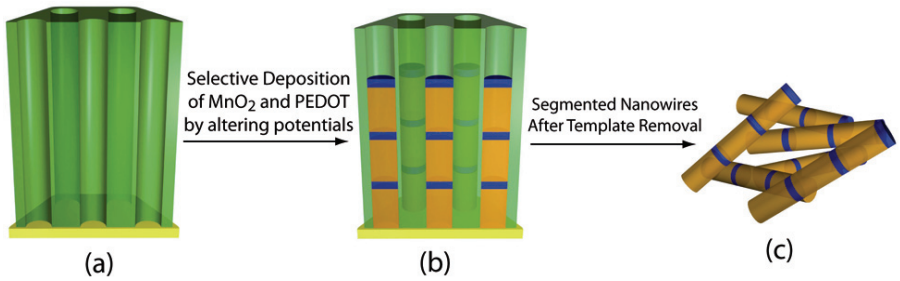

Scheme 7.2. Synthesis of segmented MnO_2/PEDOT nanowires via selective deposition of MnO_2 and PEDOT by applying alternative potentials.

The selective growth of MnO_2 and PEDOT at different potentials on the ring shape electrode suggest that segmented MnO_2/PEDOT nanowires can be fabricated if alternating potentials are applied during the electrodeposition, which is illustrated in Scheme 7.2. Such metal oxide/conductive polymer segmented nanowires is never reported before. When 0.6 V is applied, MnO_2 is selectively grown due to the lower onset potential of MnO_2[279,280]. When 0.9 V is applied, only PEDOT is electrodeposited because of the overwhelming growth of PEDOT mentioned earlier. Similar work has been done to electrodeposite segmented nanowires with two different metals (Cu/Co[281], Pt/Ni[282]) with different reduction potentials[164]. The more noble metal can be selectively deposited at a potential that is more positive than the reduction potential of the more active metal. The potential is then poised more negative to deposit the more active metal. However, at a more negative potential both of the metals will codeposit. The concentration of the second metal in the plating solution is made much higher than the more noble first metal in order to minimize the amount of noble metal deposited during deposition of the second metal. Similar problem is avoided in the deposition of MnO_2/PEDOT segmented nanowire because the PEDOT inhibits the growth of MnO_2 due to depletion of Mn^{2+} and mutual

expelling of MnO_2 and PEDOT. The length of the MnO_2 and PEDOT can be controlled by the charge during the electrodeposition. For example, the PEDOT segments in Figure 7.6b is controlled to be much shorter than the PEDOT segments in Figure 7.6a.

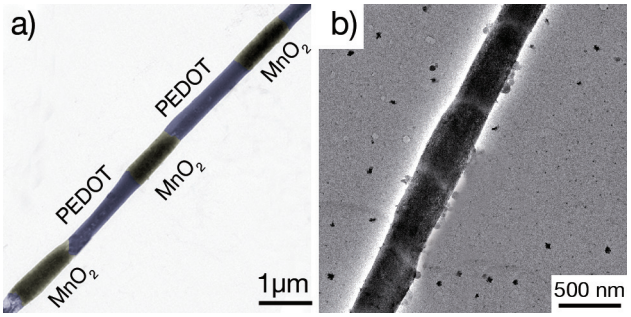

Figure 7.6. Segmented MnO_2/PEDOT nanowires electrodeposited applying alternative potentials in the single bath of manganese acetate (10 mM) and EDOT (80 mM). (a) PEDOT and MnO_2 segments are electrodeposited by the same charge densities of 250 mC/cm^2 at 0.6 V and 0.9 V. PEDOT (blue) and MnO_2 (brown) is colored manually by Photoshop for better visualization. (b) Same synthetic conditions as (a) except the PEDOT is electrodeposited at the charge densities of 50 mC/cm^2.

Finally, we have studied the coelectrodeposition of MnO_2 and PEDOT in the home-made template, which has smaller pore size (60 nm) than the commercial alumina membrane from whatman, inc. The coelectrodeposited MnO_2 and PEDOT in the home made template can be described as follows: Bottom electrodes from sputtered Au in the home-made template is relative flatter (less sharp edges) compared to the sputtered electrode from commercial membrane (it is much easier for the sputtered Au to fill up the small pore sized membrane, which render the electrodes rings

blunter). Consequently it is more difficult for the PEDOT to find sharp edges to get electrodeposited and PEDOT growth onset potential is shifted to higher potential, which is also observed on the flat top electrodes mention earlier. No PEDOT can be clearly identified below 0.80 V. While at 0.85 V, MnO_2/PEDOT coaxial nanowires is observed similarly to ones synthesized in the commercial large pore size membrane. Figure 7.7a. show the TEM image of MnO_2/PEDOT coaxial nanowire electrodeposited in the home-made template, darker core represents the MnO_2 while brighter shell represents the PEDOT. The elemental maps of Mn, S and mixed mpa of Mn and S also confirmed coaxial structures of MnO_2/PEDOT nanowires. The Mn and S elemental line scans profiles across the nanowire shows the precise position of MnO_2 and PEDOT on the nanowire.

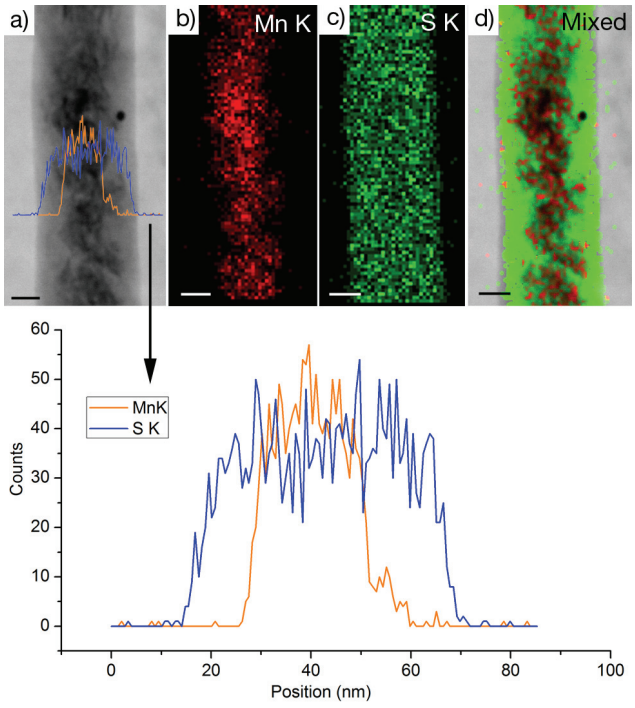

Figure 7.7. (a) TEM image of MnO_2/PEDOT coaxial nanowires in the home-made template (b) MnK (c) S K (d) mixed MnK and S K EDS mapping on the same coaxial nanowire. (e) MnK (orange) and S (blue) elemental EDS line scan profile across same coaxial nanowire in (a)

It is interesting to note the formation coaxial nanostructured of MnO_2/PEDOT is not uniform along the whole axis of the nanowire obtained from home made template. Instead, coaxial nanostructures are randomly found at different locations on the nanowires. This could be explained by the limited diffusion of EDOT monomer and Mn^{2+} in the small pore size membrane: when the EDOT starts to be depleted, the PEDOT is grown into the tubular like morphology. After most EDOT in the small channel is consumed, MnO_2 starts to be deposited in the PEDOT nanotubes to form a short coaxial MnO_2/PEDOT segment. However, the Mn^{2+} is quickly depleted due its more seriously limited diffusion; the EDOT monomer concentration is then recovered and starts over again to cover the previously grown MnO_2. Such alternation deposition is repeated by natures of alternative diffusion of MnO_2 and EDOT. It is more interesting to find the morphologies of the core MnO_2 also varied from different locations. Figure 7.8a showed a typical MnO_2/PEDOT coaxial nanowire coelectrodeposited in the home made template. Figure 7.8b and Figure 7.8d show the different morphologies of core MnO_2 on the same nanowire. Figure 7.8b shows the MnO_2 has formed into nanoparticles with sizes of 10-20 nm. The high resolution TEM clearly showed these nanoparticles have crystalline structures, which can be also proven in the electron diffraction pattern in Figure 7.8c. Figure 7.8d reveals the MnO_2 morphologies of the MnO_2 core at a different location on the nanowire, which

shows a typical fiber like morphologies observed before in the big pore size membrane. High resolution TEM shows no crystal structures can be found on these MnO_2 nanofibers, and no dots or rings can be found the electron diffraction pattern over this MnO_2 nanofibers area, which also suggest their amorphous nature.

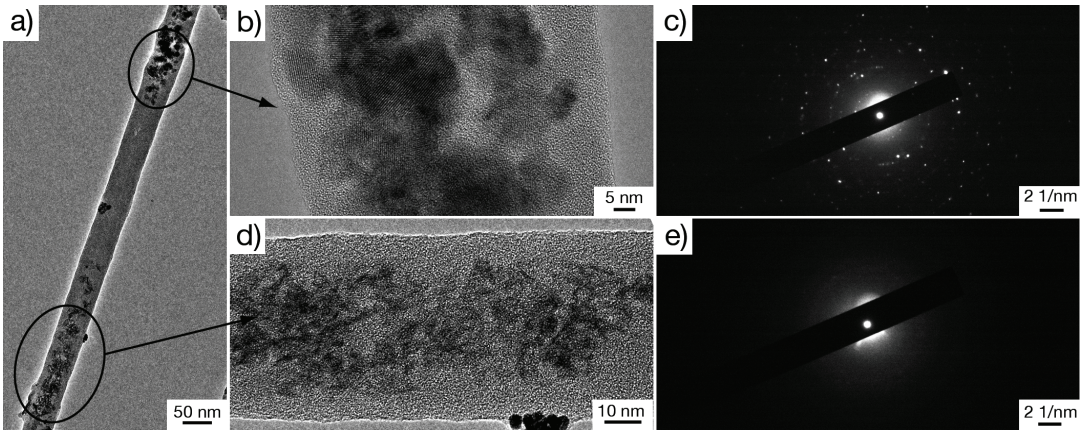

Figure 7.8. Heterogeneous structured MnO_2/PEDOT electrodeposited in home-made template (a) MnO_2/PEDOT coaxial nanostructures are randomly found at different locations on the nanowires (b) and (d) different morphologies of core MnO_2 on the same nanowire (c) and (e) corresponding electron diffraction patterns of core MnO_2 in (b) and (d)

7.4 Conclusion

The mechanism of coelectrodeposited coaxial MnO_2/PEDOT is studied in detail by performing the coelectrodeposition of MnO_2 and PEDOT on the sputtered nanoelectrodes with different shapes (ring and flat shapes) and different sizes (200 nm and 50 nm) in the alumina template channels. The sharp ring shape electrode is found to have crucial role to direct the growth of the PEDOT nanotube shells while

the flat top electrode is more favorable to the deposition of MnO_2. The growth of coaxial nanowires can be viewed as the parallel growth of core MnO_2 on the smooth inner surface and shell PEDOT on the sharp edges. 0.70 V is found to be the best condition to electrosynthesize MnO_2/PEDOT coaxial nanowires with optimized electrochemical performance, e.g. high specific capacitance of 270 F/g. The inclusion of PEDOT is found to increase the conductivity (high power) at the cost of losing energy density, while the inclusion of MnO_2 can boost the capacitance at the expense of losing conductivity (high power). Bar-coded MnO_2/PEDOT with different MnO_2 or PEDOT segment lengths can be fabricated by altering the potential for the electrochemical deposition. MnO_2 and PEDOT were found to be coelectrodeposited as short coaxial segments on nanowires in the small pore size membrane.

The mechanism of MnO_2/PEDOT coaxial nanowires offers fundamental understandings of one-step synthesis of heterogeneous one dimensional nanomaterials. Optimizing the composition and structures of high-power (high conductivity) and high-energy (high energy densities) materials at nanoscales are very important when utilizing them to build the heterostructured nanomaterials for the electrochemical energy.

Chapter 8. MnO_2-Nanoparticles Enriched Poly(3,4-ethylenedioxythiophene) Nanowires for Enhanced Electrochemical Energy Storage Capacity

8.1 Introduction

Hybrid nanomaterials are drawing a tremendous amount of attention in the nanoscience research field because not only do they offer extraordinary properties endowed by confining their dimensions but also they exhibit added synergic properties or functionalities arising from the combination of different materials[76,110,283-285]. There are a variety of ways to assemble the nanocomponents into hybrid nanomaterials. For example, layer by layer (LBL) assembly[284,286,287] has been widely used to create nanostructured composites on planar substrates[287] or to fabricate core-shell nanoparticles[284] and coaxial nanowires[110,286] with two layers or more by coating different materials onto existing nanostructured materials. Another straightforward and powerful method to fabricate hybrid nanomaterials is to disperse or assemble inorganic nanoparticles (e.g. metal[288] and magnetic nanocystals[289]) with small sizes into the matrices, voids and pores or onto the surfaces of nanostructured hosting materials (e.g. polymer nanowires, silica nanotubes). To date, hybrid nanomaterials with metal oxide and conductive polymer have been rarely reported[272]. In Chapter 6 and 7, we described the synthesis of coaxial MnO_2/PEDOT nanowires by one step coelectrodeposition method. In this chapter, we will present the loading of finely dispersed MnO_2 nanoparticles into PEDOT nanowires by simply soaking the PEDOT nanowires into a potassium permanganate solution. One of the advantages of

this synthetic method is that no additiontal steps are needed to prepare MnO_2 nanoparticles beforehand. MnO_2 nanoparticles are formed and simultaneously distributed in the pores of the PEDOT matrix triggered via the reduction of $KMnO_4$ by PEDOT. The loading amount and size of the MnO_2 nanoparticles can be controlled by varying the concentrations of $KMnO_4$ and the reaction time. Compared to the heterostructured MnO_2/PEDOT coaxial nanowires in our previous report, MnO_2 and PEDOT are more uniformly mixed in the hybrid nanowires, which enable the guest MnO_2 nanoparticles to have ultrahigh surface area so that they enhance the energy storage capacity (e.g. high specfic capacitance of 252 F/g) of the PEDOT furthermore but without causing excessive volume expansion of the PEDOT. The highly conductive and porous PEDOT matrix facilitates fast charge/discharge of the MnO_2 nanoparticles and prevents them from agglomerating. These combined properties enable the MnO_2 nanoparticle-enriched PEDOT nanowires, when applied as the electrode materials for supercapacitors or lithium ion batteries, to have boosted high energy densities even at high power densities.

8.2 Experimental Details

Chemicals and Materials. 3,4-Ethylenedioxythiophene (EDOT) was obtained from Aldrich (Milwaukee, WI). Lithium perchlorate, and potassium permanganate were obtained from Fisher Scientific (FairLawn, NJ). Acetonitrile and propylene carbonate were obtained from Sigma Aldrich. Gold electroplating solution (Orotemp 24) was purchased from Technic (Cranston, RI). Deionized water (ca. 18/ MΩ·cm resistivity) was obtained by using a Milli-Q water purification system from Millipore (Dubuque,

IA). Alumina membranes, with a pore diameter of 200 nm and thickness of 60 μm, are commercially available from Whatman (Clifton, NJ).

Synthesis. PEDOT nanowires were synthesized potentiostatically (1.2 V) in the acetonitrile solution of 100 mM EDOT, 100mM $LiClO_4$. All potentials were measured relative to an Ag/AgCl reference electrode using a Pt foil as a counter electrode, if not specified otherwise. Alumina template was subsequently removed by 3M NaOH solution to expose the PEDOT nanowires. MnO_2 nanoparticles were loaded into the PEDOT nanowires by soaking the above exposed PEDOT nanowires into potassium permanganate solution with different concentrations (5 mM-50 mM), depending on the desiring amount of MnO_2 nanoparticles that need to be loaded. Gold bottoms for the volume expansion studies were electrochemically deposited at the current density of -1 mA/cm^2 for 30 mins in the Orotemp 24 gold plating solution. The preparation of a working electrode is as follows: First, a thin layer of gold (ca. 500 nm) was sputtered onto the branched side of an alumina membrane by using a sputtering system (Denton Vacuum Desktop III). The Au-coated membrane was connected to an electrical circuit using a copper tape (3M). Defining and sealing an electroactive window (0.32 cm^2 in nominal area) was performed using silicone rubber or parafilm. Considering the porosity of the membrane (60 %), the corrected surface area of the electroactive window was 0.2 cm^2. The mass and the length (thickness in film) of the resulting PEDOT nanowires, was controlled by fixing the total charges passed during the electrodeposition. Typically coaxial nanowires with lengths of 10 μm can be obtained after the charge passed about 200 mC. Diameters of these nanowires are corresponded to the pore diameters of alumina template (ca. 300 nm).

Characterizations. The MnO_2-NP/PEDOT nanowires were investigated using a field-emission scanning electron microscope (Hitachi SU-70 SEM, operated at an acceleration voltage of 10 keV) and transmission electron microscope (JEOL JEM 2100 Field Emission Transmission Electron Microscope (FE-TEM), 200 keV). The sampling methods for SEM and TEM analysis are briefly described: gold-coated side of a small piece of an alumina template was tightly attached onto an SEM specimen holder by using a carbon tape. The template was dissolved to expose the nanowires by using 3 M NaOH. After rinsing it with de-ionized water repeatedly, the sample was dried in air before observation. For TEM sampling, sonication is applied to the MnO_2-NP/PEDOT to disperse them in ethanol. The released nanowires were repeatedly rinsed with de-ionized water and ethanol. Then, 6 μL of the nanowire solution was dropped and dried on a TEM grid.

In order to calculate specific capacitance, cyclic voltammetry at different scan rates (100-500 mV/s) and galvanostatic charge/discharge tests at different current densities (10-50 mA/cm^2) were performed by cycling potential from 0 to 1 V in 1 M $LiClO_4$ in water. Galvanostatic charge/discharge for the lithium ion battery study is done by cycling the potential from 0 to 1V at current density of 1.25 mA/cm^2 (corresponds to about 10 C charge/discharge rate for MnO_2-NP/EPDOT nanowires) in the solution of 1 M $LiClO_4$ in the propylene carbonate. All the above electrochemical experiments were performed using a bi-potentiostat (BI-STAT; Princeton Applied Research).

8.3 Results and Discussion

Scheme 1 illustrates the synthesis of MnO_2 nanoparticle-loaded PEDOT nanowires, which will be abbreviated as MnO_2-NP/PEDOT nanowires. PEDOT nanowires were first electrodeposited in an alumina template and then exposed by template removal. The freestanding PEDOT nanowires were subsequently soaked in potassium permanganate solution (typically 10 mM) for various times (typical 10min). MnO_2 nanoparticles were grown into the PEDOT matrix during this soaking process. The color of the PEDOT nanowires turned from navy blue into a greenish color due to mixing with the brownish colored MnO_2-NP. Soaking PEDOT nanowires in higher concentrations of $KMnO_4$ or at longer times will result in etching of PEDOT (discussed later), which renders the PEDOT nanowires brownish in color. It is worth noting that the thus formed MnO_2 nanoparticles can be etched off by dilute sulfric acid, which causes the PEDOT nanowires to return to their bluish color. (See Figure 8.1).

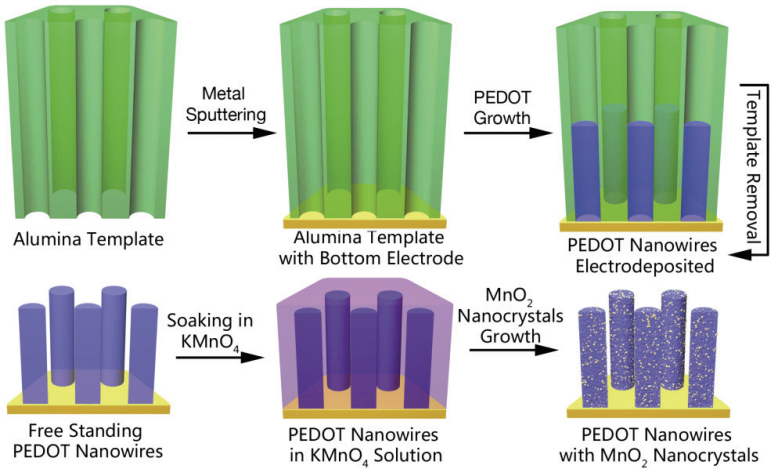

Scheme 8.1. Synthesis of MnO_2-NP/PEDOT Composite Nanowires

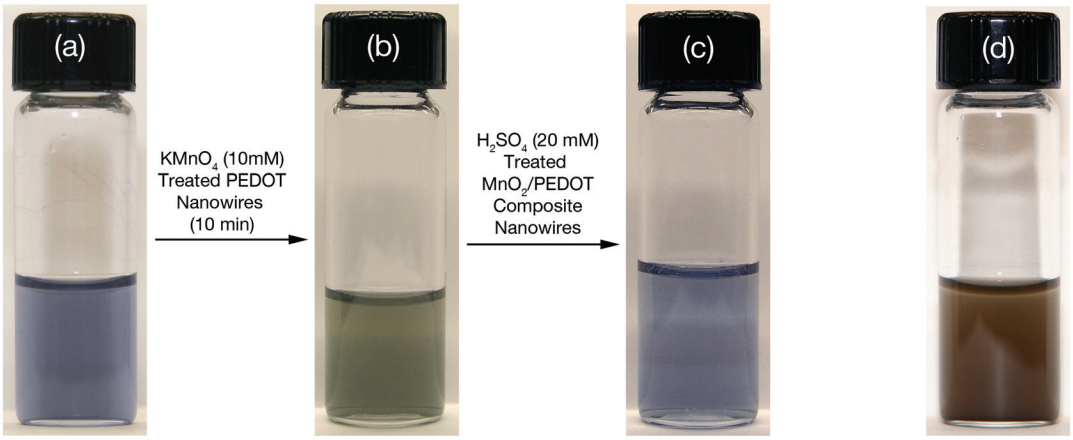

Figure 8.1. Digital images of (a) PEDOT nanowires dispersed in ethanol (b) MnO_2-NP/PEDOT nanowires in ethanol (c) Sulfuric acid treated MnO_2-NP/PEDOT nanowires, MnO_2 is striped off (d) overoxidized PEDOT nanowires after soaking PEDOT nanowires in 10 mM $KMnO_4$ for 30 min

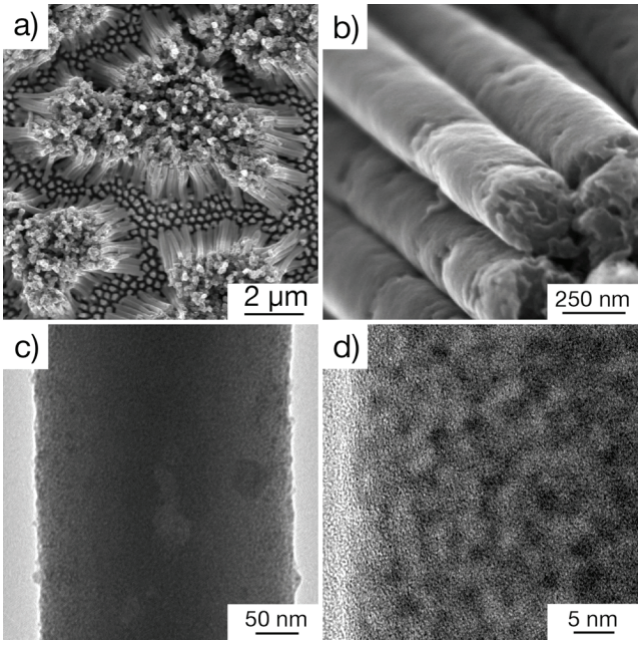

Figure 8.2. (a,b) SEM and (c,d) TEM images of PEDOT nanowires after being treated with $KMnO_4$ (10 mM) for 10 min at different magnifications.

The SEM image (Figure 8.2a) of the $KMnO_4$ treated PEDOT nanowires shows that they have aggregated into piles driven by the surface tension during solvent evaporation. To prevent this aggregation problem from affecting the electrochemical testing, the electrode should be prevented from completely drying. Figure 8.2b shows the high resolution SEM image of the same nanowires, which reveals their cigar shapes and rough surfaces. Figure 8.2c is the TEM image from a segment of $KMnO_4$ treated PEDOT nanowire. Some dark nanoparticles can be vaguely seen, which can be further observed more clearly using a higher resolution TEM image (Figure 8.2d.) These nanoparticles are found be to less than 5 nm and finely dispersed in the PEDOT matrix. XRD studies shows that these nanoparticles are X-ray amorphours, however, under TEM, they show some weak crystalline structures, which may be introduced by the annealing caused by the heating TEM electron beams. The lattice spaces and electron diffraction ring patterns only partly match the XRD indices of α-MnO_2. Alternative methods are used to analyse these $KMnO_4$ treated nanowire in order to confirm the existance of MnO_2. Figure 8.3 a-d show the TEM images, Mn K map, S K map, and their mixed map on a segment of MnO_2-NP/PEDOT nanowire. Figure 8.3e showed the EDS spectra from a single MnO_2-NP PEDOT nanowire. Quantitative information show that the atomic ratio of Mn to S is 1.42:1, which suggests that a large amount of MnO_2-NP have been loaded into the PEDOT matrix.

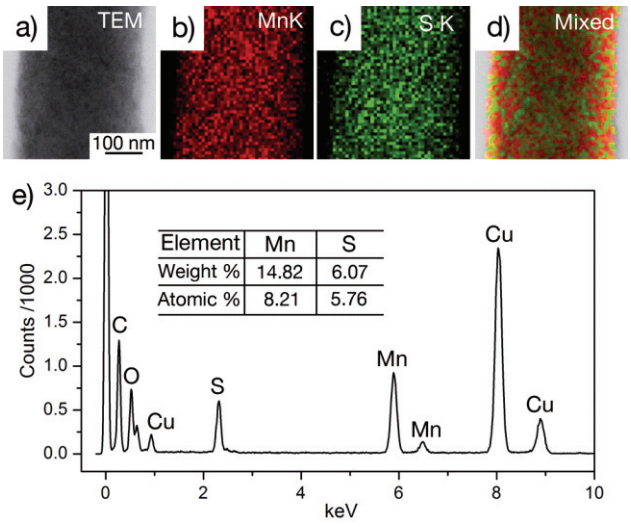

Figure 8.3. (a) TEM image and EDS mapping of (b) Mn, (c) (S), and (d) mixture of Mn and S on a segment of MnO_2-NP/PEDOT nanowires

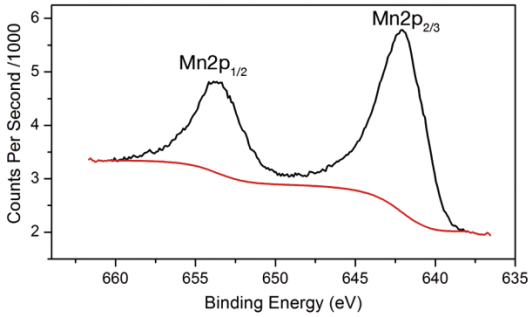

Figure 8.4. XPS spectra for manganese in the $KMnO_4$ treated PEDOT nanowires

Figure 8.4 show the XPS spectra obtained from the MnO_2-NP loaded PEDOT nanowires, the peaks of Mn $2p_{3/2}$, Mn $2p_{1/2}$ which are centered at 642 and 653.8 eV, respectively, with a spin-energy separation of 11.8 eV are in good agreement with reported data of Mn $2p_{3/2}$ and Mn $2p_{1/2}$ in MnO_2[81].

The mechanism of MnO_2 formation is not completely understood at this point but a few plausible mechanisms are proposed and discussed. Based on the Mn/S ratio

shown in Figure 8.3e, we can assume that 1 mole of PEDOT can encapsulate c.a. 1.4 moles of MnO_2-NP. This process requires 4.2 moles of electrons to reduce the 1.4 moles of $KMnO_4$. However, it is difficult to conceive that 1 mole of PEDOT can provide 4.2 moles of electrons because the PEDOT is the already oxidized form of EDOT. The maximum electrons it can provide are based on its doping level, which is 0.3[290]. This suggests one mole of PEDOT can only provide 0.3 moles of delocalized electrons during the doping (oxidation) process, which is not enough to reduce 1.4 moles of $KMnO_4$.

By looking at the structure of PEDOT, one would find that there are unsaturated bonds on the PEDOT conjugated rings, which might be broken and oxidized by the $KMnO_4$. If this is true, this oxidation will destroy the conjugation of PEDOT and the PEDOT will lose its conductivity and electroactivity. However, our experimental test has ruled out this possibility: After the MnO_2-NP are loaded in the PEDOT matrix, dilute sulfuric acid is applied to the hybrid nanowires to strip off the MnO_2. Electrochemical tests were performed on these MnO_2-striped PEDOT nanowires and they showed that the electrochemical properties were retained (data not shown) when compared to the electrochemical properties of PEDOT nanowires before MnO_2-NP insertion.

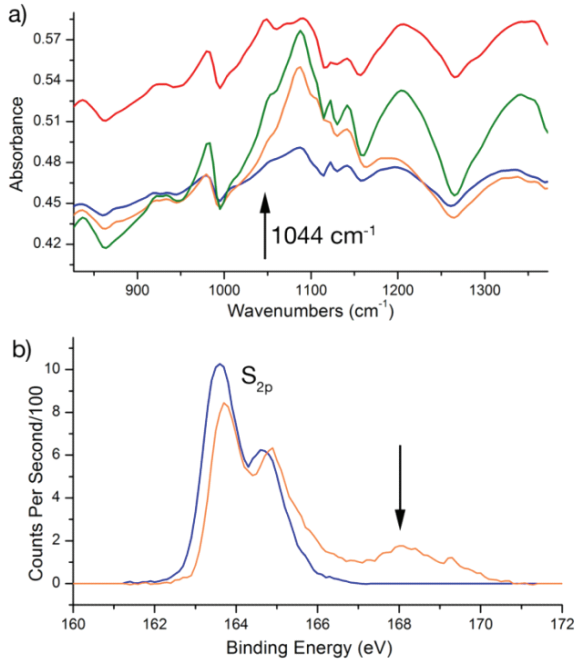

Figure 8.5. (a) IR spectra of PEDOT nanowire (blue) and PEDOT nanowires treated with 10 mM (orange), 20 mM (green) and 50 mM (red) $KMnO_4$ for 10 min. An absorbance peak at 1044 cm^{-1} graduately appears as the concentration of $KMnO_4$ increases and can be identified clearly when the $KMnO_4$ concentration has reached 50 mM. (b) XPS spectra of PEDOT before (blue) and after treatment with $KMnO_4$ (orange). The Sulphur peak has slightly shifted to the higher binding energy, which suggests the sulfur has been oxidized. Also a small new peak at higher binding energy of 168 eV has appeared.

Based on the above analysis, the mechanism of MnO_2 NP formation becomes more ambiguous. However, when we take a glance at the EDOT monomer structure, it is not hard to find that the sulphur on the thiophene ring may serve as the reductive site for the $KMnO_4$ reduction. Indeed, MnO_2 nanoparticles have been synthesized previously via the $KMnO_4$ reduction by nitrogen sites on the aniline monomers[291].

Figure 8.5a show the IR spectra of PEDOT nanowires treated with different concentration of $KMnO_4$ for 10 min. The arising peak at 1044 cm^{-1} can be assigned to the sulphoxide (S=O bond) stretching mode[292], which suggests possible oxidation of the thiophene sulphur into sulphoxide by $KMnO_4$. The new peak (168 eV) in XPS analysis (Figure 8.5b) alludes to the possible oxidation of thiophene sulphur into the sulphone O=S=O group[293]. Similar oxidation on the sulphur sites of PEDOT:PSS by hydrogen peroxide[294] or NaOCl[295] and have been described elsewhere. Oxidation of sulphides to corresponding sulphones by $KMnO_4$ is also reported. In order to prevent the PEDOT from losing its electroactivity, the concentration of $KMnO_4$ and the soaking time have to be kept low and short so that only a small portion of the PEDOT is oxidized. It is worth noting that only partial oxidation of thiophene sulphur sites on PEDOT will not be able to provide enough electrons for the $KMnO_4$ reduction ratio of 1.4 times of MnO_2 to PEDOT. However, such reduction reactions can form the initial seeds which may accelerate the natural reduction of $KMnO_4$ into MnO_2 and further grow theMnO_2 nanoparticles.

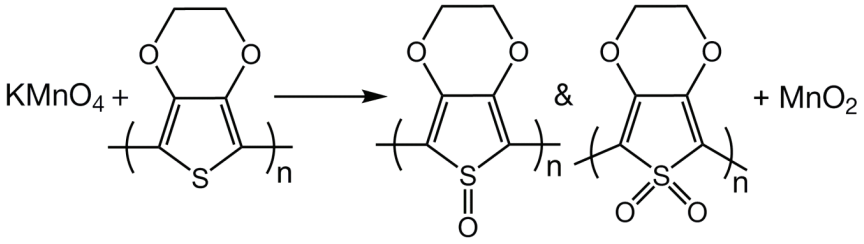

Scheme 8.2. Reduction of $KMnO_4$ by PEDOT to form MnO_2

By controlling the soaking time and the concentration of the $KMnO_4$, we can regulate the loading amount of MnO_2. Figure 8.6a shows the Mn/S ratio determined by EDS analysis after the PEDOT nanowires reacted with different concentrations of $KMnO_4$ for 1 min. It is worth of noting that the MnO_2 loading increases more rapidly

at higher concentration of $KMnO_4$, which could be caused by the complete etching away of PEDOT after it is overoxidized into soluble product. Figure 8.6b shows how the Mn/S ratio responds to the soaking time more linearly.

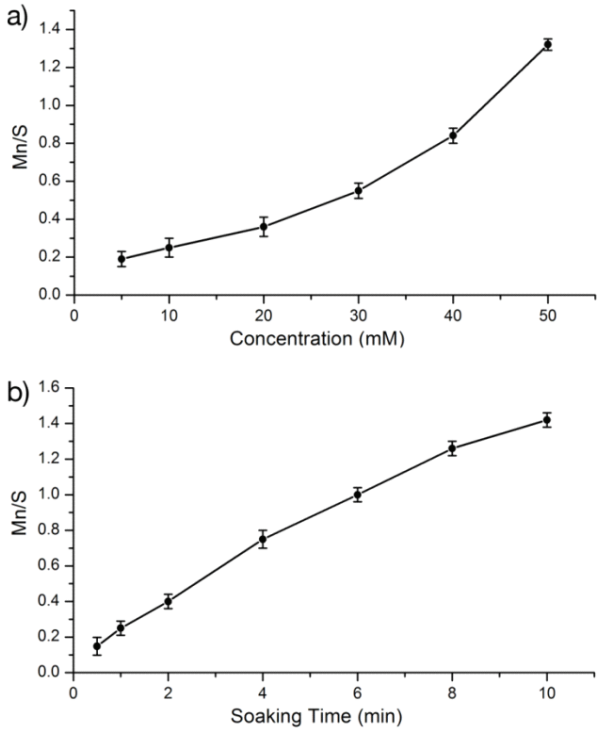

Figure 8.6. MnO_2 loading capacity (Mn/S ratio) versus (a) different concentrations of $KMnO_4$ for 1 min and (b) different soaking times in 10 mM $KMnO_4$.

It is interesting to note that not only can the loading amount of MnO_2 be varied but also the nanoparticle size and structure can be tuned when different concentrations of $KMnO_4$ or different soaking times are applied.

In order to study the electrochemical energy storage benefits of loading MnO_2 into the PEDOT matrix , cyclic voltammetry (CV) (Figure 8.7a) and galvanostatic charge/discharge (Figure 8.7b) tests were performed on the PEDOT nanowires before

and after $KMnO_4$ treament. Both galvanostatic charge/discharge (Figure 8.8) and CV methods are used to calculate the specific capacitance of MnO_2-NP/PEDOT nanowires and evaluate their energy density and power density Thus the calculated specfic capacitance MnO_2-NP/PEDOT nanowires is 250 F/g, which is higher than our previous reported MnO_2/PEDOT coaxial nanowires. 80% percent of the high energy density 8 Wh/kg is maintained while the power densities is boosted over 20 kW/kg.The well-maintained energy density is due to small dimensions of the PEDOT nanowires and MnO_2 NP as well as as the high conductivity of PEDOT. Due to the large specific surface area of MnO_2 NP, the pristine specific capacitance of MnO_2 NP can be calculated as 410 F/g, which is higher than other synthesized nanostructured MnO_2 supercapacitor electrodes at the same charge/discharge rate[296,297]. Figure 8.7b also demonstrates that the MnO_2-NP/PEDOT can serve as promising electrode materials for lithium ion batteries. Indeed, nanostructured MnO_2 or PEDOT have been respectively reported for applications in lithium ion batteries[298,299].

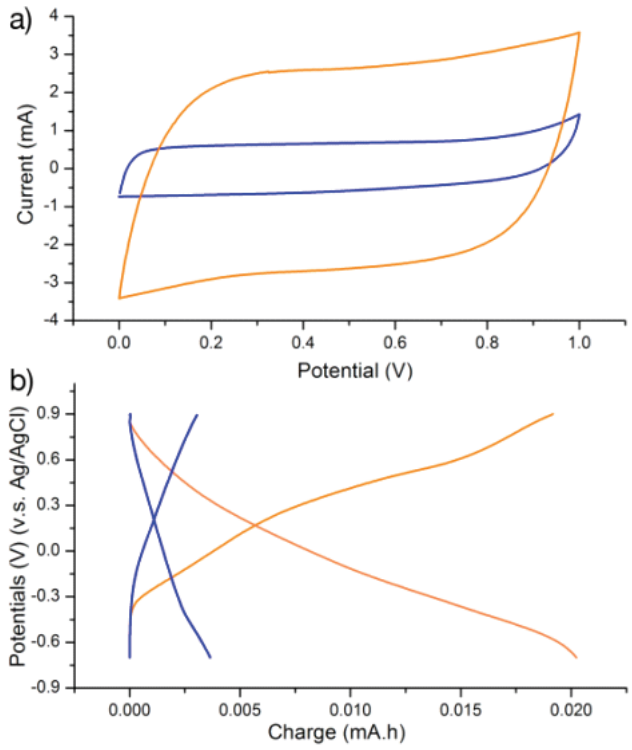

Figure 8.7. (a) Cyclic Voltamograms of PEDOT nanowires before (blue) and after (orange)10 mM $KMnO_4$ treatment (10 min) scanned at 100 mV/s between 0-1 V in 1 M $LiClO_4$ in water. The inclusion of MnO_2 nanoparticles has resulted in the capacitive current increasing fourfold (b) galvanostatic charge/discharge curves of PEDOT nanowires (blue) and MnO_2-NP/PEDOT nanowires (orange) at current density of 1.25 mA/cm^2 in 1 M $LiClO_4$ in propylene carbonate,which corresponds to the 10 C high charge/discharge rate. It shows that the charge capacity significantly increased at least 4 times after loading of MnO_2 nanoparticles.

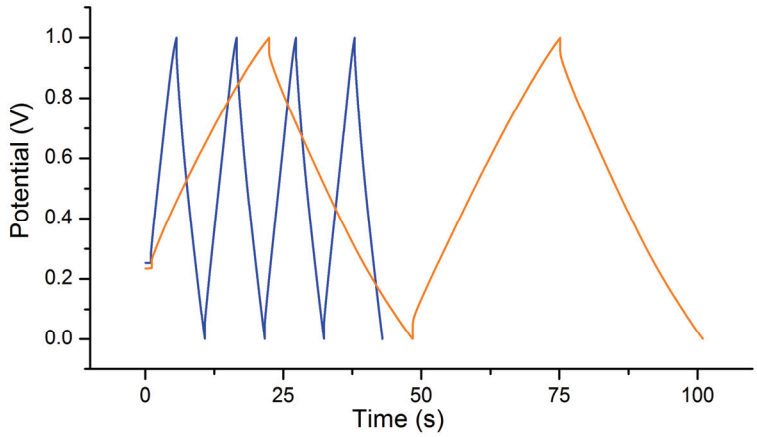

Figure 8.8. Galvanostatic charge/discharge curves for PEDOT nanowires (blue) and PEDOT nanowires after loading MnO_2 nanoparticles (orange)

It is worth noting that although the inclusion of MnO_2 NP significantly increases the charge capacity of PEDOT nanowires, the volume of the PEDOT is not expanded significantly. Figure 8.9 shows the TEM images of PEDOT nanowires (grown on Au bottom) before and after the $KMnO_4$ treatment. Assuming the diameter of the bottom gold is not affected by the $KMnO_4$, and the PEDOT nanowire swelling is isotropic, the volume expansion rate can calculated as:

$$\frac{V_2 - V_1}{V_1} = \left(\frac{d_{MnO_2/PEDOT} / d_{Au-MnO_2/PEDOT}}{d_{PEDOT} / d_{Au-PEDOT}} - 1 \right)^3 \tag{8.1}$$

Thus calculated volume expansion rate is 25%. Compared to MnO_2/PEDOT coaxial nanowires in our previous report, the incorporated MnO_2 utilizes less space while

providing more energy capacity,which further increases the energy density and power density per volume.

Volume expansion of PEDOT nanowire can also be theoretically estimated by the following equation:

$$\frac{V_2 - V_1}{V_1} = \frac{n_2}{n_1}\frac{d_1 M_2}{d_2 M_1} \qquad (2)$$

Where n_2/n_1 is the mole ratio of the MnO_2 to PEDOT (here-in 1.42), d_2, d_1 are the density of MnO_2 and PEDOT[300], M_2 and M_1 is the molecular weights of MnO_2 and PEDOT. Based on equation (8.2) the volume expansion is estimated as 28%, which well matches the experimental obtained volume expansion rate.

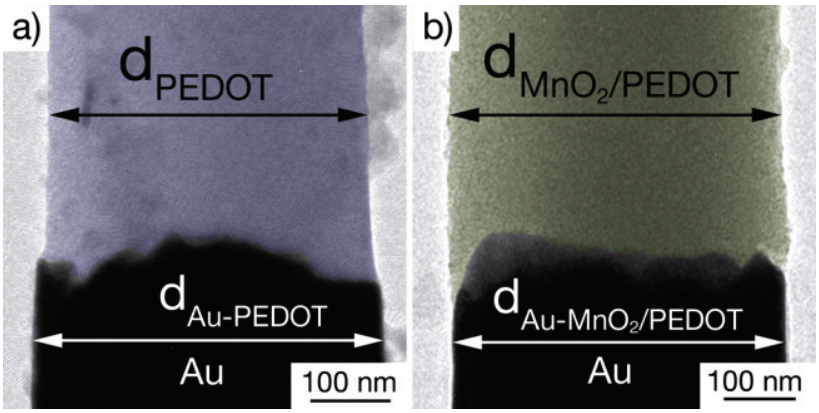

Figure 8.9. Volume expansion of PEDOT nanowires before and after loading of MnO_2-NP. (PEDOT nanowires are treated in 10 mM $KMnO_4$ for 10 min) d_{PEDOT} and $d_{MnO2/PEDOT}$ represent the diameters of the PEDOT nanowire before and after $KMnO_4$ treatment, $d_{Au/PEDOT}$ and $d_{Au\text{-}MnO2/PEDOT}$ represent diameters of the their corresponding gold bottom. The diameter expansion of the MnO_2-NP/PEDOT nanowires is less than 8%, which is easily accommodated by the available spaces between the PEDOT

nanowires after template removal. The small volume expansion is mainly due to the low volumetric mass density of PEDOT matrix (provides spaces to include large amount of MnO_2).

8.4 Conclusion

In summary, we described the fabrication of MnO_2 nanoparticle-loaded PEDOT nanowires by simply soaking the PEDOT nanowires in $KMnO_4$ solution. The formation of MnO_2 nanoparticles is triggered via the $KMnO_4$ reduction by the sulfur sites on thiophene rings. The MnO_2 nanoparticles boost the energy storage capacity by 4 times while only causing the PEDOT volume to expand 25%. The hosting material, highly conductive and porous PEDOT, facilitates the fast charge/discharge rate of the MnO_2 nanoparticles and prevents them from aggregation. These synergic properties enable the MnO_2-NP enriched PEDOT nanowires to be promising electrode materials with high energy densities and high power densities for supercapacitors and lithium ion batteries, which pave the way for the investigation of other types of hybrid nanomaterials for applications in electrochemical energy storage.

Chapter 9. Summary and Outlook

9.1 Summary

Template synthesized nanomaterials such as nanowires, nanotubes, and coaxial nanowries have been successfully in electrochemical energy storage systems such as supercapacitors and lithium ion batteries for enhancing their charge/discharge rates, energy densities and power densities, etc. Template synthesis of nanomaterials and alumina template fabrication has been decribed in details in concepts as well as in experimental aspects. Four examples of using template synthesized nanomaterials in electrochemical energy storage are given. The first one is utilizing poly(3,4-ethylenedioxythiophene) (PEDOT) nanotubes as electrode materials for high-powered supercapacitor. The thin-walled nanotubes allow fast charge/discharge of the PEDOT to achieve high power. The second one is related to synthesis and characterization of RuO_2/PEDOT composite nanotubes for supercapacitors. Loading appropriate amount of RuO_2 can effectively enhance the specific capacitance of PEDOT nanotube. The third case illustrates the synthesis of MnO_2/PEDOT coaxial nanowires by one step coelectrodeposition for electrochemical energy storage. The combined properties of MnO_2 and PEDOT enable the coaxial nanowires to have very high specific capacitances at high current densities. Their formation mechanism are explored and their nanostructures are tuned for optimized electrochemical properties. The final case reports the MnO_2-Nanoparticles enriched PEDOT nanowires for enhanced electrochemical energy storage capacity. Large amount of the MnO_2 nanoparticles can be loaded into PEDOT nanowires after they are soaked in $KMnO_4$

solution. Thus loaded MnO_2 nanoparticles effective enhance the energy densities of PEDOT nanowires without causing too much volume expansion to them.

9.2 Outlook

The present study can be extended into a few directions. For example, different materials can be combined into heterstructured nanomaterials. Metal oxides such as CoO_2 and V_2O_5 can be combined with different conductive polymers such as polypyrrole, polyaniline can be coelectrodeposited into alumina template. Thus formed nanowires can be investigated for their detailed nanostructures and electrochemical properties. The coaxial nanowires can also be applied into lithium ion battery if proper materials are chosen as the shell materials and core materials, for example, graphitic carbon and $LiFePO_4$. Segmented nanowires of MnO_2/PEDOT can be further investigated for fabricating peridioc PEDOT nanocapsules by etching of the core MnO_2. Fundamentals studies such as investigating the electrochemical properties on a single nanotube, nanowires, or coaxial nanowires are also required to further understand the advantages of using one dimensional nanomaterials in the applications of energy storage. Another important study can be performed on the investigation of thin coated nanomaterials on the 3-D nano-architectured electrodes suchs 1-D arrays of carbon nanotubes, metal nanowires for the applications of supercapacitors. Because the faradic reaction only occur within a few nanometers from the surface of the electrode materials for the pseudo-type supercapacitor at fast charge/discharge rate, coating a thin layer of nanomaterials on the 3-D nano-architectured electrodes may result in the much higher utilization of materials during

the charge/discharge process, which may lead to the breakthrough of enhancement of specific capacitance and specific power.

Publications:

The Chapter 4 in this thesis has been published in

Nanotechnology, **2008**, *19*, 215710

The Chapter 5 in this thesis has been publised in

J. Am. Chem. Soc. **2008**, *130*, 2942-2943

Reference

(1) Romm, J. *Energy Policy* **2006**, *34*, 2609-2614.
(2) Service, R. F. *Science* **2006**, *313*, 902-902.
(3) Brodd, R. J.; Bullock, K. R.; Leising, R. A.; Middaugh, R. L.; Miller, J. R.; Takeuchi, E. *J. Electrochem. Soc.* **2004**, *151*, K1-K11.
(4) Armand, M.; Tarascon, J. M. *Nature* **2008**, *451*, 652-657.
(5) Armand, M.; Johansson, P.; Elsevier Science Bv: 2008, p 821-825.
(6) Miller, J. R.; Simon, P. *Science* **2008**, *321*, 651-652.
(7) Conway, B. E. *Electrochemical Supercapacitors: Scientific Fundamentals and Technological Applications*; Plenum Publishing Co.Ltd., 1999.
(8) Pandolfo, A. G.; Hollenkamp, A. F. *J. Power Sources* **2006**, *157*, 11-27.
(9) Frackowiak, E.; Metenier, K.; Bertagna, V.; Beguin, F. *Appl. Phys. Lett.* **2000**, *77*, 2421-2423.
(10) Frackowiak, E.; Beguin, F. *Carbon* **2001**, *39*, 937-950.
(11) Vix-Guterl, C.; Frackowiak, E.; Jurewicz, K.; Friebe, M.; Parmentier, J.; Beguin, F. *Carbon* **2005**, *43*, 1293-1302.
(12) Yoon, B. J.; Jeong, S. H.; Lee, K. H.; Kim, H. S.; Park, C. G.; Han, J. H. *Chem. Phys. Lett.* **2004**, *388*, 170-174.
(13) Fuertes, A. B.; Lota, G.; Centeno, T. A.; Frackowiak, E. *Electrochim. Acta* **2005**, *50*, 2799-2805.
(14) Wu, N. L. 2002, p 6-11.
(15) Conway, B. E. *J. Electrochem. Soc.* **1991**, *138*, 1539-1548.
(16) Raymundo-Pinero, E.; Khomenko, V.; Frackowiak, E.; Beguin, F. *J. Electrochem. Soc.* **2005**, *152*, A229-A235.
(17) Mastragostino, M.; Arbizzani, C.; Soavi, F. 2002, p 493-498.
(18) Arbizzani, C.; Mastragostino, M.; Meneghello, L. *Electrochim. Acta* **1996**, *41*, 21-26.
(19) Khomenko, V.; Frackowiak, E.; Beguin, F. *Electrochim. Acta* **2005**, *50*, 2499-2506.
(20) Ryu, K. S.; Kim, K. M.; Park, N. G.; Park, Y. J.; Chang, S. H. *J. Power Sources* **2002**, *103*, 305-309.
(21) Kotz, R.; Carlen, M. *Electrochim. Acta* **2000**, *45*, 2483-2498.
(22) Grahame, D. C. *Chem. Rev.* **1947**, *41*, 441-501.
(23) Zheng, J. P. *Electrochemical and Solid State Letters* **1999**, *2*, 359-361.
(24) Zheng, J. P.; Cygan, P. J.; Jow, T. R. *J. Electrochem. Soc.* **1995**, *142*, 2699-2703.
(25) Cottineau, T.; Toupin, M.; Delahaye, T.; Brousse, T.; Belanger, D. *Applied Physics a-Materials Science & Processing* **2006**, *82*, 599-606.
(26) Wang, S. Y.; Ho, K. C.; Kuo, S. L.; Wu, N. L. *J. Electrochem. Soc.* **2006**, *153*, A75-A80.
(27) Toupin, M.; Brousse, T.; Belanger, D. *Chem. Mater.* **2002**, *14*, 3946-3952.
(28) Hu, C. C.; Tsou, T. W. *Electrochem. Commun.* **2002**, *4*, 105-109.
(29) Jiang, J. H.; Kucernak, A. *Electrochim. Acta* **2002**, *47*, 2381-2386.
(30) Xiao, Q. F.; Zhou, X. *Electrochim. Acta* **2003**, *48*, 575-580.
(31) Frackowiak, E.; Khomenko, V.; Jurewicz, K.; Lota, K.; Beguin, F. 2006, p 413-418.

(32) Fusalba, F.; Gouerec, P.; Villers, D.; Belanger, D. *J. Electrochem. Soc.* **2001**, *148*, A1-A6.
(33) An, K. H.; Jeon, K. K.; Heo, J. K.; Lim, S. C.; Bae, D. J.; Lee, Y. H. *J. Electrochem. Soc.* **2002**, *149*, A1058-A1062.
(34) Laforgue, A.; Simon, P.; Sarrazin, C.; Fauvarque, J. F. 1999, p 142-148.
(35) Fonseca, C. P.; Benedetti, J. E.; Neves, S. *J. Power Sources* **2006**, *158*, 789-794.
(36) Choi, D.; Blomgren, G. E.; Kumta, P. N. *Adv. Mater.* **2006**, *18*, 1178-+.
(37) Machida, K.; Furuuchi, K.; Min, M.; Naoi, K. *Electrochemistry* **2004**, *72*, 402-404.
(38) Toupin, M.; Brousse, T.; Belanger, D. *Chem. Mater.* **2004**, *16*, 3184-3190.
(39) Sugimoto, W.; Iwata, H.; Yasunaga, Y.; Murakami, Y.; Takasu, Y. *Angew. Chem.-Int. Edit.* **2003**, *42*, 4092-4096.
(40) Miller, J. M.; Dunn, B.; Tran, T. D.; Pekala, R. W. *J. Electrochem. Soc.* **1997**, *144*, L309-L311.
(41) Wang, Y.; Takahashi, K.; Lee, K.; Cao, G. Z. *Adv. Funct. Mater.* **2006**, *16*, 1133-1144.
(42) Hu, C. C.; Chang, K. H.; Lin, M. C.; Wu, Y. T. *Nano Lett.* **2006**, *6*, 2690-2695.
(43) Liu, R.; Il Cho, S.; Lee, S. B. *Nanotechnology* **2008**, *19*, 8.
(44) Guo, Y. G.; Hu, J. S.; Wan, L. J. *Adv. Mater.* **2008**, *20*, 2878-2887.
(45) Wang, Y.; Cao, G. Z. *Adv. Mater.* **2008**, *20*, 2251-2269.
(46) Bruce, P. G.; Scrosati, B.; Tarascon, J. M. *Angew. Chem., Int. Ed.* **2008**, *47*, 2930-2946.
(47) Arico, A. S.; Bruce, P.; Scrosati, B.; Tarascon, J. M.; Van Schalkwijk, W. *Nat. Mater.* **2005**, *4*, 366-377.
(48) Okubo, M.; Hosono, E.; Kim, J.; Enomoto, M.; Kojima, N.; Kudo, T.; Zhou, H. S.; Honma, I. *J. Am. Chem. Soc.* **2007**, *129*, 7444-7452.
(49) Chen, J.; Xu, L. N.; Li, W. Y.; Gou, X. L. *Adv. Mater.* **2005**, *17*, 582-+.
(50) Gao, X. P.; Bao, J. L.; Pan, G. L.; Zhu, H. Y.; Huang, P. X.; Wu, F.; Song, D. Y. *J. Phys. Chem. B* **2004**, *108*, 5547-5551.
(51) Chan, C. K.; Peng, H. L.; Liu, G.; McIlwrath, K.; Zhang, X. F.; Huggins, R. A.; Cui, Y. *Nat. Nanotechnol.* **2008**, *3*, 31-35.
(52) Robertson, A. D.; Armstrong, A. R.; Bruce, P. G. *Chem. Mater.* **2001**, *13*, 2380-2386.
(53) Poizot, P.; Laruelle, S.; Grugeon, S.; Dupont, L.; Tarascon, J. M. *Nature* **2000**, *407*, 496-499.
(54) Pereira, N.; Dupont, L.; Tarascon, J. M.; Klein, L. C.; Amatucci, G. G. *J. Electrochem. Soc.* **2003**, *150*, A1273-A1280.
(55) Li, H.; Balaya, P.; Maier, J. *J. Electrochem. Soc.* **2004**, *151*, A1878-A1885.
(56) Li, H.; Shi, L. H.; Wang, Q.; Chen, L. Q.; Huang, X. J.; Elsevier Science Bv: 2002, p 247-258.
(57) Fong, R.; Vonsacken, U.; Dahn, J. R. *J. Electrochem. Soc.* **1990**, *137*, 2009-2013.
(58) Huang, H.; Yin, S. C.; Nazar, L. F. *Electrochemical and Solid State Letters* **2001**, *4*, A170-A172.
(59) Yang, J.; Winter, M.; Besenhard, J. O. *Solid State Ionics* **1996**, *90*, 281-287.

(60) Wolfenstine, J.; Campos, S.; Foster, D.; Read, J.; Behl, W. K. *J. Power Sources* **2002**, *109*, 230-233.
(61) Raimondi, F.; Scherer, G. G.; Kotz, R.; Wokaun, A. *Angew. Chem.-Int. Edit.* **2005**, *44*, 2190-2209.
(62) Hassoun, J.; Panero, S.; Simon, P.; Taberna, P. L.; Scrosati, B. *Adv. Mater.* **2007**, *19*, 1632-+.
(63) Gao, B.; Sinha, S.; Fleming, L.; Zhou, O. *Adv. Mater.* **2001**, *13*, 816-+.
(64) Armstrong, A. R.; Armstrong, G.; Canales, J.; Bruce, P. G. *Angew. Chem.-Int. Edit.* **2004**, *43*, 2286-2288.
(65) Armstrong, G.; Armstrong, A. R.; Bruce, P. G.; Reale, P.; Scrosati, B. *Adv. Mater.* **2006**, *18*, 2597-+.
(66) Armstrong, G.; Armstrong, A. R.; Canales, J.; Bruce, P. G. *Chem. Commun.* **2005**, 2454-2456.
(67) Nam, K. T.; Kim, D. W.; Yoo, P. J.; Chiang, C. Y.; Meethong, N.; Hammond, P. T.; Chiang, Y. M.; Belcher, A. M. *Science* **2006**, *312*, 885-888.
(68) Cho, J. *Electrochem. Commun.* **2003**, *5*, 146-148.
(69) Son, D.; Kim, E.; Kim, T. G.; Kim, M. G.; Cho, J. H.; Park, B. *Appl. Phys. Lett.* **2004**, *85*, 5875-5877.
(70) Zhang, S. C.; Qiu, X. P.; He, Z. Q.; Weng, D. S.; Zhu, W. T. 2006, p 350-353.
(71) Herle, P. S.; Ellis, B.; Coombs, N.; Nazar, L. F. *Nat. Mater.* **2004**, *3*, 147-152.
(72) Prosini, P. P.; Carewska, M.; Scaccia, S.; Wisniewski, P.; Passerini, S.; Pasquali, M. *J. Electrochem. Soc.* **2002**, *149*, A886-A890.
(73) Yamada, A.; Hosoya, M.; Chung, S. C.; Kudo, Y.; Hinokuma, K.; Liu, K. Y.; Nishi, Y. 2003, p 232-238.
(74) Zhou, Y. K.; Shen, C. M.; Li, H. L. *Solid State Ionics* **2002**, *146*, 81-86.
(75) Li, W. Y.; Xu, L. N.; Chen, J. *Adv. Funct. Mater.* **2005**, *15*, 851-857.
(76) Sides, C. R.; Croce, F.; Young, V. Y.; Martin, C. R.; Scrosati, B. *Electrochemical and Solid State Letters* **2005**, *8*, A484-A487.
(77) Patrissi, C. J.; Martin, C. R. *J. Electrochem. Soc.* **1999**, *146*, 3176-3180.
(78) Kang, K. S.; Meng, Y. S.; Breger, J.; Grey, C. P.; Ceder, G. *Science* **2006**, *311*, 977-980.
(79) Patil, A.; Patil, V.; Shin, D. W.; Choi, J. W.; Paik, D. S.; Yoon, S. J. *Mater. Res. Bull.* **2008**, *43*, 1913-1942.
(80) Novak, P.; Muller, K.; Santhanam, K. S. V.; Haas, O. *Chem. Rev.* **1997**, *97*, 207-281.
(81) Reddy, A. L. M.; Shaijumon, M. M.; Gowda, S. R.; Ajayan, P. M. *Nano Lett.* **2009**, *9*, 1002-1006.
(82) Kwon, Y.; Kim, H.; Doo, S. G.; Cho, J. H. *Chem. Mater.* **2007**, *19*, 982-986.
(83) Xie, H. M.; Wang, R. S.; Ying, J. R.; Zhang, L. Y.; Jalbout, A. F.; Yu, H. Y.; Yang, G. L.; Pan, X. M.; Su, Z. M. *Adv. Mater.* **2006**, *18*, 2609-+.
(84) Kim, D. W.; Hwang, I. S.; Kwon, S. J.; Kang, H. Y.; Park, K. S.; Choi, Y. J.; Choi, K. J.; Park, J. G. *Nano Lett.* **2007**, *7*, 3041-3045.
(85) Niederberger, M. *Acc. Chem. Res.* **2007**, *40*, 793-800.
(86) Trewyn, B. G.; Slowing, II; Giri, S.; Chen, H. T.; Lin, V. S. Y. *Acc. Chem. Res.* **2007**, *40*, 846-853.

(87) Cassell, A. M.; Raymakers, J. A.; Kong, J.; Dai, H. J. *J. Phys. Chem. B* **1999**, *103*, 6484-6492.
(88) Wu, Y. Y.; Fan, R.; Yang, P. D. *Nano Lett.* **2002**, *2*, 83-86.
(89) Barbe, C. J.; Arendse, F.; Comte, P.; Jirousek, M.; Lenzmann, F.; Shklover, V.; Gratzel, M. *J. Am. Ceram. Soc.* **1997**, *80*, 3157-3171.
(90) Wang, X.; Li, Y. D. *J. Am. Chem. Soc.* **2002**, *124*, 2880-2881.
(91) Blanco, A.; Chomski, E.; Grabtchak, S.; Ibisate, M.; John, S.; Leonard, S. W.; Lopez, C.; Meseguer, F.; Miguez, H.; Mondia, J. P.; Ozin, G. A.; Toader, O.; van Driel, H. M. *Nature* **2000**, *405*, 437-440.
(92) Martin, C. R. *Science* **1994**, *266*, 1961-1966.
(93) Kresge, C. T.; Leonowicz, M. E.; Roth, W. J.; Vartuli, J. C.; Beck, J. S. *Nature* **1992**, *359*, 710-712.
(94) Ying, J. Y.; Mehnert, C. P.; Wong, M. S. *Angewandte Chemie-International Edition* **1999**, *38*, 56-77.
(95) Han, W. Q.; Fan, S. S.; Li, Q. Q.; Hu, Y. D. *Science* **1997**, *277*, 1287-1289.
(96) Cheng, F.; Tao, Z.; Liang, J.; Chen, J. *Chem. Mater.* **2008**, *20*, 667-681.
(97) Che, G. L.; Lakshmi, B. B.; Fisher, E. R.; Martin, C. R. *Nature* **1998**, *393*, 346-349.
(98) Che, G.; Lakshmi, B. B.; Martin, C. R.; Fisher, E. R.; Ruoff, R. S. *Chem. Mater.* **1998**, *10*, 260-267.
(99) Phillips, J.; Shiina, T.; Nemer, M.; Lester, K. *Langmuir* **2006**, *22*, 9694-9703.
(100) Li, N. C.; Martin, C. R. *J. Electrochem. Soc.* **2001**, *148*, A164-A170.
(101) Li, N. C.; Martin, C. R.; Scrosati, B. *Electrochemical and Solid State Letters* **2000**, *3*, 316-318.
(102) Patrissi, C. J.; Martin, C. R. *J. Electrochem. Soc.* **2001**, *148*, A1247-A1253.
(103) Li, N. C.; Martin, C. R.; Scrosati, B. *J. Power Sources* **2001**, *97-8*, 240-243.
(104) Sides, C. R.; Li, N. C.; Patrissi, C. J.; Scrosati, B.; Martin, C. R. *Mrs Bulletin* **2002**, *27*, 604-607.
(105) Sides, C. R.; Martin, C. R. *Adv. Mater.* **2005**, *17*, 125-128.
(106) Long, J. W.; Rhodes, C. P.; Young, A. L.; Rolison, D. R. *Nano Lett.* **2003**, *3*, 1155-1161.
(107) Li, N. C.; Patrissi, C. J.; Che, G. L.; Martin, C. R. *J. Electrochem. Soc.* **2000**, *147*, 2044-2049.
(108) Nishizawa, M.; Mukai, K.; Kuwabata, S.; Martin, C. R.; Yoneyama, H. *J. Electrochem. Soc.* **1997**, *144*, 1923-1927.
(109) Liu, R.; Lee, S. B. *J. Am. Chem. Soc.* **2008**, *130*, 2942-2943.
(110) Taberna, L.; Mitra, S.; Poizot, P.; Simon, P.; Tarascon, J. M. *Nat. Mater.* **2006**, *5*, 567-573.
(111) Hassoun, J.; Panero, S.; Simon, P.; Taberna, P. L.; Scrosati, B. *Adv. Mater.* **2007**, *19*, 1632-+.
(112) Yang, P. D.; Zhao, D. Y.; Margolese, D. I.; Chmelka, B. F.; Stucky, G. D. *Nature* **1998**, *396*, 152-155.
(113) Asefa, T.; MacLachlan, M. J.; Coombs, N.; Ozin, G. A. *Nature* **1999**, *402*, 867-871.
(114) Ren, Z. F.; Huang, Z. P.; Xu, J. W.; Wang, J. H.; Bush, P.; Siegal, M. P.; Provencio, P. N. *Science* **1998**, *282*, 1105-1107.

(115) Lu, A. H.; Schuth, F. *Adv. Mater.* **2006**, *18*, 1793-1805.
(116) Yang, H. F.; Shi, Q. H.; Tian, B. Z.; Lu, Q. Y.; Gao, F.; Xie, S. H.; Fan, J.; Yu, C. Z.; Tu, B.; Zhao, D. Y. *J. Am. Chem. Soc.* **2003**, *125*, 4724-4725.
(117) Yang, H. F.; Zhao, D. Y. *J. Mater. Chem.* **2005**, *15*, 1217-1231.
(118) Norris, D. J.; Vlasov, Y. A. *Adv. Mater.* **2001**, *13*, 371-376.
(119) Wijnhoven, J.; Vos, W. L. *Science* **1998**, *281*, 802-804.
(120) Yoshino, K.; Shimoda, Y.; Kawagishi, Y.; Nakayama, K.; Ozaki, M. *Appl. Phys. Lett.* **1999**, *75*, 932-934.
(121) Possin, G. E. *Rev. Sci. Instrum.* **1970**, *41*, 772-&.
(122) Hulteen, J. C.; Martin, C. R. *J. Mater. Chem.* **1997**, *7*, 1075-1087.
(123) Martin, C. R. *Chem. Mater.* **1996**, *8*, 1739-1746.
(124) Lakshmi, B. B.; Dorhout, P. K.; Martin, C. R. *Chem. Mater.* **1997**, *9*, 857-862.
(125) Martin, C. R. *Acc. Chem. Res.* **1995**, *28*, 61-68.
(126) Klein, J. D.; Herrick, R. D.; Palmer, D.; Sailor, M. J.; Brumlik, C. J.; Martin, C. R. *Chem. Mater.* **1993**, *5*, 902-904.
(127) Bao, J. C.; Tie, C. Y.; Xu, Z.; Zhou, Q. F.; Shen, D.; Ma, Q. *Adv. Mater.* **2001**, *13*, 1631-+.
(128) Mbindyo, J. K. N.; Mallouk, T. E.; Mattzela, J. B.; Kratochvilova, I.; Razavi, B.; Jackson, T. N.; Mayer, T. S. *J. Am. Chem. Soc.* **2002**, *124*, 4020-4026.
(129) Li, L.; Yang, Y. W.; Li, G. H.; Zhang, L. D. *Small* **2006**, *2*, 548-553.
(130) Wang, S.; Yu, G. J.; Gong, J. L.; Li, Q. T.; Xu, H. J.; Zhu, D. Z.; Zhu, Z. Y. *Nanotechnology* **2006**, *17*, 1594-1598.
(131) Yuan, Z. H.; Zhou, W.; Duan, Y. Q.; Bie, L. J. *Nanotechnology* **2008**, *19*.
(132) Lei, Y.; Chim, W. K. *Chem. Mater.* **2005**, *17*, 580-585.
(133) Zach, M. P.; Inazu, K.; Ng, K. H.; Hemminger, J. C.; Penner, R. M. *Chem. Mater.* **2002**, *14*, 3206-3216.
(134) Walter, E. C.; Murray, B. J.; Favier, F.; Kaltenpoth, G.; Grunze, M.; Penner, R. M. *J. Phys. Chem. B* **2002**, *106*, 11407-11411.
(135) Menke, E. J.; Li, Q.; Penner, R. M. *Nano Lett.* **2004**, *4*, 2009-2014.
(136) Sun, Y. G.; Mayers, B. T.; Xia, Y. N. *Nano Lett.* **2002**, *2*, 481-485.
(137) Lou, X. W.; Archer, L. A.; Yang, Z. C. *Adv. Mater.* **2008**, *20*, 3987-4019.
(138) Huo, Q. S.; Margolese, D. I.; Ciesla, U.; Feng, P. Y.; Gier, T. E.; Sieger, P.; Leon, R.; Petroff, P. M.; Schuth, F.; Stucky, G. D. *Nature* **1994**, *368*, 317-321.
(139) Peng, X. G.; Manna, L.; Yang, W. D.; Wickham, J.; Scher, E.; Kadavanich, A.; Alivisatos, A. P. *Nature* **2000**, *404*, 59-61.
(140) Bagshaw, S. A.; Prouzet, E.; Pinnavaia, T. J. *Science* **1995**, *269*, 1242-1244.
(141) Thurn-Albrecht, T.; Schotter, J.; Kastle, C. A.; Emley, N.; Shibauchi, T.; Krusin-Elbaum, L.; Guarini, K.; Black, C. T.; Tuominen, M. T.; Russell, T. P. *Science* **2000**, *290*, 2126-2129.
(142) Lazzari, M.; Lopez-Quintela, M. A. *Adv. Mater.* **2003**, *15*, 1583-1594.
(143) Stein, A.; Melde, B. J.; Schroden, R. C. *Adv. Mater.* **2000**, *12*, 1403-1419.
(144) Fendler, J. H. *Chem. Mater.* **1996**, *8*, 1616-1624.
(145) Raman, N. K.; Anderson, M. T.; Brinker, C. J. *Chem. Mater.* **1996**, *8*, 1682-1701.
(146) Nikoobakht, B.; El-Sayed, M. A. *Chem. Mater.* **2003**, *15*, 1957-1962.

(147) Sotiropoulou, S.; Sierra-Sastre, Y.; Mark, S. S.; Batt, C. A. *Chem. Mater.* **2008**, *20*, 821-834.
(148) Reches, M.; Gazit, E. *Science* **2003**, *300*, 625-627.
(149) Mirkin, C. A.; Letsinger, R. L.; Mucic, R. C.; Storhoff, J. J. *Nature* **1996**, *382*, 607-609.
(150) Therese, G. H. A.; Kamath, P. V. *Chem. Mater.* **2000**, *12*, 1195-1204.
(151) Xu, X. C.; Chen, L. D.; Wang, C. F.; Yao, Q.; Feng, C. D. *J. Solid State Chem.* **2005**, *178*, 2163-2166.
(152) Xiao, R.; Il Cho, S.; Liu, R.; Lee, S. B. *J. Am. Chem. Soc.* **2007**, *129*, 4483-4489.
(153) Cho, S. I.; Kwon, W. J.; Choi, S. J.; Kim, P.; Park, S. A.; Kim, J.; Son, S. J.; Xiao, R.; Kim, S. H.; Lee, S. B. *Adv. Mater.* **2005**, *17*, 171-+.
(154) Il Cho, S.; Lee, S. B. *Acc. Chem. Res.* **2008**, *41*, 699-707.
(155) Caruso, R. A.; Antonietti, M. *Chem. Mater.* **2001**, *13*, 3272-3282.
(156) Gasparac, R.; Kohli, P.; Mota, M. O.; Trofin, L.; Martin, C. R. *Nano Lett.* **2004**, *4*, 513-516.
(157) Daub, M.; Knez, M.; Goesele, U.; Nielsch, K. 2007.
(158) Perez, I.; Robertson, E.; Banerjee, P.; Henn-Lecordier, L.; Son, S. J.; Lee, S. B.; Rubloff, G. W. *Small* **2008**, *4*, 1223-1232.
(159) Hou, S. F.; Wang, J. H.; Martin, C. R. *J. Am. Chem. Soc.* **2005**, *127*, 8586-8587.
(160) Steinhart, M.; Wendorff, J. H.; Greiner, A.; Wehrspohn, R. B.; Nielsch, K.; Schilling, J.; Choi, J.; Gosele, U. *Science* **2002**, *296*, 1997-1997.
(161) Hurst, S. J.; Payne, E. K.; Qin, L. D.; Mirkin, C. A. *Angew. Chem.-Int. Edit.* **2006**, *45*, 2672-2692.
(162) He, B.; Son, S. J.; Lee, S. B. *Langmuir* **2006**, *22*, 8263-8265.
(163) Hernandez, R. M.; Richter, L.; Semancik, S.; Stranick, S.; Mallouk, T. E. *Chem. Mater.* **2004**, *16*, 3431-3438.
(164) Mieszawska, A. J.; Jalilian, R.; Sumanasekera, G. U.; Zamborini, F. P. *Small* **2007**, *3*, 722-756.
(165) Reynes, O.; Demoustier-Champagne, S. *J. Electrochem. Soc.* **2005**, *152*, D130-D135.
(166) Ji, C. X.; Searson, P. C. *J. Phys. Chem. B* **2003**, *107*, 4494-4499.
(167) Pena, D. J.; Mbindyo, J. K. N.; Carado, A. J.; Mallouk, T. E.; Keating, C. D.; Razavi, B.; Mayer, T. S. *J. Phys. Chem. B* **2002**, *106*, 7458-7462.
(168) Kovtyukhova, N. I.; Martin, B. R.; Mbindyo, J. K. N.; Mallouk, T. E.; Cabassi, M.; Mayer, T. S. 2002, p 255-262.
(169) Kovtyukhova, N. I.; Martin, B. R.; Mbindyo, J. K. N.; Smith, P. A.; Razavi, B.; Mayer, T. S.; Mallouk, T. E. *J. Phys. Chem. B* **2001**, *105*, 8762-8769.
(170) Kovtyukhova, N. I.; Mallouk, T. E.; Mayer, T. S. *Adv. Mater.* **2003**, *15*, 780-+.
(171) Martin, C. R.; Mitchell, D. T. In *Electroanalytical Chemistry, Vol 21* 1999; Vol. 21, p 1-74.
(172) Martin, C. R.; Nishizawa, M.; Jirage, K.; Kang, M. *J. Phys. Chem. B* **2001**, *105*, 1925-1934.
(173) Wirtz, M.; Martin, C. R. *Adv. Mater.* **2003**, *15*, 455-458.
(174) Kros, A.; Nolte, R. J. M.; Sommerdijk, N. *Adv. Mater.* **2002**, *14*, 1779-1782.
(175) Yuan, J. H.; Wang, K.; Xia, X. H. *Adv. Funct. Mater.* **2005**, *15*, 803-809.

(176) He, Q.; Tian, Y.; Cui, Y.; Mohwald, H.; Li, J. B. *J. Mater. Chem.* **2008**, *18*, 748-754.
(177) Ikezawa, Y.; Nishimura, K.; Uchida, H.; Inoue, M.; Elsevier Science Bv: 2004, p 1690-1691.
(178) Schonenberger, C.; vanderZande, B. M. I.; Fokkink, L. G. J.; Henny, M.; Schmid, C.; Kruger, M.; Bachtold, A.; Huber, R.; Birk, H.; Staufer, U. *J. Phys. Chem. B* **1997**, *101*, 5497-5505.
(179) Hillebrenner, H.; Buyukserin, F.; Stewart, J. D.; Martin, C. R. *Nanomedicine* **2006**, *1*, 39-50.
(180) Li, S. F. Y.; Mark, S. S.; Kricka, L. J. *Current Nanoscience* **2009**, *5*, 182-188.
(181) Kang, S.; Su, P. C.; Park, Y. I.; Saito, Y.; Prinz, F. B. *J. Electrochem. Soc.* **2006**, *153*, A554-A559.
(182) Wang, H.; Xu, C. W.; Cheng, F. L.; Jiang, S. P. *Electrochem. Commun.* **2007**, *9*, 1212-1216.
(183) Foll, H.; Christophersen, M.; Carstensen, J.; Hasse, G. *Mater. Sci. Eng. R-Rep.* **2002**, *39*, 93-141.
(184) Macak, J. M.; Tsuchiya, H.; Schmuki, P. *Angew. Chem.-Int. Edit.* **2005**, *44*, 2100-2102.
(185) Gong, D.; Grimes, C. A.; Varghese, O. K.; Hu, W. C.; Singh, R. S.; Chen, Z.; Dickey, E. C. *J. Mater. Res.* **2001**, *16*, 3331-3334.
(186) Osulliva.Jp; Wood, G. C. *Proceedings of the Royal Society of London Series a-Mathematical and Physical Sciences* **1970**, *317*, 511-&.
(187) Nielsch, K.; Choi, J.; Schwirn, K.; Wehrspohn, R. B.; Gosele, U. *Nano Lett.* **2002**, *2*, 677-680.
(188) F. Keller, M. S. H., D. L. Robinson *J. Electrochem. Soc.*, *100*, 411-419.
(189) Wernick, S., Pinner, R. and Sheasby, P.G. *The Surface Treatment and Finishing of Aluminium and its Alloys*, 1987.
(190) Sulka, G. D.; Parkola, K. G. *Thin Solid Films* **2006**, *515*, 338-345.
(191) Thompson, G. E. a. W., G.C. *Treatise on Materials Science and Technology*; Academic Press New York, 1983.
(192) Despić, A. a. P., V.P. *Modern Aspects of Electrochemistry*; Plenum Press, New York and London.
(193) Ono, S.; Ichinose, H.; Masuko, N. *J. Electrochem. Soc.* **1991**, *138*, 3705-3710.
(194) Delloca, C. J.; Fleming, P. J. *J. Electrochem. Soc.* **1976**, *123*, 1487-1493.
(195) Zhao, X. W.; Jiang, P.; Xie, S. S.; Feng, J. F.; Gao, Y.; Wang, J. X.; Liu, D. F.; Song, L.; Liu, L. F.; Dou, X. Y.; Luo, S. D.; Zhang, Z. X.; Xiang, Y. J.; Zhou, W. Y.; Wang, G. *Nanotechnology* **2006**, *17*, 35-39.
(196) Lee, W.; Ji, R.; Gosele, U.; Nielsch, K. *Nat. Mater.* **2006**, *5*, 741-747.
(197) Schneider, J. J.; Engstler, N.; Budna, K. P.; Teichert, C.; Franzka, S. *Eur. J. Inorg. Chem.* **2005**, 2352-2359.
(198) Yuan, J. H.; Chen, W.; Hui, R. J.; Hu, Y. L.; Xia, X. H. *Electrochim. Acta* **2006**, *51*, 4589-4595.
(199) Xu, W. L.; Chen, H.; Zheng, M. J.; Ding, G. Q.; Shen, W. Z. *Opt. Mater.* **2006**, *28*, 1160-1165.
(200) Xu, T.; Zangari, G.; Metzger, R. M. *Nano Lett.* **2002**, *2*, 37-41.

(201) Yu, J. S.; Kim, J. Y.; Lee, S.; Mbindyo, J. K. N.; Martin, B. R.; Mallouk, T. E. *Chem. Commun.* **2000**, 2445-2446.
(202) Kline, T. R.; Tian, M. L.; Wang, J. G.; Sen, A.; Chan, M. W. H.; Mallouk, T. E. *Inorg. Chem.* **2006**, *45*, 7555-7565.
(203) Piao, Y.; Lim, H.; Chang, J. Y.; Lee, W. Y.; Kim, H.; Pergamon-Elsevier Science Ltd: 2005, p 2997-3013.
(204) Wu, Y. Y.; Livneh, T.; Zhang, Y. X.; Cheng, G. S.; Wang, J. F.; Tang, J.; Moskovits, M.; Stucky, G. D. *Nano Lett.* **2004**, *4*, 2337-2342.
(205) Gao, T.; Meng, G. W.; Wang, Y. W.; Sun, S. H.; Zhang, L. *J. Phys.-Condes. Matter* **2002**, *14*, 355-363.
(206) Nishio, K.; Iwata, K.; Masuda, H. *Electrochemical and Solid State Letters* **2003**, *6*, H21-H23.
(207) Cepak, V. M.; Martin, C. R. *Chem. Mater.* **1999**, *11*, 1363-1367.
(208) Kuwabata, S.; Martin, C. R. *J. Membr. Sci.* **1994**, *91*, 1-12.
(209) Winter, M.; Brodd, R. J. *Chem. Rev.* **2004**, *104*, 4245-4269.
(210) Burke, A. *J. Power Sources* **2000**, *91*, 37-50.
(211) Vol'fkovich, Y. M.; Serdyuk, T. M. *Russian Journal of Electrochemistry* **2002**, *38*, 935-958.
(212) Conway, B. E.; Birss, V.; Wojtowicz, J. *J. Power Sources* **1997**, *66*, 1-14.
(213) Rudge, A.; Davey, J.; Raistrick, I.; Gottesfeld, S.; Ferraris, J. P. *J. Power Sources* **1994**, *47*, 89-107.
(214) Song, H. K.; Palmore, G. T. R. *Advanced Materials* **2006**, *18*, 1764-+.
(215) Hu, C. C.; Wang, C. C. *J. Electrochem. Soc.* **2003**, *150*, A1079-A1084.
(216) Malinauskas, A.; Malinauskiene, J.; Ramanavicius, A. *Nanotechnology* **2005**, *16*, R51-R62.
(217) Arbizzani, C.; Mastragostino, M.; Soavi, F. *J. Power Sources* **2001**, *100*, 164-170.
(218) Carlberg, J. C.; Inganas, O. *J. Electrochem. Soc.* **1997**, *144*, L61-L64.
(219) Ryu, K. S.; Lee, Y. G.; Hong, Y. S.; Park, Y. J.; Wu, X. L.; Kim, K. M.; Kang, M. G.; Park, N. G.; Chang, S. H. *Electrochim. Acta* **2004**, *50*, 843-847.
(220) Lota, K.; Khomenko, V.; Frackowiak, E. *J. Phys. Chem. Solids* **2004**, *65*, 295-301.
(221) Li, W. K.; Chen, J.; Zhao, J. J.; Zhang, J. R.; Zhu, J. J. *Mater. Lett.* **2005**, *59*, 800-803.
(222) Heywang, G.; Jonas, F. *Advanced Materials* **1992**, *4*, 116-118.
(223) Jang, J.; Bae, J.; Park, E. *Advanced Materials* **2006**, *18*, 354-+.
(224) Ingram, M. D.; Staesche, H.; Ryder, K. S. *J. Power Sources* **2004**, *129*, 107-112.
(225) Arico, A. S.; Bruce, P.; Scrosati, B.; Tarascon, J.-M.; van Schalkwijk, W. *Nat. Mater.* **2005**, *4*, 366-377.
(226) Cho, S. I.; Choi, D. H.; Kim, S.-H.; Lee, S. B. *Chem. Mater.* **2005**, *17*, 4564-4566.
(227) Cho, S. I.; Kwon, W. J.; Choi, S. J.; Kim, P.; Park, S. A.; Kim, J.; Son, S. J.; Xiao, R.; Kim, S. H.; Lee, S. B. *Advanced Materials* **2005**, *17*, 171-+.
(228) Xiao, R.; Cho, S. I.; Liu, R.; Lee, S. B. *submitted to J. Am. Chem. Soc.* .
(229) Vandyke, L. S.; Martin, C. R. *Langmuir* **1990**, *6*, 1118-1123.

(230) Cai, Z. H.; Martin, C. R. *Synth. Met.* **1992**, *46*, 165-179.
(231) Sides, C. R.; Martin, C. R. *Advanced Materials* **2005**, *17*, 125-+.
(232) Che, G.; Jirage, K. B.; Fisher, E. R.; Martin, C. R.; Yoneyama, H. *J. Electrochem. Soc.* **1997**, *144*, 4296-4302.
(233) Niu, L.; Kvarnstrom, C.; Froberg, K.; Ivaska, A. *Synth. Met.* **2001**, *122*, 425-429.
(234) Groenendaal, L. B.; Zotti, G.; Aubert, P.-H.; Waybright, S. M.; Reynolds, J. R. *Adv. Mater. (Weinheim, Ger.)* **2003**, *15*, 855-879.
(235) Randriamahazaka, H.; Noel, V.; Chevrot, C. *J. Electroanal. Chem.* **1999**, *472*, 103-111.
(236) Ahonen, H. J.; Lukkari, J.; Kankare, J. *Macromolecules* **2000**, *33*, 6787-6793.
(237) An, K. H.; Kim, W. S.; Park, Y. S.; Choi, Y. C.; Lee, S. M.; Chung, D. C.; Bae, D. J.; Lim, S. C.; Lee, Y. H. *Advanced Materials* **2001**, *13*, 497-+.
(238) Du, C. S.; Yeh, J.; Pan, N. *Nanotechnology* **2005**, *16*, 350-353.
(239) Niu, C. M.; Sichel, E. K.; Hoch, R.; Moy, D.; Tennent, H. *Appl. Phys. Lett.* **1997**, *70*, 1480-1482.
(240) Zheng, J. P. *J. Electrochem. Soc.* **2005**, *152*, A1864-A1869.
(241) Belanger, D.; Ren, X. M.; Davey, J.; Uribe, F.; Gottesfeld, S. *J. Electrochem. Soc.* **2000**, *147*, 2923-2929.
(242) Ferraris, J. P.; Eissa, M. M.; Brotherston, I. D.; Loveday, D. C. *Chem. Mater.* **1998**, *10*, 3528-3535.
(243) Fusalba, F.; Ho, H. A.; Breau, L.; Belanger, D. *Chem. Mater.* **2000**, *12*, 2581-2589.
(244) Gupta, V.; Miura, N. *Electrochemical and Solid State Letters* **2005**, *8*, A630-A632.
(245) Kim, J. Y.; Chung, I. J. *J. Electrochem. Soc.* **2002**, *149*, A1376-A1380.
(246) Laforgue, A.; Simon, P.; Fauvarque, J. F.; Mastragostino, M.; Soavi, F.; Sarrau, J. F.; Lailler, P.; Conte, M.; Rossi, E.; Saguatti, S. *J. Electrochem. Soc.* **2003**, *150*, A645-A651.
(247) Laforgue, A.; Simon, P.; Fauvarque, J. F.; Sarrau, J. F.; Lailler, P. *J. Electrochem. Soc.* **2001**, *148*, A1130-A1134.
(248) Mastragostino, M.; Arbizzani, C.; Paraventi, R.; Zanelli, A. *J. Electrochem. Soc.* **2000**, *147*, 407-412.
(249) Prasad, K. R.; Munichandraiah, N. *Electrochemical and Solid State Letters* **2002**, *5*, A271-A274.
(250) Prasad, K. R.; Munichandraiah, N. *J. Electrochem. Soc.* **2002**, *149*, A1393-A1399.
(251) Soudan, P.; Ho, H. A.; Breau, L.; Belanger, D. *J. Electrochem. Soc.* **2001**, *148*, A775-A782.
(252) Villers, D.; Jobin, D.; Soucy, C.; Cossement, D.; Chahine, R.; Breau, L.; Belanger, D. *J. Electrochem. Soc.* **2003**, *150*, A747-A752.
(253) R, B. E. a. M. J. *Impedance Spectroscopy: Theory, Experiment, and Applications*; New Jersey: Wiley, 2005.
(254) Noel, V.; Randriamahazaka, H.; Chevrot, C. *J. Electroanal. Chem.* **2003**, *558*, 41-48.
(255) Jang, J.; Bae, J.; Park, E. *Adv. Mater.* **2006**, *18*, 354-358.

(256) Zang, J. F.; Bao, S. J.; Li, C. M.; Bian, H. J.; Cui, X. Q.; Bao, Q. L.; Sun, C. Q.; Guo, J.; Lian, K. R. *J. Phys. Chem. C* **2008**, *112*, 14843-14847.
(257) Hong, J. I.; Yeo, I. H.; Paik, W. K. *J. Electrochem. Soc.* **2001**, *148*, A156-A163.
(258) Hu, C. C.; Huang, Y. H. *J. Electrochem. Soc.* **1999**, *146*, 2465-2471.
(259) Xiao, R.; Cho, S. I.; Liu, R.; Lee, S. B. *J. Am. Chem. Soc.* **2007**, *129*, 4483-4489.
(260) Niu, L.; Kvarnstrom, C.; Fröberg, K.; Ivaska, A. *Synth. Met.* **2001**, *122*, 425-429.
(261) Huang, L. M.; Lin, H. Z.; Wen, T. C.; Gopalan, A. *Electrochim. Acta* **2006**, *52*, 1058-1063.
(262) Liu, R.; Cho, S. I.; Lee, S. B. *Nanotechnology* **2008**, *19*, 215710.
(263) Li, Q. G.; Olson, J. B.; Penner, R. M. *Chem. Mater.* **2004**, *16*, 3402-3405.
(264) Law, M.; Greene, L. E.; Johnson, J. C.; Saykally, R.; Yang, P. D. *Nat. Mater.* **2005**, *4*, 455-459.
(265) Goodey, A. P.; Eichfeld, S. M.; Lew, K. K.; Redwing, J. M.; Mallouk, T. E. *J. Am. Chem. Soc.* **2007**, *129*, 12344-+.
(266) Kovtyukhova, N. L.; Mallouk, T. E. *Adv. Mater.* **2005**, *17*, 187-+.
(267) Tian, B. Z.; Zheng, X. L.; Kempa, T. J.; Fang, Y.; Yu, N. F.; Yu, G. H.; Huang, J. L.; Lieber, C. M. *Nature* **2007**, *449*, 885-U8.
(268) Fan, H. J.; Knez, M.; Scholz, R.; Nielsch, K.; Pippel, E.; Hesse, D.; Zacharias, M.; Gosele, U. *Nat. Mater.* **2006**, *5*, 627-631.
(269) Liu, Z. Q.; Zhang, D. H.; Han, S.; Li, C.; Lei, B.; Lu, W. G.; Fang, J. Y.; Zhou, C. W. *J. Am. Chem. Soc.* **2005**, *127*, 6-7.
(270) Desilvestro, J.; Haas, O. *J. Electrochem. Soc.* **1990**, *137*, C5-C22.
(271) Zhu, C. L.; Chou, S. W.; He, S. F.; Liao, W. N.; Chen, C. C. *Nanotechnology* **2007**, *18*, 6.
(272) Peng, X. S.; Jin, J.; Ichinose, I. *Adv. Funct. Mater.* **2007**, *17*, 1849-1855.
(273) Chang, J. K.; Tsai, W. T. *J. Appl. Electrochem.* **2004**, *34*, 953-961.
(274) Groenendaal, L.; Zotti, G.; Aubert, P. H.; Waybright, S. M.; Reynolds, J. R. *Adv. Mater.* **2003**, *15*, 855-879.
(275) Liu, R.; Oba, F.; Bohannan, E. W.; Ernst, F.; Switzer, J. A. *Chem. Mater.* **2003**, *15*, 4882-4885.
(276) Siegfried, M. J.; Choi, K. S. *J. Am. Chem. Soc.* **2006**, *128*, 10356-10357.
(277) Li, C.; Imae, T. *Macromolecules* **2004**, *37*, 2411-2416.
(278) Cahen, S.; Janot, R.; Laffont-Dantras, L.; Tarascon, J. M. *J. Electrochem. Soc.* **2008**, *155*, A512-A519.
(279) Chang, J. K.; Tsai, W. T. *J. Electrochem. Soc.* **2003**, *150*, A1333-A1338.
(280) Wu, M. S.; Chiang, P. C. J. *Electrochemical and Solid State Letters* **2004**, *7*, A123-A126.
(281) Piraux, L.; George, J. M.; Despres, J. F.; Leroy, C.; Ferain, E.; Legras, R.; Ounadjela, K.; Fert, A. *Appl. Phys. Lett.* **1994**, *65*, 2484-2486.
(282) Liang, H. P.; Guo, Y. G.; Hu, J. S.; Zhu, C. F.; Wan, L. J.; Bai, C. L. *Inorg. Chem.* **2005**, *44*, 3013-3015.
(283) Chen, X.; Knez, M.; Berger, A.; Nielsch, K.; Gosele, U.; Steinhart, M. *Angew Chem Int Edit* **2007**, *46*, 6829-6832.

(284) Kim, J. S.; Rieter, W. J.; Taylor, K. M. L.; An, H.; Lin, W. L.; Lin, W. B. *J. Am. Chem. Soc.* **2007**, *129*, 8962-8963.
(285) Meduri, P.; Pendyala, C.; Kumar, V.; Sumanasekera, G. U.; Sunkara, M. K. *Nano Lett.* **2009**, *9*, 612-616.
(286) Lauhon, L. J.; Gudiksen, M. S.; Wang, C. L.; Lieber, C. M. *Nature* **2002**, *420*, 57-61.
(287) Srivastava, S.; Kotov, N. A. *Acc. Chem. Res.* **2008**, *41*, 1831-1841.
(288) Guo, Y. G.; Hu, J. S.; Liang, H. P.; Wan, L. J.; Bai, C. L. *Chem. Mater.* **2003**, *15*, 4332-4336.
(289) Son, S. J.; Reichel, J.; He, B.; Schuchman, M.; Lee, S. B. *J. Am. Chem. Soc.* **2005**, *127*, 7316-7317.
(290) Randriamahazaka, H.; Noel, V.; Chevrot, C. *J. Electroanal. Chem.* **1999**, *476*, 183-183.
(291) Ragupathy, P.; Vasan, H. N.; Munichandraiah, N. *J. Electrochem. Soc.* **2008**, *155*, A34-A40.
(292) Fawcett, W. R.; Kloss, A. A. *J. Phys. Chem.* **1996**, *100*, 2019-2024.
(293) Gardella, J. A.; Ferguson, S. A.; Chin, R. L. *Appl. Spectrosc.* **1986**, *40*, 224-232.
(294) Yoshioka, Y.; Calvert, P. D.; Jabbour, G. E. *Macromol. Rapid Commun.* **2005**, *26*, 238-246.
(295) Yoshioka, Y.; Jabbour, G. E. *Adv. Mater.* **2006**, *18*, 1307-1312.
(296) Shinomiya, T.; Gupta, V.; Miura, N. *Electrochim. Acta* **2005**, *51*, 4412-4419.
(297) Wang, X. Y.; Wang, X. Y.; Huang, W. G.; Sebastian, P. J.; Gamboa, S. *J. Power Sources* **2005**, *140*, 211-215.
(298) Chen, J.; Liu, Y.; Minett, A. I.; Lynam, C.; Wang, J. Z.; Wallace, G. G. *Chem. Mater.* **2007**, *19*, 3595-3597.
(299) Liu, D. W.; Zhang, Q. F.; Xiao, P.; Garcia, B. B.; Guo, Q.; Champion, R.; Cao, G. Z. *Chem. Mater.* **2008**, *20*, 1376-1380.
(300) Aasmundtveit, K. E.; Samuelsen, E. J.; Pettersson, L. A. A.; Inganäs, O.; Johansson, T.; Feidenhans, R. *Synth. Met.* **1999**, *101*, 561-564.